DYNAMICS OF DIAMAGNETICALLY LEVITATING RESONATORS

DYNAMICS OF DIAMAGNETICALLY LEVITATING RESONATORS

Dissertation

for the purpose of obtaining the degree of doctor
at Delft University of Technology,
by the authority of the Rector Magnificus, prof. dr. ir. T. H. J. J. van der Hagen,
chair of the Board for Doctorates,
to be defended publicly on
Wednesday 1 March 2023 at 10:00 o'clock.

by

Xianfeng CHEN

Master of Engineering in Mechatronics Engineering,
China University of Petroleum (east China), China
born in Guigang, China.

This dissertation has been approved by the promotors

Prof. dr. P.G. Steeneken	Promotor
Dr. F. Alijani	Copromotor

Composition of the doctoral committee:

Rector Magnificus,	chairperson
Prof. dr. P.G. Steeneken,	Delft University of Technology
Dr. F. Alijani,	Delft University of Technology
Independent members:	
Prof. dr. ir. H.S.J. van der Zant	Delft University of Technology
Prof. dr. P.K. Lam	Agency for Science, Technology and Research, Singapore
Prof. dr. J. Twamley	Okinawa Institute of Science and Technology, Japan
Prof. dr. A.V. Metrikine	Delft University of Technology
Dr. S. Hanay	Bilkent University, Turkey

Keywords: Diamagnetic levitation, dynamics, resonator, damping mechanism, *Q* factor, eddy currents, MEMS, mass sensor, accelerometer, nonlinear dynamics, composite

Printed by: Ipskamp Printing

Front & Back: Diamagnetic levitation

ISBN 978-94-6384-418-5

An electronic version of this dissertation is available at
http://repository.tudelft.nl/.

To my family.

CONTENTS

SUMMARY

Powered by the silicon revolution, microelectromechanical systems (MEMS) have made their way into people's every-day life. The accelerometers in smart phones, gyroscopes in game controllers and inkjet printers in offices are a few examples. By looking at the resonance of MEMS, ultra-sensitive sensors can be realized. In pursuit of low-noise in these devices, reducing damping becomes critical. Among different damping sources, dissipation through clamping points can be viewed as a dominant source that can be quenched by levitation.

Among different levitation schemes, diamagnetic levitation stands out as the only passive method that does not require continuous energy supply. Moreover, due to the relatively strong magnetic potential, it can enable levitation of macroscopic objects which are beneficial for developing ultra-sensitive accelerometers, gravimeters as well as sensors for exploring macroscopic limits of quantum mechanics. Even though there already exist plenty of studies and applications about diamagnetic levitation, its dynamics is not yet fully understood and modeled. In this thesis, we study both the rigid body and elastodynamics of diamagnetically levitating resonators, theoretically and experimentally.

In Chapter 2, we focus on the linear rigid body dynamics of diamagnetically levitating resonators. By modeling and measuring the levitation height and resonance frequencies of millimeter graphite resonators, we investigate their stiffness change due to the magnetic field. By measuring the Q factors of the resonators in high vacuum, we reveal that eddy current damping is the underlying mechanism of energy dissipation in these resonators, and further highlight the size dependency of Q.

After identifying that eddy currents are the root cause of energy dissipation in diamagnetically levitating resonators, in chapter 3 we present a route to suppress eddy currents by fabricating diamagnetic composites. We disperse micro graphite particles inside epoxy matrix and fabricate macroscopic composites that demonstrate Q factors above 450,000, which are more than 400 times higher than graphite plates with similar dimensions. We then study the sensitivity of eddy currents to graphite particle size, volume fraction and plate length, and show that these composites can achieve acceleration noise floors as low as superconducting levitation systems that operate at cryogenic temperatures.

In Chapter 4, we drive a levitating graphite resonator into the nonlinear regime to study its nonlinear dynamic response. We actuate the levitating resonator into resonance using base excitation and probe its nonlinear stiffness induced merely by the magnetic force. We show that the levitating resonator exhibit softening type nonlinearity and deviates from the common Duffing type nonlinearity due to the strongly asymmetric magnetic force. Furthermore, we study the nonlinear damping originating from eddy currents and squeeze-film gas damping when the resonator vibrates at large amplitudes. By measuring and modeling the nonlinear frequency response in both air and vacuum

conditions, we show that the nonlinearity of eddy current damping is negligible, while the air damping has a significant effect.

Finally, in Chapter 5 we investigate the elastodynamics of a levitating resonator and develop a mass sensor based on its frequency shift. We first characterize the first 10 bending modes of the levitating resonator experimentally, and then construct an analytical model to compare them with the modeled resonance frequencies. Next, we use the third bending mode of the resonator to develop a levitating mass sensor and calibrate its mass responsivity using micro glass beads. We validate the sensor, by measuring the density of different kinds of liquids, and detecting the real-time evaporation of water droplets. Finally, by measuring the Allan deviation of the sensor's frequency stability, we show that it can resolve mass changes down to 4 ng.

In Chapter 6, we conclude the main findings about diamagnetic levitation from this thesis and give the outlook and recommendations for future directions.

SAMENVATTING

Micro-elektromechanische systemen (MEMS) hebben een plaats gevonden in ons dagelijks leven als gevolg van de revolutie in de halfgeleiderindustrie. Versnellingssensoren in smart phones, gyroscopen in spelcontrollers en inkjet printers in kantoren zijn een paar voorbeelden van toepassingen van MEMS. Ultra-gevoelige sensoren kunnen worden gerealiseerd door de resonantiefrequentie van MEMS te meten. Om de ruis in deze apparaten te verlagen, is vermindering van dissipatie essentieel. Van de verschillende dempingsbronnen is dissipatie via de verankeringspunten van de resonator meestal dominant, en door de resonator te laten zweven kan deze bron van demping geëlimineerd worden.

Van de verschillende levitatie methodes, is diamagnetische levitatie uniek, omdat het de enige techniek die geen continu vermogen vraagt, en dus volledig passief werkt bij kamertemperatuur. Bovendien maakt deze techniek het mogelijk, via de relatief sterke magnetische potentiaal, om macroscopische objecten te laten zweven en zo ultra-gevoelige accelerometers, gravimeters, en sensoren voor het meten van de macroscopische limieten van de kwantummechanica te realiseren. Ook al zijn er al veel studies en toepassingen van diamagnetische levitatie, toch is de dynamica van diamagnetisch zwevende objecten nog niet volledig begrepen en gemodelleerd. In dit proefschrift bestuderen we resonanties van zowel starre als flexibele diamagnetisch zwevende lichamen met theoretische en experimentele methodes.

In hoofdstuk 2 richten we ons op de lineaire dynamica van resonerende, diamagnetisch leviterende, starre lichamen. Via modellen en metingen van de levitatiehoogte en resonantiefrequentie van grafiet resonatoren met afmetingen op de millimeterschaal, onderzoeken we hun stijfheidsverandering als gevolg van het magneetveld. Door de kwaliteitsfactoren Q van de resonatoren te meten in hoog vacuum, laten we zien dat demping door eddy wervelstromen het onderliggende dempingsmechanisme is, en tonen we de afmetingsafhankelijkheid van dit dempingsmechanisme aan.

Na de vaststelling dat eddy stromen de oorzaak van energiedissipatie zijn, presenteren we in hoofdstuk 3 een methode om deze eddy stromen te onderdrukken door diamagnetische composieten te fabriceren. We dispergeren microscopische grafiet deeltjes in een epoxy matrix en fabriceren macroscopische composieten die Q factoren van boven de 450,000 laten zien, meer dan 400 keer hoger dan grafiet plaatjes van dezelfde afmetingen. We bestuderen daarna de afhankelijkheid van de eddy stromen van de deeltjesgrootte, volumefractie en plaat lengte, en tonen aan dat deze composieten bij kamertemperatuur een acceleratie ruisvloer kunnen bereiken die even laag is als die van supergeleidende leviterende systemen bij cryogene temperaturen.

In hoofdstuk 4, drijven we een leviterende grafiek resonator zo hard aan dat deze het niet-lineaire regime bereikt om zo zijn niet-lineair dynamische response te bestuderen. We actueren de zwevende resonator bij zijn resonantiefrequentie met behulp van basis aandrijving en meten de niet-lineaire stijfheid die puur door de magnetische kracht

wordt veroorzaakt. We laten zien dat deze resonator een 'softening' niet-lineariteitseffect laat zien dat afwijkt van de normale niet-lineariteit van het Duffing-type, als gevolg van de sterk asymmetrische magnetische kracht. Daarnaast bestuderen we de niet-lineaire dempingseigenschappen die hun oorsprong vinden in de eddy stromen en het squeeze-film gasdempingseffect als de resonator trilt met grote amplitudes. Door het meten en modeleren van de niet-lineaire frequentieresponse, zowel in lucht als in vacuum, tonen we aan dat de niet-lineariteit als gevolg van eddy stromen verwaarloosbaar is, terwijl gas demping een significant effect heeft.

Tenslotte onderzoeken we in hoofdstuk 5 de elastodynamica van een zwevende resonator en ontwikkelen een massa sensor die gebaseerd is op frequentieverschuivingen. We karakteriseren de resonantiefrequenties van eerste 10 buigmodes van de zwevende resonator experimenteel en vergelijken die met een analytisch model. Vervolgens, gebruiken we de derde buigmode om een zwevende massameter te ontwikkelen en kalibreren we de sensor met microscopische glaskralen. We valideren de sensor door de dichtheid van verschillende vloeistoffen te meten en door het verdampen van waterdruppels te meten. Tenslotte tonen we aan, door het bepalen van de Allan deviation van resonator's frequentiestabiliteit, dat deze een oplossend vermogen heeft dat groot genoeg is om massa veranderingen van slechts 4 nanogram te detecteren.

In hoofdstuk 6, concluderen we door de belangrijkste bevindingen over diamagnetische levitatie samen te vatten, kijken we vooruit en geven aanbevelingen voor toekomstige onderzoeksrichtingen.

1

INTRODUCTION

In this chapter, we give an introduction to micro-electromechanical resonators and the current research status of diamagnetic levitation. We explain the motivation for studying diamagnetic levitation and formulate the research question of this thesis.

1

1.1. BACKGROUNDS

Micro- and nano-electromechanical systems (MEMS/NEMS) are advancing our society, ranging from people's daily life [1] to fundamental science [2]. The rapid development of MEMS/NEMS is due to their miniaturized size and compact structure, which enable them to develop highly sensitive sensors with low cost at large scale. As most MEMS/NEMS have one or more parts that undergo motion, studying the resonances of MEMS/NEMS has become a topic of great importance and has lead to new applications. By coupling the resonance frequencies to external quantities, such as force or mass, ultra-sensitive sensors that can detect force at zeptonewton scale [3] and mass of single molecules [4] have been developed. Within these resonant sensors, the detection limit is influenced by quality factor (Q factor), which is the measure of energy dissipation. A higher Q factor means that the resonator's energy is less dissipated, and this is beneficial to increase the sensitivity of resonant sensors [5]. Among different kinds of energy dissipation sources, damping through the clamping points in the form of acoustic loss is dominant in many resonant systems. In literature, great efforts have been paid to reduce the clamping loss by soft clamping [6] or confining the energy within a certain frequency band gap using phononic crystal structures [7]. However, the ultimate method to prevent the energy leaking from a resonator through clamping points is by levitation [8, 9].

1.2. LEVITATION SCHEMES

Levitation enables an object to be free from clamping and well isolated from its environment. This not only has the potential to significantly reduce the energy loss of the levitating system, but also enables unconstrained high-precision control of the object. Levitation can be realised in different ways, using aerodynamic, acoustic, optical, electrical and magnetic forces [8, 9]. Aerodynamic or acoustic radiation force can be used to levitate any material and, thereby, has a great potential in contact-less transportation and manipulation of objects [10, 11]. However, since these levitation schemes require air as a medium for generating the levitation force, aerodynamic and acoustic levitation are not able to operate in vacuum conditions. Thus, their performance is limited by air damping and they are not conventionally used for sensing applications. For ultra-sensitive sensors, attention has moved to optical, electrical and magnetic levitation, see Fig. 1.1 for examples.

OPTICAL AND ELECTRICAL LEVITATION

Decades after its first demonstration in the 1970s [15], optical levitation (see Fig. 1.1a) has became the most popular scheme among different levitation methods in pursuit of ultra-sensitive sensors and platforms for quantum opto-mechanics [3, 12, 16–18]. This is not only because optically levitating systems can be easily integrated with light for detection and motion control, but also due to their advantages ranging from being compatible to many kinds of materials, having high resonance frequencies and controllable levitation potentials. The remaining issues for optical levitation are that the levitating particles tend to escape the optical trap before high vacuum can be attained, therefore feedback control is always required for long-term stability in high vacuum [19]. Moreover, the optically trapped objects suffer from both the laser recoil heating [20] and the

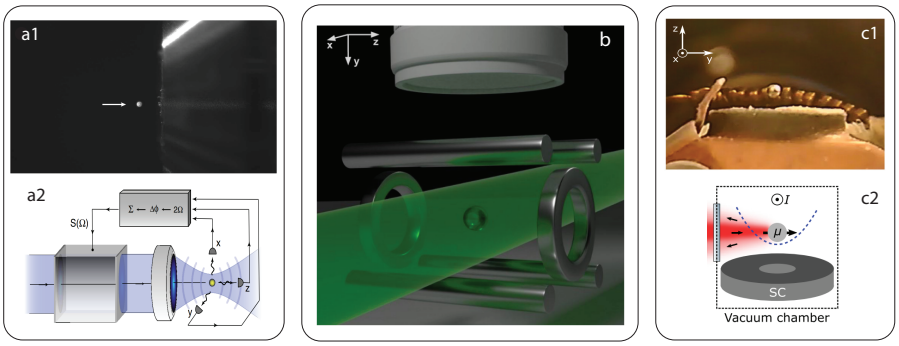

Figure 1.1: Different levitation schemes. (a) Optical levitation of a 140 nm silica particle [12] inside an optical potential; (b) Electrical levitation of a 460 nm silica particle in a Paul trap [13]; (c) Superconducting levitation of a 0.5 mm neodymium magnet sphere above a lead superconducting disk [14].

internal heating via absorption of laser light [21]. These drawbacks influence their performance and limit their applications. To overcome the deficiencies of optical levitation, electrical levitation (see Fig. 1.1b) is a promising technique for trapping charged dielectric micro/nano particles using a Paul trap [13, 22] that uses a rapidly varying dynamic electric field to eliminate electrostatic instabilities due to Earnshaw's theorem. Free from internal heating and having large potential depth, electrical levitation has been used as an opto-mechanical platform for testing wave-function collapse models [13, 23, 24]. The challenge of electric levitation is their dependence on the continuous energy input for generating the levitation force. Adding to this, electrically levitated objects may suffer from noise and drift from the applied electric fields [25].

MAGNETIC LEVITATION

Another method for defying gravity is magnetic levitation. Magnetic levitation can be categorized into electromagnetic, superconducting and diamagnetic levitation based on their working principles. Electromagnetic levitation is the most commonly known and used magnetic levitation method, for instance, in maglev trains [26] or precision stages [27]. Magnetic force is generated by actively controlled magnetic fields through electromagnetic coils, which enables high speed contact-less motion and precision control of bodies. Apart from the active electromagnetic levitation method, many kinds of materials with negative magnetic susceptibility can be levitated by diamagnetic force [28]. In a particular case, superconductors are considered to be a perfect diamagnetic material with magnetic susceptibility of -1 that can completely expel magnetic fields due to the Meissner effect [29]. The levitation method using superconductors and diamagnetic force is called superconducting levitation, where either a superconductor [30] or a magnet [31] is levitated. Among these two schemes, levitating a magnet above a superconductor is more attractive for sensing applications [14] or exploring quantum mechanics [31], since it is easier to maintain the low temperature of the superconductor as a substrate.

The last levitation method that is implemented using diamagnetic force is diamag-

1

netic levitation. Normally, diamagnetic levitation is referred to as the levitation of a diamagnetic material above magnets [32] or the levitation of a permanent magnet above a diamagnetic material [33]. In contrast to electromagnetic levitation, that requires energy to generate magnetic field and feedback control, or superconducting levitation that has to operate at cryogenic temperature to prepare the material into the diamagnetic state, diamagnetic levitation with permanent magnets is a completely passive method that does not require any energy supply and can operate at room temperature.

1.3. DIAMAGNETIC LEVITATION

1.3.1. DIAMAGNETISM

Materials can be classified into diamagnetic, paramagnetic, ferromagnetic, antiferromagnetic and ferrimagnetic materials based on their magnetization in an external magnetic field. Among the five categories, paramagnetic and diamagnetic materials exhibit no collective magnetic interactions and are not magnetically ordered at the atomic scale, and their magnetization **M** to an external magnetic field can be written as [34]:

$$\mathbf{M} = \chi \mathbf{H}, \tag{1.1}$$

where χ is the magnetic susceptibility of the material, and **H** is the externally applied magnetic field. For diamagnetic materials $\chi < 0$ and the induced magnetization is opposite to the applied magnetic field, therefore the materials will be repelled by the magnetic field; for paramagnetic materials $\chi > 0$ and the induced magnetization is parallel to the applied magnetic field, therefore the materials will be attracted by the magnetic field (see Fig. 1.2). In nature, there are many kinds of materials that present the property of diamagnetism, such as bismuth, graphite, water and wood [28].

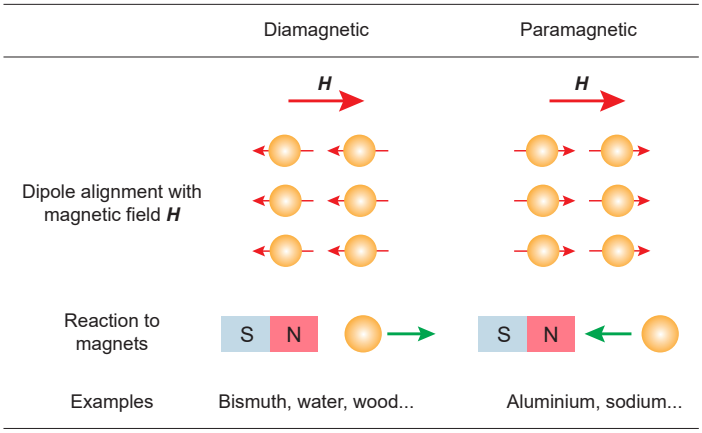

Figure 1.2: Difference between diamagnetic and paramagnetic materials. The dipole alignment of diamagnetic materials is opposite to the applied external magnetic field **H**, thus diamagnetic materials are repelled by magnetic field; in contrast, the dipole alignment of paramagnetic materials is parallel to the applied external magnetic filed **H**, thus paramagnetic materials are attracted by magnetic field. The green arrows indicate the magnetic forces experienced by the materials.

Due to the negative susceptibility and repelling magnetic force, stable diamagnetic levitation becomes an exception to Earnshaw's theorem [35] and was first demonstrated by Lord Kelvin by the successful levitation of a bismuth sample [36]. When a diamagnetic object is placed inside a magnetic field, the total magnetic force from the field on the object $\mathbf{F_B}$ is determined as

$$\begin{aligned}\mathbf{F_B} &= \nabla \int_{\mathcal{V}} \mathbf{M}\cdot\mathbf{B}\mathrm{d}\mathcal{V} \\ &= \frac{\mu_0}{2}\int_{\mathcal{V}} \nabla(\chi_x H_x^2 + \chi_y H_y^2 + \chi_z H_z^2)\mathrm{d}\mathcal{V},\end{aligned} \tag{1.2}$$

where $\mathcal{V}$ is the volume of the diamagnetic object, $H_{x,y,z}$ are the components of the magnetic field strength, $\mathbf{M}$ is the magnetization, $\mathbf{B} = \mu_0\mathbf{H}$ is the magnetic flux density in vacuum and μ_0 is the magnetic permeability of vacuum. Since the diamagnetic susceptibility χ is relatively small in the diamagnetic materials we study in this thesis, the approximation $B = (1+\chi)\mu_0 H \approx \mu_0 H$ is made in equation (1.2). When the magnetic force counteracting the gravitational force is sufficiently strong, an object can be levitated.

1.3.2. STATE-OF-THE-ART STUDIES ON DIAMAGNETIC LEVITATION

Over the last decades, diamagnetic levitation has been developing fast with the successful levitation of a wide range of materials, and it has been applied in many areas such as metrology, energy harvesting and motion manipulation, as shown in Fig. 1.3.

The most well known experiment of diamagnetic levitation might be the successful levitation of a frog in a magnetic field of 16 T [28] and the levitation of a permanent magnet between two fingertips [37], as shown in Fig. 1.3a and b, respectively. Even though the above two experiments required dramatic power to enable the magnetic field, they opened a new chapter for diamagnetic levitation. With miniaturised size, diamagnetic objects can be levitated by permanent magnets with a relatively weak magnetic field. Over the last decades, levitation of a wide range of materials, including water [38], borosilicate [39], graphite [40], polyethylene glycol [41], poly (methyl methacrylate) (PMMA) [48], silica [49], cells [50], has been demonstrated using different permanent magnet arrangements. Among these, levitation of pyrolytic graphite is the most common method since its magnetic susceptibility at room temperature is the largest. Therefore, pyrolytic graphite structures with dimensions of centimeters can be easily levitated by commercially available permanent magnets (Fig. 1.3e,g,k,l,m). Regarding other materials with relatively weaker diamagnetism, special design of the magnetic field is needed, and only objects with smaller dimensions can be levitated (see Fig. 1.3c,d,f,j).

Due to the advantages of passive levitation and being free from clamping loss, diamagnetically levitating systems have been developed into a wide range of sensors, including accelerometers [39–41], force sensors [42] and viscosity/density sensors [51]. Being able to levitate a large mass and operate at low frequencies, these systems have also shown potentials for vibration energy harvesting [33, 43]. These energy harvesters tend to levitate permanent magnets since their mass is bigger. Furthermore, due to the absence of mechanical friction and constraints, diamagnetic levitation is the technique of choice in motion control and manipulation of objects. Using diamagnetic levitation,

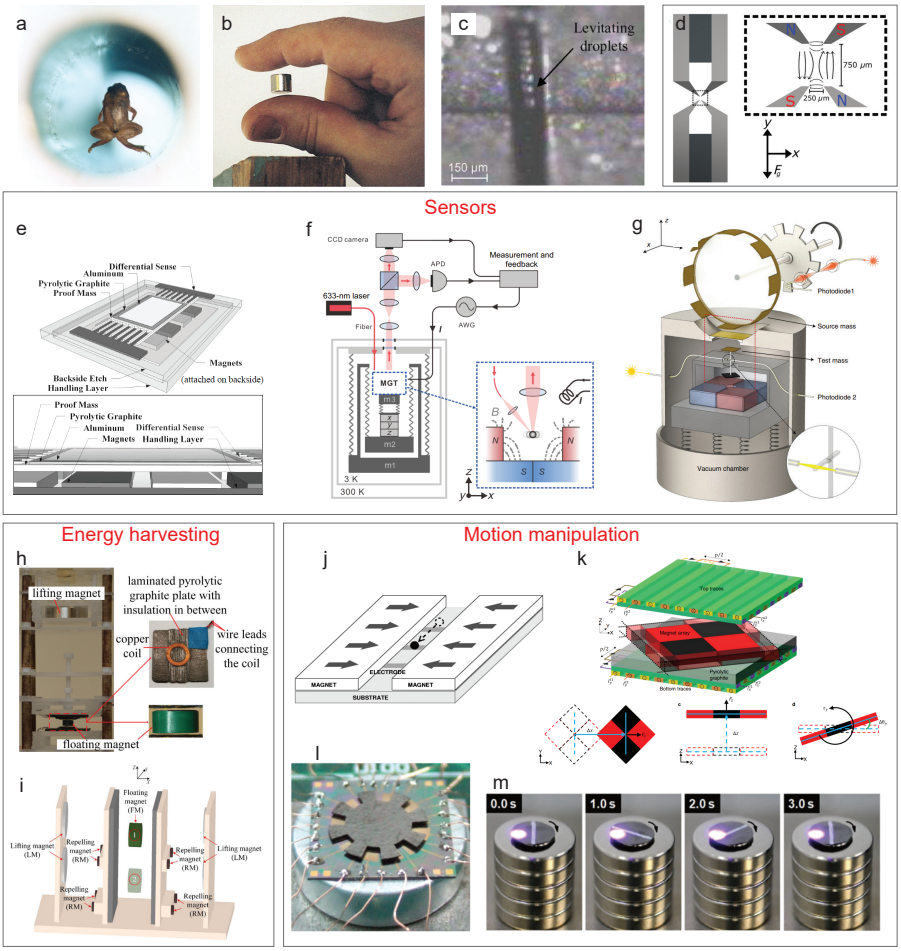

Figure 1.3: Examples of diamagnetic levitation. (a) Levitation of a frog above a 16T magnetic field [28]; (b) Levitation of a NdFeB magnet stabilized by fingertips [37]; (c) Levitation of ~ 30 μm water microdroplets above permanent magnets [38]; (d) A 3D magneto-gravitational trap consisting of samarium-cobalt permanent magnets that is able to levitate ~ 60 μm borosilicate particles [39]; (e) Diamagentically levitated MEMS accelerometers above a checkerboard configuration of magnets [40]; (f) A diamagnetically levitated 7.8 μm polyethylene glycol resonator with ultra-low damping and $Q = 2 \times 10^7$ [41]; (g) An ultra-sensitive force sensor at sub-milligram scales for testing theories of dark energy [42]; (h) A vibration energy harvester based on vertical diamagnetic levitation [33]; (i) A low frequency vibration energy harvester based on horizontal diamagnetic levitation [43]; (j) A diamagnetically levitating particle moving by current pulses through electrodes [44]; (k) A precision diamagnetically levitated nanopositioner with large range and six degrees-of-freedom [45]; (l) A graphite rotor levitating above permanent magnets and driven by electrostatic forces [46]; (m) A diamangetically levitated graphite plate that can be moved by laser irradiation [47].

contact-less transportation of micro particles or droplets have been demonstrated [44]. Integrated with dedicated circuits and control methods, levitating stages with six degree-of-freedoms and nanometer accuracy have been implemented [45]. Using round perma-

nent magnets, frictionless rotors controlled through electrostatic or light-thermal force have also been realized [46, 47].

The previous works have laid the foundation of diamagnetic levitation, ranging from the basic theory of diamagnetism to novel applications. This makes diamagnetic levitation a promising technique for the development of next-generation unclamped micro electromechanical systems. However, the damping mechanism of diamagnetically levitating systems is not fully understood, and its nonlinear and elastodynamics are rarely exploited.

1.4. AIM OF THIS RESEARCH

The main aim of this thesis is to study the dynamics of diamagnetically levitating resonators to provide profound understanding of their stiffness and dissipation mechanisms, which can be used for realizing ultra-low noise devices and extremely sensitive sensors. To achieve the goal, the following research questions are formulated:

- What is the dominant source of energy dissipation in a levitating resonator?
- How to reduce the damping and increase the Q factor of a levitating resonator?
- How does the nonlinear dynamics of these levitating resonators look like in a magnetic potential well?
- How do diamagnetically levitating resonators perform as real-time density and mass sensors?

To answer these questions, a levitation system consisting of four permanent magnets and a diamagnetic plate is investigated through experimental and theoretical studies. These studies will provide insights into low-frequency rigid body dynamics, high-frequency elastodynamics, and nonlinear dynamics.

1.5. THIS THESIS

In this thesis, we study the rigid body and elastodynamics of a diamagnetic plate that stably levitates above a checkerboard array of permanent magnets, analytically and experimentally. The main Chapters except for Chapter 1 and Chapter 6 are based on four published or to be submitted journal articles. The structure of the thesis is shown in Fig. 1.4.

Specifically, in Chapter 1, we first give an introduction to different kinds of levitation schemes and then the theory and state-of-the-art studies of diamagnetic levitation. In Chapter 2, we focus on the rigid body dynamics of a diamagnetically levitating graphite plate. To understand the resonance frequency and damping mechanism, we conduct dynamic measurements in a vacuum condition to get rid of the influence of air damping. Using numerical methods, we find out that the dissipation source in a diamagnetically levitating object is eddy currents and then study its dependency to plate size. Based on these findings, in Chapter 3, we demonstrate a new route for reducing eddy current damping by dispersing graphite particles in an epoxy matrix, and eventually increase

the Q factor of a diamagnetically levitating resonator by two orders. Apart from the linear dynamics, in Chapter 4, we actuate the levitating resonator into nonlinear regime and study its nonlinear dynamic response. This study provides new understandings on the role of nonlinear magnetic stiffness and air damping on nonlinear dynamics of these levitating systems. In Chapter 5, we emphasize on elastodynamics and characterize the elastic modes of these resonators in kHz regime. Using the shift in resonance frequencies, we then develop a sensitive mass sensor with a resolution down to nanogram and validate it by measuring the evaporation of water droplets. Finally, we conclude and summarize the research conducted in this thesis and provide an outlook for future research in Chapter 6.

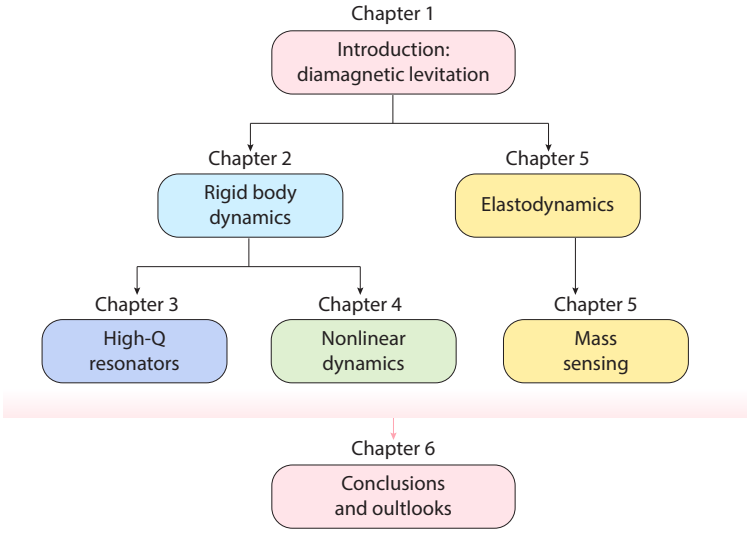

Figure 1.4: Structure of this thesis.

REFERENCES

[1] C. Lam, "A review of the recent development of mems and crystal oscillators and their impacts on the frequency control products industry", in 2008 ieee ultrasonics symposium (IEEE, 2008), pp. 694–704.

[2] S. Barzanjeh, A. Xuereb, S. Gröblacher, M. Paternostro, C. A. Regal, and E. M. Weig, "Optomechanics for quantum technologies", Nature Physics **18**, 15–24 (2022).

[3] G. Ranjit, M. Cunningham, K. Casey, and A. A. Geraci, "Zeptonewton force sensing with nanospheres in an optical lattice", Physical Review A **93**, 053801 (2016).

[4] A. K. Naik, M. Hanay, W. Hiebert, X. Feng, and M. L. Roukes, "Towards single-molecule nanomechanical mass spectrometry", Nature nanotechnology **4**, 445–450 (2009).

[5] S. Schmid, L. G. Villanueva, and M. L. Roukes, *Fundamentals of nanomechanical resonators*, Vol. 49 (Springer, 2016).

[6]M. J. Bereyhi, A. Beccari, R. Groth, S. A. Fedorov, A. Arabmoheghi, T. J. Kippenberg, and N. J. Engelsen, "Hierarchical tensile structures with ultralow mechanical dissipation", Nature Communications **13**, 1–9 (2022).

[7]Y. Tsaturyan, A. Barg, E. S. Polzik, and A. Schliesser, "Ultracoherent nanomechanical resonators via soft clamping and dissipation dilution", Nature nanotechnology **12**, 776–783 (2017).

[8]E. Brandt, "Levitation in physics", Science **243**, 349–355 (1989).

[9]C. Gonzalez-Ballestero, M. Aspelmeyer, L. Novotny, R. Quidant, and O. Romero-Isart, "Levitodynamics: levitation and control of microscopic objects in vacuum", Science **374**, eabg3027 (2021).

[10]J. A. Schetz, "Aerodynamics of high-speed trains", Annual Review of fluid mechanics **33**, 371 (2001).

[11]M. A. Andrade, N. Pérez, and J. C. Adamowski, "Review of progress in acoustic levitation", Brazilian Journal of Physics **48**, 190–213 (2018).

[12]F. van der Laan, F. Tebbenjohanns, R. Reimann, J. Vijayan, L. Novotny, and M. Frimmer, "Sub-kelvin feedback cooling and heating dynamics of an optically levitated librator", Physical Review Letters **127**, 123605 (2021).

[13]A. Pontin, N. Bullier, M. Toroš, and P. Barker, "Ultranarrow-linewidth levitated nanooscillator for testing dissipative wave-function collapse", Physical Review Research **2**, 023349 (2020).

[14]C. Timberlake, G. Gasbarri, A. Vinante, A. Setter, and H. Ulbricht, "Acceleration sensing with magnetically levitated oscillators above a superconductor", Applied Physics Letters **115**, 224101 (2019).

[15]A. Ashkin and J. Dziedzic, "Optical levitation by radiation pressure", Applied Physics Letters **19**, 283–285 (1971).

[16]J. Ahn, Z. Xu, J. Bang, P. Ju, X. Gao, and T. Li, "Ultrasensitive torque detection with an optically levitated nanorotor", Nature Nanotechnology **15**, 89–93 (2020).

[17]F. Tebbenjohanns, M. L. Mattana, M. Rossi, M. Frimmer, and L. Novotny, "Quantum control of a nanoparticle optically levitated in cryogenic free space", Nature **595**, 378–382 (2021).

[18]D. C. Moore and A. A. Geraci, "Searching for new physics using optically levitated sensors", Quantum Science and Technology **6**, 014008 (2021).

[19]F. Monteiro, S. Ghosh, A. G. Fine, and D. C. Moore, "Optical levitation of 10-ng spheres with nano-g acceleration sensitivity", Physical Review A **96**, 063841 (2017).

[20]V. Jain, J. Gieseler, C. Moritz, C. Dellago, R. Quidant, and L. Novotny, "Direct measurement of photon recoil from a levitated nanoparticle", Physical review letters **116**, 243601 (2016).

[21]J. Millen, T. Deesuwan, P. Barker, and J. Anders, "Nanoscale temperature measurements using non-equilibrium brownian dynamics of a levitated nanosphere", Nature nanotechnology **9**, 425–429 (2014).

[22] L. Dania, D. S. Bykov, M. Knoll, P. Mestres, and T. E. Northup, "Optical and electrical feedback cooling of a silica nanoparticle levitated in a paul trap", Physical Review Research **3**, 013018 (2021).

[23] D. Goldwater, M. Paternostro, and P. Barker, "Testing wave-function-collapse models using parametric heating of a trapped nanosphere", Physical Review A **94**, 010104 (2016).

[24] A. Vinante, A. Pontin, M. Rashid, M. Toroš, P. Barker, and H. Ulbricht, "Testing collapse models with levitated nanoparticles: detection challenge", Physical Review A **100**, 012119 (2019).

[25] N. Bullier, A. Pontin, and P. Barker, "Characterisation of a charged particle levitated nano-oscillator", Journal of Physics D: Applied Physics **53**, 175302 (2020).

[26] H.-W. Lee, K.-C. Kim, and J. Lee, "Review of maglev train technologies", IEEE transactions on magnetics **42**, 1917–1925 (2006).

[27] A. Pirati, J. van Schoot, K. Troost, R. van Ballegoij, P. Krabbendam, J. Stoeldraijer, E. Loopstra, J. Benschop, J. Finders, H. Meiling, et al., "The future of euv lithography: enabling moore's law in the next decade", in Extreme ultraviolet (euv) lithography viii, Vol. 10143 (SPIE, 2017), pp. 57–72.

[28] M. Simon and A. Geim, "Diamagnetic levitation: flying frogs and floating magnets", Journal of applied physics **87**, 6200–6204 (2000).

[29] C. P. Poole, H. A. Farach, and R. J. Creswick, *Superconductivity* (Academic press, 2013).

[30] M. G. Latorre, A. Paradkar, D. Hambraeus, G. Higgins, and W. Wieczorek, "A chip-based superconducting magnetic trap for levitating superconducting microparticles", IEEE Transactions on Applied Superconductivity **32**, 1–5 (2022).

[31] J. Gieseler, A. Kabcenell, E. Rosenfeld, J. Schaefer, A. Safira, M. J. Schuetz, C. Gonzalez-Ballestero, C. C. Rusconi, O. Romero-Isart, and M. D. Lukin, "Single-spin magnetomechanics with levitated micromagnets", Physical review letters **124**, 163604 (2020).

[32] R. D. Waldron, "Diamagnetic levitation using pyrolytic graphite", Review of Scientific Instruments **37**, 29–35 (1966).

[33] S. Palagummi and F. Yuan, "An optimal design of a mono-stable vertical diamagnetic levitation based electromagnetic vibration energy harvester", Journal of Sound and Vibration **342**, 330–345 (2015).

[34] N. Ida et al., *Engineering electromagnetics* (Springer, 2015).

[35] S. Earnshaw, "On the nature of the molecular forces which regulate the constitution of the luminiferous ether", Transactions of the Cambridge Philosophical Society **7**, 97 (1848).

[36] G. Kustler, "Diamagnetic levitation-historical milestones", Revue Roumaine Des Sciences Techniques Serie Electrotechnique Et Energetique **52**, 265 (2007).

[37] A. Geim, M. Simon, M. Boamfa, and L. Heflinger, "Magnet levitation at your fingertips", Nature **400**, 323–324 (1999).

[38]H. Chetouani, C. Jeandey, V. Haguet, H. Rostaing, C. Dieppedale, and G. Reyne, "Diamagnetic levitation with permanent magnets for contactless guiding and trapping of microdroplets and particles in air and liquids", IEEE Transactions on Magnetics **42**, 3557–3559 (2006).

[39]C. W. Lewandowski, T. D. Knowles, Z. B. Etienne, and B. D'Urso, "High-sensitivity accelerometry with a feedback-cooled magnetically levitated microsphere", Physical Review Applied **15**, 014050 (2021).

[40]D. Garmire, H. Choo, R. Kant, S. Govindjee, C. Sequin, R. Muller, and J. Demmel, "Diamagnetically levitated mems accelerometers", in Transducers 2007-2007 international solid-state sensors, actuators and microsystems conference (IEEE, 2007), pp. 1203–1206.

[41]Y. Leng, R. Li, X. Kong, H. Xie, D. Zheng, P. Yin, F. Xiong, T. Wu, C.-K. Duan, Y. Du, et al., "Mechanical dissipation below 1 μ hz with a cryogenic diamagnetic levitated microoscillator", Physical Review Applied **15**, 024061 (2021).

[42]P. Yin, R. Li, C. Yin, X. Xu, X. Bian, H. Xie, C.-K. Duan, P. Huang, J.-h. He, and J. Du, "Experiments with levitated force sensor challenge theories of dark energy", Nature Physics, 1–5 (2022).

[43]S. Palagummi, J. Zou, and F. Yuan, "A horizontal diamagnetic levitation based low frequency vibration energy harvester", Journal of Vibration and Acoustics **137** (2015).

[44]I. Lyuksyutov, D. Naugle, and K. Rathnayaka, "On-chip manipulation of levitated femtodroplets", Applied physics letters **85**, 1817–1819 (2004).

[45]K. Vikrant and G. Jayanth, "Diamagnetically levitated nanopositioners with large-range and multiple degrees of freedom", Nature Communications **13**, 1–11 (2022).

[46]W. Liu, W. Zhang, and W. Chen, "Simulation analysis and experimental study of the diamagnetically levitated electrostatic micromotor", Journal of Magnetism and Magnetic Materials **492**, 165634 (2019).

[47]M. Kobayashi and J. Abe, "Optical motion control of maglev graphite", Journal of the American Chemical Society **134**, 20593–20596 (2012).

[48]F. Xiong, P. Yin, T. Wu, H. Xie, R. Li, Y. Leng, Y. Li, C. Duan, X. Kong, P. Huang, et al., "Lens-free optical detection of thermal motion of a submillimeter sphere diamagnetically levitated in high vacuum", Physical Review Applied **16**, L011003 (2021).

[49]B. R. Slezak, C. W. Lewandowski, J.-F. Hsu, and B. D'Urso, "Cooling the motion of a silica microsphere in a magneto-gravitational trap in ultra-high vacuum", New Journal of Physics **20**, 063028 (2018).

[50]H. Chetouani, V. Haguet, C. Jeandey, C. Pigot, A. Walther, N. Dempsey, F. Chatelain, B. Delinchant, and G. Reyne, "Diamagnetic levitation of beads and cells above permanent magnets", in Transducers 2007-2007 international solid-state sensors, actuators and microsystems conference (IEEE, 2007), pp. 715–718.

[51]S. Clara, H. Antlinger, A. Abdallah, E. Reichel, W. Hilber, and B. Jakoby, "An advanced viscosity and density sensor based on diamagnetically stabilized levitation", Sensors and Actuators A: Physical **248**, 46–53 (2016).

2

RIGID BODY DYNAMICS OF DIAMAGNETICALLY LEVITATING GRAPHITE RESONATORS

Diamagnetic levitation is a promising technique for realizing resonant sensors and energy harvesters, since it offers thermal and mechanical isolation from the environment at zero power. To advance the application of diamagnetically levitating resonators, it is important to characterize their dynamics in the presence of both magnetic and gravitational fields. Here we experimentally actuate and measure rigid body modes of a diamagnetically levitating graphite plate. We numerically calculate the magnetic field and determine the influence of magnetic force on the resonance frequencies of the levitating plate. By analyzing damping mechanisms, we conclude that eddy current damping dominates dissipation in mm-sized plates. We use finite element simulations to model eddy current damping and find close agreement with experimental results. We also study the size-dependent Q-factors (Qs) of diamagnetically levitating plates and show that Qs above 100 million are theoretically attainable by reducing the size of the diamagnetic resonator down to microscale, making these systems of interest for next generation low-noise resonant sensors and oscillators.

Parts of this chapter have been published in Applied Physics Letters **116**, 243505 (2020) [1]

2.1. INTRODUCTION

Levitation, as the means to defy gravity, has always been a dream of mankind. This dream has been realized at large scale with the design of aircrafts, hovercrafts, and maglev trains, however, the potential of levitation is yet to be fully explored at small scale. Levitation requires forces that act in the absence of mechanical contact, like optical, acoustic, aerodynamic or magnetic forces [2]. Among them diamagnetic levitation stands out as the only means of stable levitation at room temperature that is passive, because it can be sustained indefinitely without feedback control or cooling systems that consume energy. Although stable levitation in a constant magnetic field may seem to be impossible, centuries back Lord Kelvin showed that there is an exception to Earnshaw's theorem: diamagnetic materials can levitate stably in a magnetic field [3]. One of the most renowned experiments in this respect is the levitation of a living frog using a 16.5 Tesla magnetic field [4]. That experiment required much power to drive large electromagnets, however at small scale the story is different because the magnetic field of permanent magnets is sufficient to overcome gravitational forces and enable levitation. During the last decades, levitation of liquid droplets [5, 6], cells [7] and solid particles [6] have been demonstrated using small permanent magnets. Moreover, this passive levitation has been used for realizing devices like accelerometers [8, 9], energy harvesters [10–12], viscosity/density sensors [13], and force sensors [14].

To realize highly sensitive resonant sensors, it is essential to characterize their frequency response and dissipation mechanisms, that are closely linked to the precision with which frequencies of a resonant sensor can be determined and that are intrinsically coupled to the thermomechanical noise floor via the fluctuation dissipation theorem [15]. In particular, minimization of damping is an essential consideration in the design of low phase noise oscillators and highly precise resonant sensors.

One of the most important dissipation mechanisms in Micro-Electro-Mechanical Systems (MEMS) is acoustic loss, which occurs when mechanical energy leaves the structure as sound waves, via the anchors or clamping points. In literature great efforts are undertaken to minimize acoustic loss by suspending resonators via thin, high-tension tethers [16] or optimized clamping points [17]. However, the ultimate way of eliminating acoustic losses is levitation in vacuum, since acoustic waves cannot propagate in the absence of matter. For this reason optical levitation has been applied to obtain high Q resonators [18]. Even though promising, this technique has the drawback that it requires high-power lasers, that can significantly increase the temperature of the levitating object and affect its microstructure. In this respect, zero power levitation of diamagnetic materials at room temperature combined with their vacuum compatibility make them ideal candidates for tackling this challenge. Moreover, since the main sources of dissipation in diamagnetic resonators are air and eddy current damping [10, 12, 19], by operating the resonator in vacuum, one can eliminate air damping so that the only remaining dissipative force is eddy current force which can be minimized to obtain high Q resonators.

In this Chapter we study the rigid body resonances and dissipation mechanisms of a diamagnetic resonator that levitates above permanent magnets at different pressures. The diamagnetic material used in our experiments is pyrolytic graphite which has large negative magnetic susceptibility and thus can levitate easily above permanent magnets.

In contrast to studies on conventional microelectromechanical resonators, these levitating resonators allow us to study the dynamics of nearly free-body objects, in the absence of mechanical clamping or anchor effects. Interestingly, the restoring force, that is generally provided by a compliant mechanical spring, is here provided by magnetic and gravitational forces. By using a laser Doppler vibrometer (LDV), 3 rigid body translational and 2 rotational modes of the plate are detected and their resonance frequencies and Qs are characterized experimentally. To understand the effect of air damping on our resonator, we perform experiments over a pressure range of 10^{-4} to 1000 mbar. This pressure-dependent study also allows us to study the effect of eddy current damping on plates of different sizes in vacuum. To get a deeper insight into the magnetically induced stiffness and eddy current damping of the resonator, numerical finite element method (FEM) models are used to simulate the magnetic force and eddy currents on the levitating plate. With our FEM model, the effect of plate size on the Q is studied, from which we conclude that the Qs of rigid body modes for diamagnetically levitating objects increases at small dimensions.

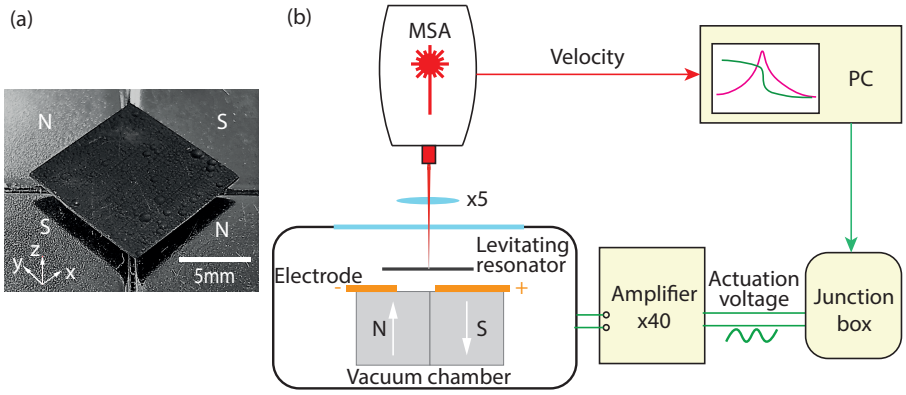

Figure 2.1: The levitating resonator and experimental setup. (a) Levitating pyrolytic graphite plate above 4 cubic Nickel coated NdFeB magnets with alternating magnetization, where N and S stand for north and south pole of the magnet, respectively. The origin of the coordinate system is at the center of the plate. (b) Schematic of the measurement setup comprising a MSA400 Polytec LDV for the read out and electrostatic excitation method. The actuation voltage is generated by the LDV junction box and is amplified by a 40 × voltage amplifier that drives the levitating plate into resonance using electrostatic actuation. The electrostatic force is generated via two electrodes beneath the levitating plate. By focusing MSA laser beam on the plate, the vibration signal is detected,and the acquired velocity is transferred to a PC for frequency response analysis.

2.2. EXPERIMENTAL SETUP

Pyrolytic graphite (from Magnetladen Seiler GmbH) is cut into square plates of different side length L using a laser cutter after which their surfaces are slightly polished using fine sand paper (5 μm grain) to a thickness of 280 microns. The literature values of the material properties of the pyrolytic graphite resonator used for experiments and simulations are given in Table 2.1. Our diamagnetic pyrolytic graphite plates are levitating above a checkboard arrangement of 4 cubic NdFeB ferromagnets (side length D=12 mm) with

Table 2.1: Material properties of the levitating pyrolytic graphite.

Property	Symbol	Value	Unit
Density	ρ	2070	kg/m^3
Susceptibility $\perp$ [4]	χ_z	-450	$\times 10^{-6}$
Susceptibility $\parallel$ [4]	$\chi_{x,y}$	-85	$\times 10^{-6}$
Conductivity $\perp$[20]	σ_z	200	S/m
Conductivity $\parallel$[20]	$\sigma_{x,y}$	200000	S/m

alternating magnetization (Fig. 2.1a). The remanent magnetic flux density of the cubic magnets is $B_r = 1.4\,\mathrm{T}$. The magnetic field gradient in the z-direction provides an upward force on the plate to compensate the gravitational force. Together with the lateral magnetic gradients it provides a stable energy minimum that determines the plate's rest position. The figure shows that we define x and y-axes along parallel to the plate edges.

To probe the motion of the levitating resonator, we use the experimental setup shown in Fig. 2.1b. It includes an MSA400 Polytec LDV that measures the out-of-plane speed of the plate. In our experiments, the excitation voltage is generated by LDV junction box that drives the levitating plate into resonance using electrostatic forces. These forces are generated via two electrodes (thin copper tapes isolated from the magnets, not shown in Fig. 2.1a) beneath the levitating plate. When a voltage is applied between the two electrodes (Fig. 2.1b), the levitating plate acts as a floating electrode between the two electrodes, thus forming a capacitive divider. In the area at which the plate overlaps with the electrodes, an electrostatic downward force is exerted that depends on the overlapping area, voltage difference, and gap size. In order to efficiently excite different modes of the plate, an asymmetric arrangement of the electrodes is used, as shown in Fig. 2.1b. Due to this asymmetry, the electrostatic forces between each of the electrodes and the plate are different, and generate both a translational force and a rotational moment on the plate. A periodic chirp voltage signal (V_{AC}=1.0 V) is superposed on an offset voltage (V_{DC}=-1.2 V) and amplified by a voltage amplifier (40×) that applies the voltage across the electrodes. The DC offset voltage is used to make sure that the electrostatic force, that is proportional to the square of the voltage, has a component of the same frequency as the chirp signal. With the LDV, the frequency response curves are measured, and by scanning the laser over the plate the mode shapes are obtained using the Polytec software. In this Chapter, the LDV measurements are conducted in a vacuum chamber over a pressure range of 10^{-4} to 1000 mbar because air damping is negligible when pressure is below 10^{-4} and it takes more time to reach to lower pressure.

2.3. RESULTS

2.3.1. MAGNETIC STIFFNESS

Since there are 3 translational and 3 rotational degrees-of-freedom, the plate is expected to exhibit 6 different rigid-body resonances. In Fig. 2.2a, the levitating plate is driven from 8 – 25 Hz, and 5 of these 6 rigid body modes are observed. These mode shapes, as obtained by LDV and from camera movies, are schematically shown in Fig. 2.2a. Movies of the detected mode shapes are also shown in supplementary material A1. The rota-

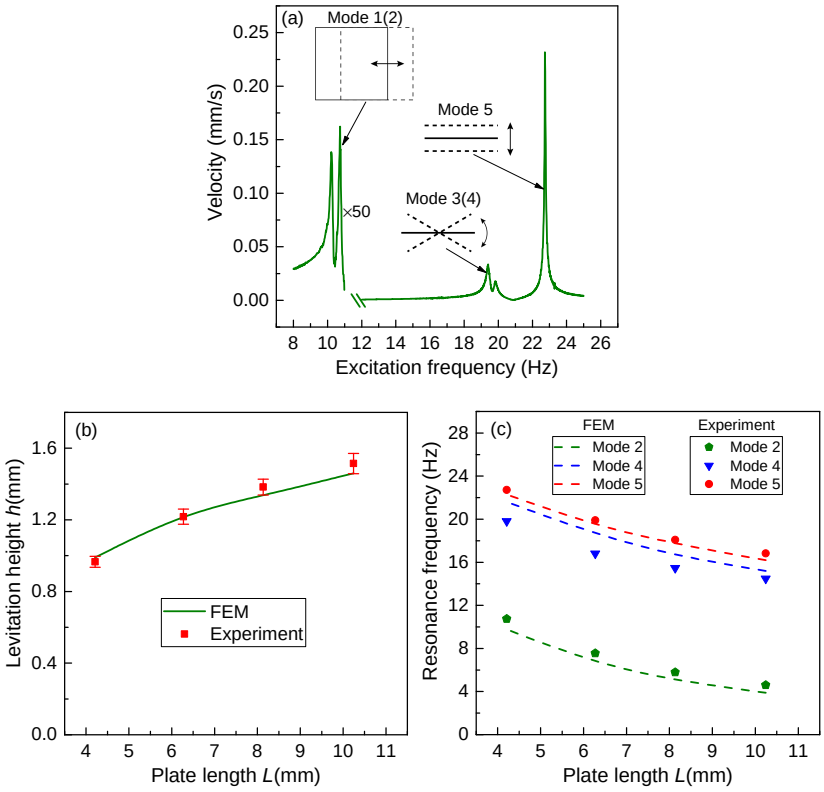

Figure 2.2: Dynamic characterization of the levitating resonator in its rigid body modes. (a) Frequency response curve of a $4.28 \times 4.14 \times 0.28\,\mathrm{mm}^3$ levitating graphite plate. The lowest frequency peaks have been multiplied by a factor 50 for visibility. Observed mode shapes are shown schematically near the corresponding resonance peaks. (b) Simulated and measured levitation height with different plate lengths (the thickness of all plates is 0.28mm). (c) Experimental and simulated resonance frequencies at different plate lengths. All dimensions and material parameters used for the simulations are found in the text and in Table 2.1, without free parameters.

tional mode around the z-axis is not observed, probably because it is not efficiently excited by the employed electrode configuration. Even if it were excited, it would not be efficiently detected by the LDV, that is only sensitive to motion in the z-direction. The frequency responses shown in Fig. 2.2a are determined at an off-centered point on the plate such that also the rotational modes 3 and 4 can be measured. Even though the amplitudes are small, it is surprising that modes 1 and 2 are detected using the vibrometer since their motion is in-plane, whereas the LDV is mainly sensitive to out-of-plane motion. It is likely that the in-plane motion of the plate is accompanied by an out-of-plane rotation or translation related to the shape of the magnetic potential well. We also note that both modes 1 and 2 as well as modes 3 and 4 are degenerate with almost identical resonance frequencies, and similar mode shapes (Fig. 2.2a).

To investigate the plate size, side length L, dependence of the observed effects and for

model verification, experiments are carried out on larger plates of 6.28, 8.14 and 10.25 mm. After placing the plates of different sizes above the magnet array, the levitation height of the plate is determined with a Keyence digital microscope (VHX-6000) using defocus method that measures depth based on the microscope's focus on the surface (Fig. 2.2b). Using the LDV then the resonance frequencies of modes 2, 4 and 5 of the plate are determined and are shown in Fig. 2.2c. A clear reduction in resonance frequency with increasing plate size is observed. We will analyze these observations in more detail using quantitative models.

In the static levitating state only the gravitation force and magnetic force act on the plate. A model for the magnetic field generated by the 4 cubic NdFeB magnets is constructed and used to determine the levitation height. The FEM and analytical modelling results for the magnetic field [21, 22], forces and levitation height, and its comparison to experiment can be found in the supplementary material A2. The total magnetic force from the field on the plate $\mathbf{F_B}$ is determined as:

$$\begin{aligned}\mathbf{F_B} &= \nabla \int_{\mathcal{V}} \mathbf{M}\cdot\mathbf{B}\mathrm{d}\mathcal{V} \\ &= \frac{\mu_0}{2}\int_{\mathcal{V}} \nabla(\chi_x H_x^2 + \chi_y H_y^2 + \chi_z H_z^2)\mathrm{d}\mathcal{V},\end{aligned} \tag{2.1}$$

where $\mathcal{V}$ is the volume of the plate, $H_{x,y,z}$ are the components of the magnetic field strength, $\mathbf{M}$ is the magnetization and $\mathbf{B}$ the magnetic flux density. In this analysis it is assumed that the plate does not significantly affect the magnetic field, since its relative magnetic permeability is close to 1. The results of the FEM simulations, that determine the height at which the z-component of $\mathbf{F_B}$ is equal and opposite to the gravitational force, are shown in Fig. 2.2b. The dependence of the levitation height on plate size L is well captured.

We also obtain the resonance frequencies of the plate numerically. The undriven free-body dynamics of translational modes 1,2 and 5 can be modelled by the differential equation $m\ddot{q} + c\dot{q} + kq = 0$, where q is the translational displacement and m, c and k are the mass, viscous damping coefficient and stiffness of that degree-of-freedom, respectively. Similarly for the rotational modes 3 and 4 the dynamics can be modelled by $I\ddot{\theta} + \Gamma\dot{\theta} + \mu\theta = 0$, where θ is the rotational angle around the x or y-axis and I, Γ and μ are the moment of inertia, rotational viscous damping coefficient and torsional stiffness of the mode, respectively.

Since the gravitational force is independent from position, the stiffness of the resonant modes is solely determined by the derivative of the magnetic force $\mathbf{F_B}$, or magnetic torque, with respect to translational or rotational motion around its equilibrium position. When the plate translates or rotates, the spatial volume $\mathcal{V}$ over which the integral in Eq. (2.1) is taken changes, and results in a restoring force or moment. For the torques, the integral in Eq. (2.1) is taken over the torque per volume element $\mathbf{r} \times \mathrm{d}\mathbf{F_B}$, where $\mathbf{r}$ is the position of the element with respect to the rotational axis. Using these integrals, the translational and torsional stiffnesses of the rigid body modes of the plate are numerically obtained.

From the FEM simulations the resonance frequencies are computed using $2\pi f_{res} = \sqrt{k/m}$ and $2\pi f_{res} = \sqrt{\mu/I}$ for the translational and rotational modes, respectively. The

FEM results are shown in Fig. 2.2c and show close agreement to the experimental results. The observed reduction in resonance frequency is less than what would be expected for a fixed stiffness system for which $f_{res} \propto L^{-1}$. This indicates that the stiffnesses of the system increase with plate size despite the higher levitation height, which can be attributed to the larger volume over which the integral in Eq. (2.1) is taken.

2.3.2. EDDY CURRENT DAMPING

For the rigid body modes of diamagnetically levitating resonators, many types of dissipation are negligible. In particular, mechanical friction, radiation loss, surface and material damping are all expected to be negligible or absent during rigid body vibrations. Air damping is still significant, and can be eliminated by performing experiments at low pressure. In Fig. 2.3a it is shown that the resonator's Q significantly increases and saturates at lower pressures. The saturation shows that at a pressure of 10^{-4} mbar, the damping of the rigid body modes is dominated by another mechanism, that is eddy current damping. To verify this, we compare the measured Qs on plates of different sizes in Fig. 2.3b. Included in the figure are also our FEM simulations of eddy current damping

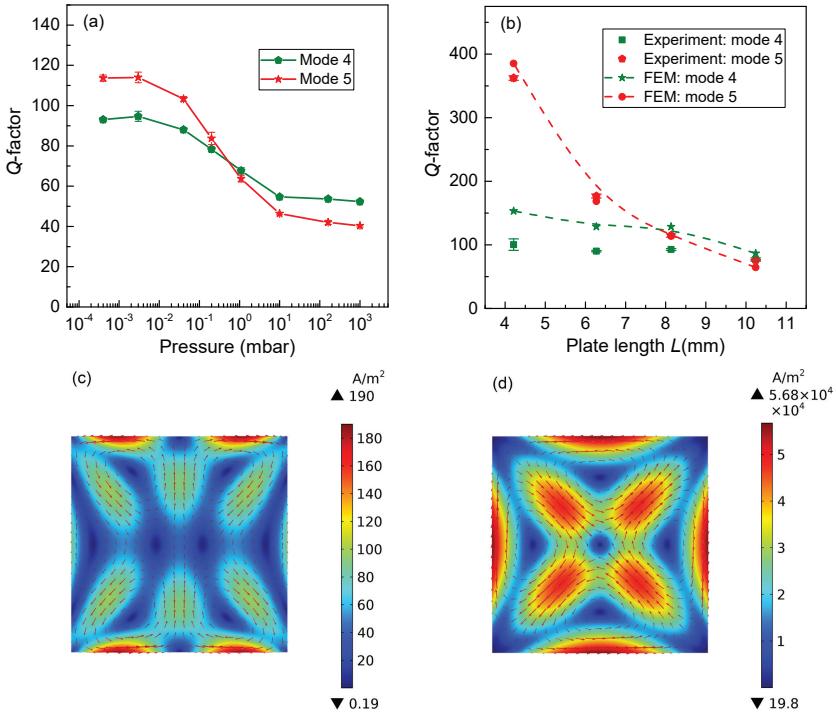

Figure 2.3: Damping of levitating resonators. (a) Pressure-dependent Q of a $8.03 \times 8.24 \times 0.28\,\mathrm{mm}^3$ levitating plate. (b) Experimental and simulated Qs of the levitating resonators of different plate lengths L (thickness t=0.28mm). All measurements have been performed at room temperature and low pressure (0.001 mbar). (c) and (d) Eddy current density simulations for modes 4 and 5, respectively. The colour map indicates the eddy current density and the arrows show the trajectory of the eddy currents.

To quantify the eddy current damping of the levitating resonator, we have developed a FEM model to evaluate the eddy current damping force. When a conductor moves with velocity vector $\mathbf{v}$ through a magnetic flux density field $\mathbf{B}$, the charge carriers inside the conductor feel an electric field $\mathbf{v}\times\mathbf{B}$ due to the Lorentz' force in addition to the field from the electric potential V_e, that generates an eddy current density $\mathbf{J}$ given by

$$\mathbf{J} = -\sigma\nabla V_e + \sigma(\mathbf{v}\times\mathbf{B}), \tag{2.2}$$

where σ is the electrical conductivity matrix, that has nonzero diagonal elements σ_x, σ_y, and σ_z. By combining Eq. (2.2) with the current continuity condition $\nabla\cdot\mathbf{J}=0$ and the boundary condition $\mathbf{J}\cdot\mathbf{n}=0$ ($\mathbf{n}$ is the unit vector perpendicular to the boundary), the eddy current density distribution $\mathbf{J}$ and potential V_e can be determined numerically for known $\mathbf{v}$, σ, $\mathbf{B}$ and plate dimensions. The simulated current density $\mathbf{J}$ distribution through the plate for the rotational mode 4 and translational mode 5 are shown in Figs. 2.3c,d respectively.

The total damping contribution due to eddy currents can now be evaluated for the translational modes by integrating the eddy current forces $\mathbf{J}\times\mathbf{B}$ to obtain $\mathbf{F}_{\text{eddy}}$ [23]. Similarly for the rotational modes the torques $\mathbf{r}\times(\mathbf{J}\times\mathbf{B})$ can be integrated to obtain the total torque τ_{eddy}. Since for thin plates and motion under consideration, the eddy currents run mainly in-plane and the motion is out-of-plane, it is the in-plane component of $\mathbf{B}$ that contributes mainly to the relevant out-of-plane force $\mathbf{F}_{\text{eddy}}\propto(\mathbf{v}\times\mathbf{B})\times\mathbf{B}$. Since the in-plane component of the $\mathbf{B}$ field is largest near the boundary between the magnets, it is expected that these regions contribute most to the $\mathbf{F}_{\text{eddy}}$.

As expected, the eddy current damping force $\mathbf{F}_{\text{eddy}}$ is found to be proportional and in the opposite direction of the velocity $\dot{q}$ and similarly the torque τ_{eddy} is opposite and proportional to the rotational velocity $\dot{\theta}$. From the proportionality constants the coefficients c and Γ for the translational and rotational modes can be determined. Using our FEM simulations, and material parameters given in table 2.1, we found the Qs associated with modes 4 and 5 for different plate lengths L as follows

$$\begin{aligned} Q &= \frac{2\pi m f_{\text{res}}}{c} \quad \text{(translational modes)},\\ Q &= \frac{2\pi I f_{\text{res}}}{\Gamma} \quad \text{(rotational modes)}. \end{aligned} \tag{2.3}$$

The simulated Q corresponds well to the experimental values as shown in Fig. 2.3b. This provides evidence that eddy current damping can account largely for the observed Qs, and their size dependence for the rigid body modes of diamagnetically levitating plates. A difference is observed between the simulated and measured Q of mode 4, which is attributed to the fact that the actual experimentally obtained rotation is observed to occur not exactly around the x or y-axis. Fig. 2.3b shows a steep increase in Q with decreasing plate length L for translational mode 5. A reduction of plate length L by a factor of 2 results in an increase of Q by a factor of ~4. For the rotational mode 4 such an increase in Q is not observed. The observed experimental trend suggests that very high Qs might be achieved in diamagnetically levitating plates of microscopic dimensions. To test this hypothesis we simulate the Q of the z-direction translational mode 5 for levitating graphite plate resonators with L=10^{-4}-10^{1} mm. Besides scaling the lateral

dimensions of the plate, also the dimension of the magnets $D = 1.2L$ and plate thickness $t = 0.03L$ are scaled proportionally. For each value of L, first the magnetic field and levitation height are calculated, then the resonance frequency, eddy currents and Q are determined according to the procedure outlined before. The result is plotted in Fig. 2.4. In Fig. 2.4a, we show that the resonance frequency is increasing with smaller plate size, and this can be attributed to the significant decrease in mass. In terms of the damping as can be seen in Fig. 2.4b, for a reduction of L by a factor 10^4 the Q increases by a factor 3.8×10^6. For plate sizes of the order of 1 μm, Qs above 100 million might be achievable, competitive to the Q of the best mechanical resonators currently available [16]. This suggests that levitating nano/micro particles could be interesting candidates for realizing high-Q resonators for accurate sensors and for studying quantum mechanics at room temperature [16, 24–26].

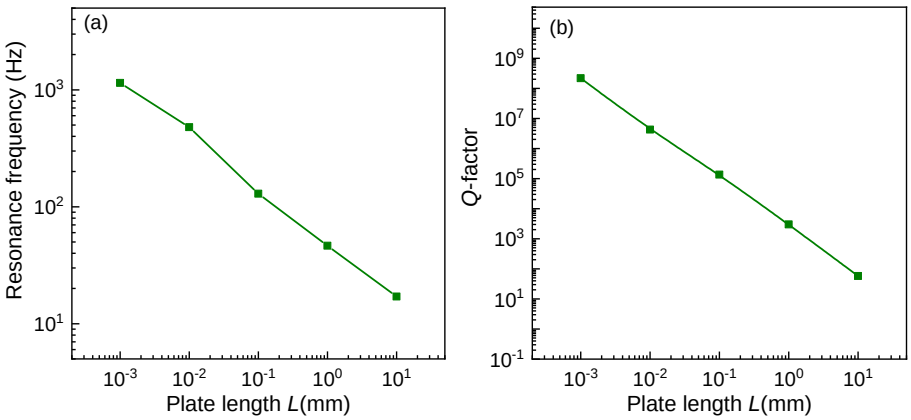

Figure 2.4: Frequency and damping dependency on size. Simulation of the frequency (a) and Q-factor (b) as a function of plate length L down to the microscale. In this simulation the plate thickness t and magnet size D is also scaled down ($D = 1.2L$ and $t = 0.03L$).

2.4. CONCLUSIONS

In conclusion, we experimentally study the rigid body motion of diamagnetically levitating resonators at different pressures. By levitating graphite plates above magnets we eliminate external mechanical effects, such that their dynamics is solely governed by magnetic field. The levitation height, resonance frequencies and Qs are measured as a function of plate size by laser Doppler vibrometry, and are modeled effectively using FEM simulations. In particular the Q of the out-of-plane translational mode is found to increase significantly with reducing dimensions. Using simulations evidence is provided that this increase in Q continues at smaller dimensions where Q factors above 100 million might be attainable, making levitating diamagnetic resonators an interesting candidate for high-Q, low-noise oscillators and sensors.

2.5. APPENDIX

A1: MOVIES OF THE RIGID BODY MODES OF A DIAMAGNETICALLY LEVITATING RESONATOR

As supporting information, movies of the rigid body motion of a levitating plate are included. The slow-motion movies are recorded at a frame rate of 240 fps and played back eight times slower. They are recorded on a $4.28 \times 4.14 \times 0.28$ mm pyrolytic graphite plate that levitates above 4 permanent cubic NdFeB magnets, with an edge length of 12 mm, and alternating out-of-plane magnetization. The plate is actuated by electrostatic force using two asymmetric electrodes (copper tapes) that are isolated from the magnets. A sinusoidal voltage signal (V_{AC}=1.0 V) at different specific frequency (10.23, 10.75, 19.41, 19.81 and 22.72 Hz) is superposed on an offset voltage (V_{DC}=-1.2 V) and amplified by a voltage amplifier (40×) that applies the voltage across the electrodes.

The movie can be found through the link below:
https://aip.scitation.org/doi/suppl/10.1063/5.0009604

A2: SIMULATION OF THE MAGNETIC LEVITATION HEIGHT

In order to determine the levitation height, we calculate the magnetic field both using an analytical derivation and using the Finite Element Method (FEM). The FEM simulations are performed using *COMSOL Multiphysics 5.3a.* For comparison with experiments we model the field distribution of 4 permanent magnets of $12\times12\times12$ mm^3 with a remanent magnetic flux density B_r=1.4 T and rounded edges with a fillet radius of 1 mm. The summed magnetic field $\mathbf{B}(x, y, z)$ of the magnets is determined analytically and using FEM. Then, assuming that the influence of the diamagnetic plate on the field is negligible, the integrated magnetic force on the diamagnetic plate, $\mathbf{F_B}$, can be determined using

$$\begin{aligned}\mathbf{F_B} &= \nabla \int_{\mathcal{V}} \mathbf{M}\cdot\mathbf{B}\,\mathrm{d}\mathcal{V} \\ &= \frac{\mu_0}{2}\int_{\mathcal{V}} \nabla(\chi_x H_x^2 + \chi_y H_y^2 + \chi_z H_z^2)\,\mathrm{d}\mathcal{V},\end{aligned} \tag{2.4}$$

where χ_x, χ_y, χ_z are the magnetic susceptibility of the levitating plate in x, y, z directions, $\mathcal{V}$ is the volume of the plate, and $\mathbf{M}$ is the plate's magnetization. The components of the magnetic field inside the plate are $H_{x,y,z} = B_{x,y,z}/\mu$, where the magnetic permeability $\mu \approx \mu_0$ for graphite.

The magnetic field is determined and in Fig. 2.5 we compare the volume integrated upward magnetic force $F_{B,z}$ calculated analytically for 4 cubes without fillets to the force obtained from FEM simulations as a function of levitation height h. The correspondence between analytical and FEM simulation verifies the accuracy of the FEM simulation. In the same figure the integrated downward gravitational force on the diamagnetic plate is shown. The plate levitates at the height h where the curves intersect. This agrees well with the measured levitation height (solid blue circle) of the plate with dimensions $10.23 \times 10.26 \times 0.28\,\mathrm{mm}^3$.

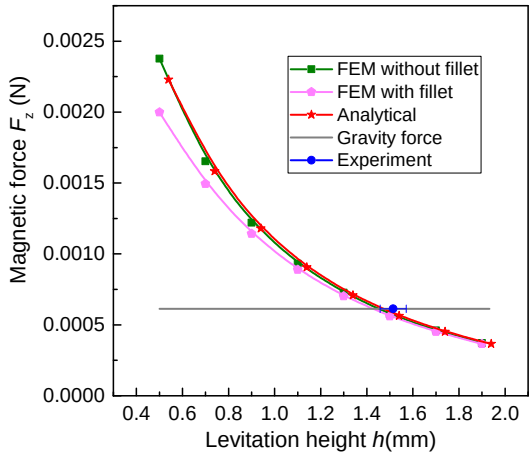

Figure 2.5: Magnetic force as a function of levitation height calculated by analytical and FEM modelling for a graphite plate of $10.23\times10.26\times0.28\,\mathrm{mm}^3$ above 4 laternating NdFeB magnets of $12\times12\times12\,\mathrm{mm}^3$. The levitation height h is defined as the distance from the top surface of the levitating plate to the top surface of magnets.

REFERENCES

[1] X. Chen, A. Keşkekler, F. Alijani, and P. G. Steeneken, "Rigid body dynamics of diamagnetically levitating graphite resonators", Applied Physics Letters **116**, 243505 (2020).

[2] E. Brandt, "Levitation in physics", Science **243**, 349–355 (1989).

[3] G. Kustler, "Diamagnetic levitation-historical milestones", Revue Roumaine Des Sciences Techniques Serie Electrotechnique Et Energetique **52**, 265 (2007).

[4] M. Simon and A. Geim, "Diamagnetic levitation: flying frogs and floating magnets", Journal of applied physics **87**, 6200–6204 (2000).

[5] I. Lyuksyutov, D. Naugle, and K. Rathnayaka, "On-chip manipulation of levitated femtodroplets", Applied physics letters **85**, 1817–1819 (2004).

[6] H. Chetouani, C. Jeandey, V. Haguet, H. Rostaing, C. Dieppedale, and G. Reyne, "Diamagnetic levitation with permanent magnets for contactless guiding and trapping of microdroplets and particles in air and liquids", IEEE Transactions on Magnetics **42**, 3557–3559 (2006).

[7] H. Chetouani, V. Haguet, C. Jeandey, C. Pigot, A. Walther, N. Dempsey, F. Chatelain, B. Delinchant, and G. Reyne, "Diamagnetic levitation of beads and cells above permanent magnets", in Transducers 2007-2007 international solid-state sensors, actuators and microsystems conference (IEEE, 2007), pp. 715–718.

[8] D. Garmire, H. Choo, R. Kant, S. Govindjee, C. Sequin, R. Muller, and J. Demmel, "Diamagnetically levitated mems accelerometers", in Transducers 2007-2007 international solid-state sensors, actuators and microsystems conference (IEEE, 2007), pp. 1203–1206.

[9]C. Pigot, B. Delinchant, G. Poulin, and G. Reyne, "Optimization of a 3d micro-accelerometer based on diamagnetic levitation", International Journal of Applied Electromagnetics and Mechanics **30**, 179–188 (2009).

[10]L. Liu and F. Yuan, "Nonlinear vibration energy harvester using diamagnetic levitation", Applied Physics Letters **98**, 203507 (2011).

[11]L. Liu and F. Yuan, "Diamagnetic levitation for nonlinear vibration energy harvesting: theoretical modeling and analysis", Journal of Sound and Vibration **332**, 455–464 (2013).

[12]S. Palagummi and F. Yuan, "A bi-stable horizontal diamagnetic levitation based low frequency vibration energy harvester", Sensors and Actuators A: Physical **279**, 743–752 (2018).

[13]S. Clara, H. Antlinger, A. Abdallah, E. Reichel, W. Hilber, and B. Jakoby, "An advanced viscosity and density sensor based on diamagnetically stabilized levitation", Sensors and Actuators A: Physical **248**, 46–53 (2016).

[14]M. Boukallel, J. Abadie, and E. Piat, "Levitated micro-nano force sensor using diamagnetic materials", in 2003 ieee international conference on robotics and automation (cat. no. 03ch37422), Vol. 3 (IEEE, 2003), pp. 3219–3224.

[15]S. Schmid, L. G. Villanueva, and M. L. Roukes, *Fundamentals of nanomechanical resonators*, Vol. 49 (Springer, 2016).

[16]R. A. Norte, J. P. Moura, and S. Gröblacher, "Mechanical resonators for quantum optomechanics experiments at room temperature", Physical review letters **116**, 147202 (2016).

[17]J. Van Beek, P. Steeneken, and B. Giesbers, "A 10mhz piezoresistive mems resonator with high q", in 2006 ieee international frequency control symposium and exposition (IEEE, 2006), pp. 475–480.

[18]J. Gieseler, L. Novotny, and R. Quidant, "Thermal nonlinearities in a nanomechanical oscillator", Nature physics **9**, 806–810 (2013).

[19]S. Palagummi and F. Yuan, "An optimal design of a mono-stable vertical diamagnetic levitation based electromagnetic vibration energy harvester", Journal of Sound and Vibration **342**, 330–345 (2015).

[20]J. Pappis and S. Blum, "Properties of pyrolytic graphite", Journal of the American Ceramic Society **44**, 592–597 (1961).

[21]E. P. Furlani, *Permanent magnet and electromechanical devices: materials, analysis, and applications* (Academic press, 2001).

[22]G. Akoun and J.-P. Yonnet, "3d analytical calculation of the forces exerted between two cuboidal magnets", IEEE Transactions on magnetics **20**, 1962–1964 (1984).

[23]B. Ebrahimi, M. B. Khamesee, and M. F. Golnaraghi, "Design and modeling of a magnetic shock absorber based on eddy current damping effect", Journal of Sound and Vibration **315**, 875–889 (2008).

[24]J.-F. Hsu, P. Ji, C. W. Lewandowski, and B. D'Urso, "Cooling the motion of diamond nanocrystals in a magneto-gravitational trap in high vacuum", Scientific reports **6**, 30125 (2016).

[25]M. O'Brien, S. Dunn, J. Downes, and J. Twamley, "Magneto-mechanical trapping of micro-diamonds at low pressures", Applied Physics Letters **114**, 053103 (2019).

[26]C. W. Lewandowski, T. D. Knowles, Z. B. Etienne, and B. D'Urso, "High sensitivity accelerometry with a feedback-cooled magnetically levitated microsphere", arXiv preprint arXiv:2002.07585 (2020).

3

DIAMAGNETIC COMPOSITES FOR HIGH-Q LEVITATING RESONATORS

Levitation offers extreme isolation of mechanical systems from their environment, while enabling unconstrained high-precision translation and rotation of objects. Diamagnetic levitation is one of the most attractive levitation schemes, because it allows stable levitation at room temperature without the need for a continuous power supply. However, dissipation by eddy currents in conventional diamagnetic materials significantly limits the application potential of diamagnetically levitating systems. Here, we present a route towards high Q macroscopic levitating resonators by substantially reducing eddy current damping using graphite particle based diamagnetic composites. We demonstrate resonators that feature quality factors Q above 450,000 and vibration lifetimes beyond one hour, while levitating above permanent magnets in high vacuum at room temperature. The composite resonators have a Q that is more than 400 times higher than that of diamagnetic graphite plates. By tuning the composite particle size and density, we investigate the dissipation reduction mechanism and enhance the Q of the levitating resonators. Since their estimated acceleration noise is as low as some of the best superconducting levitating accelerometers at cryogenic temperatures, the high Q and large mass of the presented composite resonators positions them as one of the most promising technologies for next generation ultra-sensitive room temperature accelerometers.

3.1. INTRODUCTION

The low dissipation and high quality factor (Q) of mechanical resonators makes them the devices of choice in precision time-keeping, frequency filtering, and sensing applications. With the emergence of nano- and micro-electromechanical systems, and the drive towards quantum limited mechanical elements, pushing the performance boundaries of resonators has become a matter of high scientific and societal relevance [1–6]. In particular, mechanical energy loss via the clamping points has become a dominant factor, limiting the Q of these resonators. As a consequence, attention has moved towards the field of levitodynamics [7, 8]. By employing levitating resonators that are well isolated from their environment, losses can be minimised and extreme sensitivities can be achieved.

Optically, superconducting, and electrically levitating micro and nanoresonators have been shown to feature high Qs in the range $10^6 - 10^7$ [9–12]. Although these techniques are of great interest for fundamental studies, the requirement for continuous position control and cooling power supply [8], narrows their application range, since the levitating object will collapse in a situation of power loss. Diamagnetic levitation is the only known method for realizing stable continuous vacuum levitation of objects at room temperature without external power supply [13–16]. Moreover, unlike optical and electrical levitation that are limited to nano-gram objects [17, 18], diamagnetic levitation is the method of choice for levitating macroscopic objects whose larger mass can significantly enhance the sensitivity of sensors like accelerometers [19] and gravimeters [20–23]. However, the Q of conventional diamagnetic materials such as graphite that has high magnetic susceptibilities is significantly limited by eddy current damping forces [15]. While the diamagnetic levitation of non-conductive materials such as silica could make the levitodynamic system immune to the presence of eddy current damping forces, their magnetic susceptibility is lower, such that it normally only is suitable for levitating microscopic objects [24, 25].

Here, we demonstrate millimeter scale composite plates comprising graphite microparticles dispersed in epoxy resin that levitate stably above permanent magnets and exhibit Qs above 450,000. The strong diamagnetic susceptibility of the graphite particles allows passive levitation of the composite plates, while the epoxy acts as an insulating material that suppresses eddy currents. To investigate the dependence of Q on composite properties, we perform simulations and experiments on composites with different particle sizes and volume fractions. We confirm that by reducing particle size, damping can be significantly decreased while maintaining the macroscopic size of the levitating object. Finally, we compare the performance of the realized diamagnetic composite resonator to state-of-the-art accelerometers and show that it leads to one of the lowest acceleration noise figures achieved thus far in levitating sensors.

3.2. RESULTS

3.2.1. DIAMAGNETICALLY LEVITATING COMPOSITES

To realize diamagnetically levitating resonators with high Qs, we fabricate composite materials with distributed graphite microparticles by dispersing them in epoxy resin through mechanical mixing, and then curing the resin in an oven (see Methods and A1). The fabrication process enables a high degree of freedom in size of graphite particles and selection of resin composition. Due to the strong diamagnetic susceptibility of graphite, the composite levitates stably above permanent $Nd_2Fe_{14}B$ magnets arranged in a checkerboard configuration with alternating magnetization (see Fig. 3.1a). We expect that the epoxy between the microparticles acts as an insulator, confining eddy currents within the particles (Fig. 3.1b), and thus diminishing eddy current damping forces and increasing Q [15]. Furthermore, since for a composite with particle size d moving in a magnetic field, the eddy current damping force per volume scales quadratically with particle size ($F_e \propto d^2$ see Fig. 3.1c and A5 [26]), we expect that by reducing the microparticle size in the composite, high mechanical Qs can be achieved while maintaining macroscopic mass. To experimentally investigate this effect, square graphite/epoxy composite plates of different size with a constant 90 μm thickness are prepared, as shown in Fig. 3.1d. The successful levitation of the composite plates with graphite volume fraction V_f of 21 %, as shown in Fig. 3.1d, confirms that the diamagnetism of graphite is maintained in the microparticles and that the diamagnetic force remains strong enough to oppose the gravitational force, even though the graphite particles have anisotropic mag-

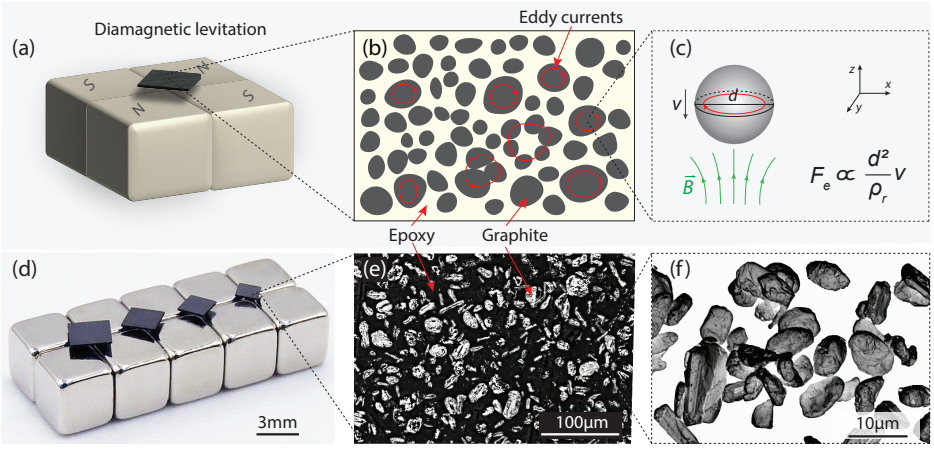

Figure 3.1: (a) Schematic of a diamagnetic plate levitating above 4 cubic $Nd_2Fe_{14}B$ magnets with alternating magnetization. (b) Schematic of the eddy currents (red circular arrows) generated inside the graphite microparticles that are distributed in the composite. (c) The relationship between the eddy current damping force F_e and particle size d, for a spherical particle with electrical resistivity ρ_r moving in a magnetic field (see A5 for details). (d) An array of graphite-epoxy composite plates of different sizes levitating above magnets at room temperature and pressure. (e) Confocal microscopy image of the surface of the composite plate with particle size of 17.6 um and volume fraction of 0.21, showing the distribution of the graphite particles (white) in the epoxy (black). (f) Scanning electron microscopy image showing the size and morphology of the graphite particles.

netic susceptibilities and are randomly oriented inside the epoxy matrix. In Fig. 3.1e,f we show microscopic images of the composite and graphite microparticles from which we note that the particle sizes are distributed over a wide range (see the particle size measurement in A2.1). Moreover, we quantitatively analyze the particle distribution (see A2.2) and observe that the graphite particles are randomly distributed inside the epoxy matrix.

3.2.2. Q-FACTOR MEASUREMENT

To probe the vibrations of the levitating plates, we use a Polytec MSA400 Laser Doppler Vibrometer (LDV) and measure their out-of-plane velocity in a vacuum chamber at a pressure of 0.1 mbar (see Fig. 3.2a and the Methods). We characterize the spectral response of the levitating objects by driving them electrostatically at different frequencies. Fig. 3.2b shows the area-averaged magnitude of the spectral response for a $1.8 \times 1.8 \times 0.09\,\mathrm{mm}^3$ composite plate with 8.6 μm graphite particles. Three plate resonance peaks can be identified in the spectral response, which correspond to the two rotational modes at 29.7 Hz (Mode 1) and 31.4 Hz (Mode 2) and the translational rigid body mode of vibration at 34.0 Hz (Mode 3). In this work, we focus on the Q of the out-of-plane translational mode that relates to the vertical motion (Mode 3). The mode shapes are identified by scanning the laser over the plate surface at the corresponding resonance frequencies, and are shown in Fig. 3.2b.

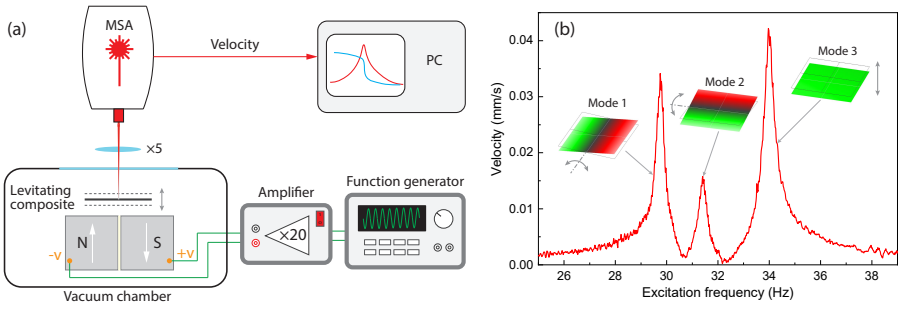

Figure 3.2: Experimental setup and rigid body dynamic response of a levitating composite resonator. (a) Schematic of the measurement setup comprising a MSA400 Polytec Laser Doppler Vibrometer (LDV) for the readout and electrostatic force as the actuation means. The drive voltage is generated by the function generator and is amplified by a 20× voltage amplifier that drives the levitating plate into resonance. The electrostatic force is generated by applying voltage between the magnets beneath the levitating plate. By focusing the vibrometer's laser beam on the plate, the plate motion is captured, and the acquired velocity is used for spectral analysis. To isolate environment noise, we place the LDV and vacuum chamber on an optical table. (b) The frequency response curve of a $1.8 \times 1.8 \times 0.09\,\mathrm{mm}^3$ levitating composite plate with 8.6 μm graphite particles measured at 0.1 mbar. Three of the measured mode shapes using LDV are shown close to the corresponding resonance peaks.

Since eddy current and air damping [15] are the major sources of dissipation in diamagnetically levitating objects, we minimize the effect of air damping by operating the composite plate resonator in high vacuum (10^{-6}mbar). In Fig. 3.3a, we compare the resonant response of the plate's translational mode in low (0.1mbar) and high (10^{-6}mbar) vacuum environments. We find an increase in the resonance frequency which we at-

tribute to a reduction in mass loading by the surrounding gas. Moreover, the high vacuum results in a much sharper peak, with much higher Q, due to the reduction of air damping effects. In fact, the Q is so high that it is difficult to accurately determine it using a frequency response measurement, due to the limited resolution bandwidth of the measurement setup.

To determine the Q more accurately while also minimizing the influence of spectral broadening, we perform ringdown measurements. These are conducted by first electrostatically exciting the composite plate at its resonance frequency, then switching off the excitation voltage and recording the free vibration decay. The amplitude of the underdamped vibration decays proportional to $\propto e^{-\frac{t}{\tau}}$, where $\tau = \frac{Q}{\pi f_{\text{res}}}$ is the decay constant and f_{res} is the resonance frequency of the plate. In Fig. 3.3b we show a typical measurement for the translational mode of the levitating composite. Note that a very long vibration lifetime of $\sim 4{,}000$s is observed, corresponding to a Q of 8.2×10^4. In the inset of Fig. 3.3b we also show the free vibrations of the plate over a 0.5 s time interval, demonstrating a clear sinusoidal response during the energy decay measurements. It is noted

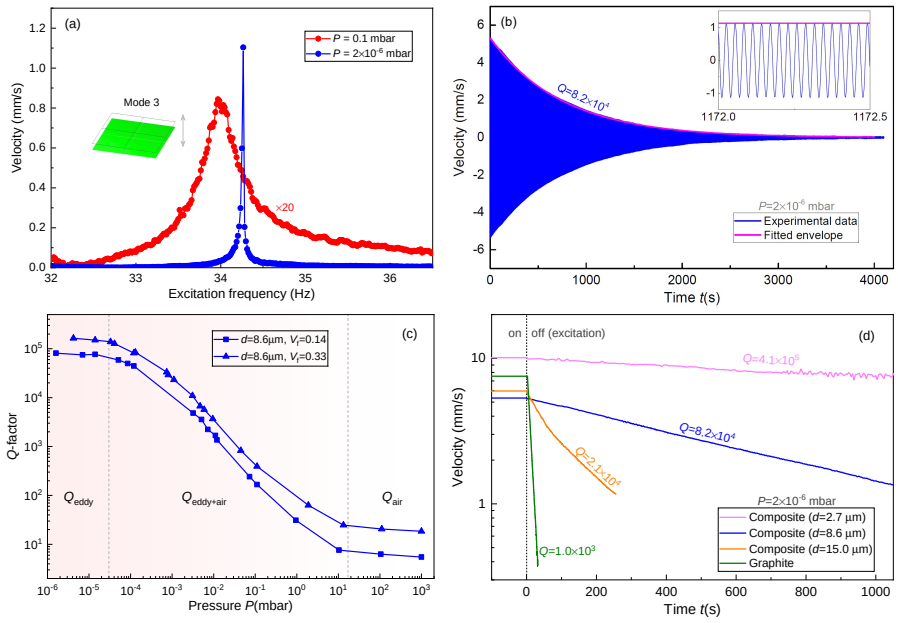

Figure 3.3: Energy dissipation measurements. (a) Frequency response curves for the translational mode of the $1.8 \times 1.8 \times 0.09\,\text{mm}^3$ levitating composite plate measured at 0.1 mbar and 2×10^{-6}mbar. The frequency response curve at 0.1 mbar has been multiplied by a factor of 20 for visibility. (b) Undriven ringdown of the same composite plate for a duration of 4.000 s at 2×10^{-6}mbar and its fitted envelope. The time signal for a 0.5 s interval is also shown in the inset. (c) The Q as a function of pressure for two sizes of composite plate shows three characteristic regions comprising the region where air damping is dominant (right), region where both air and eddy current damping contribute to dissipation (middle), and region where eddy current damping is dominant (left). (d) Ringdowns of a levitating graphite plate and three composite plates composed of different particle size, revealing that decreasing the particle size results in higher Q of the samples. The dashed line separates the time span between the excitation is on and off.

that due to the presence of low-frequency perturbations from the vacuum pump and the environment, the amplitude of the high-Q composites might fluctuate during the ring-down measurements as shown in Fig. 3.3d. However, the fluctuations do not influence the Q factor measurements as they are very small compared to the vibration amplitude.

To ensure that the energy decay constant τ is not limited by air damping, we sweep the pressure from $10^{-6} - 10^{3}$ mbar and measured Q as a function of air pressure (see Fig. 3.3c). The data for two composite plates with $d = 8.6\,\mu$m particle size and different graphite volume fractions show three distinct regions in the Q versus pressure plot. When the pressure is reduced below 3×10^{-5} mbar, Q reaches a plateau, as shown in Fig. 3.3c. This suggests that air damping has become negligible, and Q is solely limited by eddy currents. The Qs shown in the rest of this work are measured at a pressure below 5×10^{-6} mbar to eliminate the effect of air damping in our measurements.

3.2.3. TAILORING COMPOSITE PROPERTIES TO SUPPRESS EDDY CURRENTS

To investigate the effect of the graphite particle size and volume fraction on the levitation forces and the eddy current damping, we fabricate square plates with different graphite volume fractions V_f, side length L and particle size d. In Fig. 3.3d we compare the ring-down response of three $1.8 \times 1.8 \times 0.09\,\text{mm}^3$ graphite composite plates with different particle sizes, namely $d = 15.0, 8.6$ and $2.7\,\mu$m. We find that the plate that encompasses the smallest particle size exhibits the largest value of Q. Remarkably, we observe an increase of nearly 410 times in Q for the $2.7\,\mu$m particle composite plates compared to the levitating graphite plate.

To better understand this observation and gain deeper insight into the mechanisms accountable for Q enhancement, simulations based on Finite Element Method (FEM) are performed to calculate the levitation height and eddy current damping force using COMSOL multiphysics. These simulations are carried out assuming that the graphite particles have a spherical shape and are distributed inside the matrix (see A3 for details of the numerical modelling and parameter values used in our simulations). In our simulations, we treat the epoxy as air since its magnetic susceptibility and electrical conductivity are negligible compared to graphite. We also note that graphite is inherently anisotropic [13]. However, in our fabrication procedure graphite particles are randomly oriented in the epoxy matrix, and thus by considering all possible orientations in the matrix, the local anisotropy can be averaged out and the effective macroscopic behavior can be viewed isotropic. For this reason, in our study we treat the magnetic susceptibility of graphite as an effective value χ_{eff} which we evaluate by fitting our FEM simulations to the measured levitation height of the composite from experiments (see Fig. 3.13 for more details).

In Fig. 3.4a we show the levitation height of the composite plates with particle size $d = 17.6\,\mu$m as a function of volume fraction V_f. We find that composites with a graphite volume fraction below 14% ($V_f < 0.14$) do not provide sufficient diamagnetic force to counteract gravity and thus do not levitate. For composites with a graphite volume fraction above 43% ($V_f > 0.43$), the samples can not be produced with sufficient structural integrity due to the high particle content. Between these two limits, we observe a steady increase in the levitation height which agrees well with the simulations. These results indicate that the increase of the magnetic force is dominant over the increase in the overall

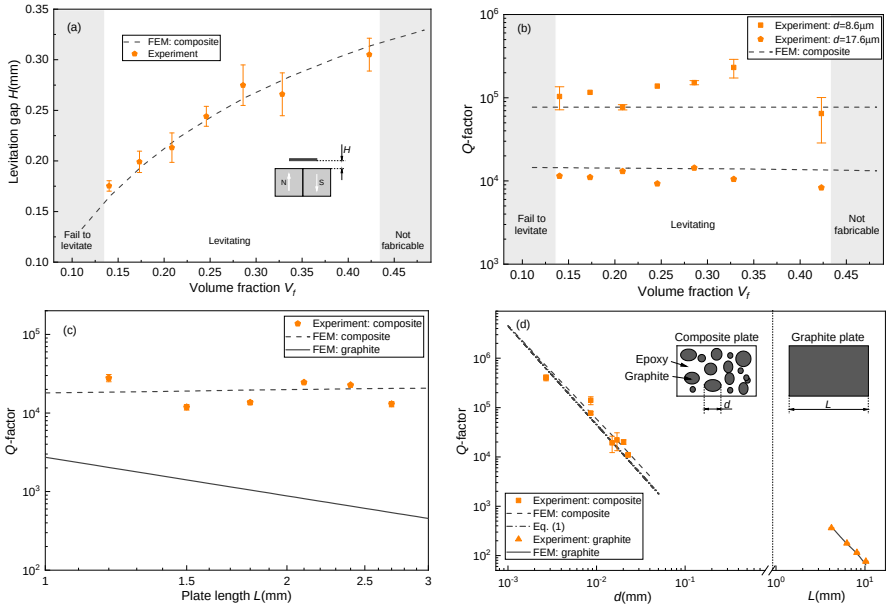

Figure 3.4: Dependence of the levitation force and dissipation on composite particle and plate size. (a) Levitation gap H of the $1.8\times1.8\times0.09\,\mathrm{mm}^3$ plate with 17.6 μm particles as a function of volume fraction. (b) Q-factor of two $1.8\times1.8\times0.09\,\mathrm{mm}^3$ plates with different particle size as a function of volume fraction. The gray area in Fig. 3.4a-b represents the volume fraction of which the composites can not be levitated. (c) Q-factor of square composite plates with a thickness of 90 μm as a function of plate side length L. The composite plates are made from d=17.6 μm particles with 0.21 volume fraction. (d) Dependence of Q on particle size. The left side of the graph (before the short dashed line) shows the Q of composite plates with varying graphite particle size. Since the Q is only weakly dependent on the volume fraction and side length (see Fig. 3.4b-c), the error bars in the data on the left side of Fig. 3.4d are obtained by analyzing the Qs obtained from plates with a thickness of 90 μm but different side lengths (1.2-2.7 mm) and volume fraction (0.14-0.32) at fixed d. The right side of the graph (after the short dashed line) shows the experimental Q of levitating plates made of pyrolytic graphite with 0.28 mm thickness and different side lengths L on the x-axis. The insets show schematics of the composite and graphite plate. In Fig. 3.4, the dashed and solid lines correspond to the FEM simulations for composite and graphite plates as described in A3, respectively. Moreover, the dashed-dotted line in Fig. 3.4d represents the Qs obtained from Eq. (3.1). The dots represent experimental data.

gravitational force through the higher mass density of the graphite particles compared to the epoxy, see Table 3.2 in A3.

We also study the influence of volume fraction V_f on the measured Q for composite plates with particle sizes d = 8.6 μm and d = 17.6 μm, as shown in Fig. 3.4b. It is interesting to see that unlike levitation height, Q does not significantly change with V_f, even though the measured bulk conductivity reveals an increase in the conductivity with the increase of V_f (see A4). This result suggests that the variations in bulk conductivity do not contribute considerably to the observed dissipation. A similar effect is seen in Fig. 3.4c, where we show the experimentally obtained Q of square plates with different side lengths L, that are cut out of the same composite with d = 17.6 μm and V_f = 0.21. It is observed from the figure that a reduction in side length does not substantially increase Q. This observation contrasts with Qs estimated from COMSOL simulations for pyrolytic

graphite plates, that increase close to an order of magnitude with reducing L[15].

The volume fraction and plate size independent Qs obtained from both experiments and simulations in Fig. 3.4b-c indicate that the majority of eddy current damping occurs inside the graphite particles and is not caused by currents flowing in between them. Thus, increasing the particle density increases the stored kinetic energy E_k (proportional to the mass) by approximately the same factor as the eddy current dissipation E_d (proportional to number of particles) (see Fig. 3.14 in A3.2), such that the Q, which is proportional to their ratio E_k/E_d, remains nominally constant.

After having investigated the effect of volume fraction and composite plate size, we now investigate the effect of graphite particle size d on Q. It can be observed from both the experimental and numerical results (see left side of Fig. 3.4d) that reducing the particle size d results in a clear increase in the Q of the composite plates. The Q increases from about 10,000 at d=22.7 μm, to a value as high as 460,000 at d = 2.7 μm, which is to our knowledge a record value for passively levitating diamagnetic resonators at room temperature. On the right side of Fig. 3.4d the Qs of pyrolytic graphite plates with varying side lengths are shown. These plates also show an increasing Q with decreasing plate size[15].

3.3. DISCUSSION AND CONCLUSIONS

To understand these findings, and in particular the increase in Q as a function of d, we use Faraday's law and obtain an analytic expression for the Q of a graphite/epoxy composite plate that moves in a magnetic field (see A5 for the detailed derivation):

$$Q = \frac{80\pi f_{res}\rho_r((\rho_g - \rho_e) + \rho_e/V_f)}{(C_r d)^2 B_2}, \tag{3.1}$$

where ρ_r is the resistivity, ρ_g is the density of graphite, ρ_e is the density of epoxy, and C_r is the effective particle size factor which we use to account for experimental deviations from the theoretical model due to variations in particle size, composition, morphology and distribution. Moreover, B_2 represents:

$$B_2 = \frac{\int_{V_{plate}} \left(\frac{dB}{dz}\right)^2 dV_{plate}}{V_{plate}}. \tag{3.2}$$

To compare our experimental findings in Fig. 3.4d to the analytical expression Eq. (3.1), we take $f_{res} = 35\,\text{Hz}$, $\rho_r = 5\times10^{-6}\,\Omega\cdot\text{m}$, $\rho_g = 2260\,\text{kg/m}^3$, $\rho_e = 1100\,\text{kg/m}^3$, and use COMSOL simulations to calculate $B_2 = 1.1\times10^6\,(\text{T/m})^2$ for a $1.8\times1.8\times0.09\,\text{mm}^3$ plate that levitates 0.26 mm above the magnets, corresponding to a composite with $V_f = 0.32$ (see Fig. 3.4a). Using these values and $C_r = 6.3$ as a fit parameter, we can match the experimental data shown in Fig. 3.4d with good accuracy. These results show that the Q in our levitating composites is inversely proportional to d^2, providing evidence that the strong dependence of Q on particle size can be mainly accounted for using Eq. (3.1), which is based on dissipation due to eddy currents that flow inside the graphite particles. The high sensitivity of Q to d, allows us to engineer and increase the Q of our levitating resonators by using different particle size while keeping the macroscopic dimensions of the

plate constant. The highest Q we obtain with this fabrication process is 4.6×10^5 for a $2.7 \times 2.7 \times 0.09\,\mathrm{m}^3$ composite plate with $d = 2.7\,\mu$m particles and $V_\mathrm{f} = 0.21$ volume fraction, which is two orders of magnitude higher than a pyrolytic graphite plate of the same size as shown in Fig. 3.4d.

It is of interest to note that extrapolation of the graphite plate data in the right side of Fig. 3.4d to smaller values of d leads to much higher values of Q than that are obtained experimentally with the composites in the left part of Fig. 3.4d. Several mechanisms might account for this difference, including the random orientation of the graphite particles in the composite, the particle size and shape variations, inactive layers on the particle surfaces and material parameter differences between the graphite in the plates and particles. In Fig. 3.4d the combined effect of these mechanisms are captured by the effective particle size factor C_r. Although we can not fully account quantitatively for the relatively large value of $C_\mathrm{r} = 6.3$ of this factor, possibly a small fraction of larger particles or clusters of particles in the composite accounts for a large part of the damping force. Microscopic images of the composites in A2 support this hypothesis, by showing that the dispersion of the particles is random and less homogeneous inside the epoxy matrix with local particle clusters. It might also be that not all sources of damping are included in Eq. (3.1) and more sophisticated models will need to be developed. Nevertheless, we foresee that by further control of the particle size and optimization of its distribution, levitating composites can achieve Qs above 1 million for millimeter composites with 1 μm or smaller particles.

The combination of high Q and large mass of the levitating composites promises low noise floor levels in accelerometry. In Fig. 3.5 we benchmark the presented levitating composite plates against state-of-the-art levitodynamic systems by plotting mass against Q (Fig. 3.5a) and the square root of the acceleration noise power spectral density $S_{aa} \propto f_\mathrm{res}/(mQ)$ [19] (Fig. 3.5b), which is a measure of the limit of detection of an accelerometer. The plots compare a range of superconducting, diamagnetically, electrically, and optically levitating systems, at room temperature (labeled with RT in Fig. 3.5), at cryogenic temperature (CT) or using feedback cooling (RT-FC). Note that RT-FC stands for natural Qs that are estimated from feedback cooling measurements. The plots also show the theoretical estimates of Q and $\sqrt{S_{aa}}$ (dashed lines) as a function of mass for diamagnetically levitating pyrolytic graphite. It appears from this benchmark that in terms of acceleration noise floor and Q, diamagnetic composites stand out, providing the possibility to levitate large, high-Q objects using relatively weak fields from permanent magnets. The combination of large levitating proof mass and high Q make these composites attractive materials for realizing next generation room temperature accelerometers with theoretical sensitivities as low as $0.16\,\mathrm{ng}/\sqrt{\mathrm{Hz}}$, that are comparable to superconducting levitodynamic systems at cryogenic temperatures (Fig. 3.5b).

In conclusion, we demonstrate diamagnetic high Q composite plate resonators consisting of graphite particles dispersed in an epoxy matrix that can be levitated at room temperature above permanent magnets with graphite volume fractions as low as 14%. By insulating the graphite particles, eddy currents are reduced and confined within the particles, allowing us to suppress the associated damping forces. This enables a remarkable enhancement in Q, reaching values as high as nearly 0.5 million at room temperature. Measurements of the dependence of damping to particle volume fraction, plate length,

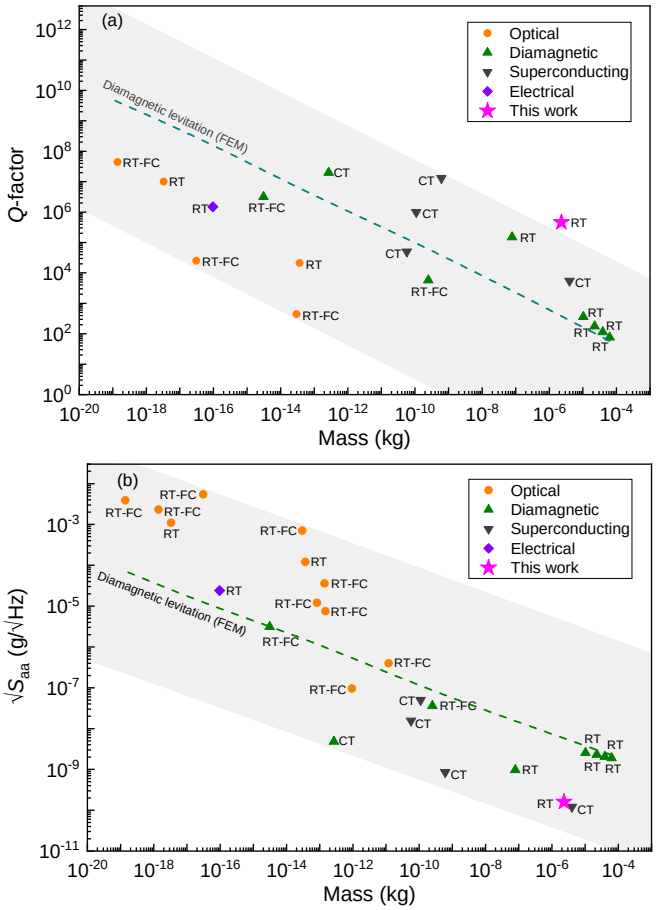

Figure 3.5: (a) Q-factor versus mass of different levitating systems (optical [9, 10, 27–29], diamagnetic [15, 24, 25, 30, 31], superconducting [11, 19, 32, 33] and electrical [12]). (b) Plot of acceleration noise floor against mass of different levitating accelerometers (optical [9, 10, 17, 27–29, 34–38], diamagnetic [15, 24, 25, 30, 31], superconducting [11, 19, 32, 33] and electrical [12]). RT stands for Qs measured at room temperature without feedback cooling, CT stands for Qs measured at cryogenic temperature without feedback cooling, RT-FC stands for natural Qs estimated from feedback cooling measurements. The Q and $\sqrt{S_{aa}}$ of different levitating systems are also shown in Table 3.3-3.5 of A6. The Q and $\sqrt{S_{aa}}$ shown as dashed lines are simulated using COMSOL for graphite plates with different size L (detailed material parameter values used for these simulations can be found in Table 3.3 of A3). In the simulations the plate thickness t and magnet size D are taken proportional to the plate side length ($D = 1.2L$ and $t = 0.03L$). The grey area in Fig. 3.5a-b sets the boundary of the Q and acceleration noise floor against mass of available levitodynamic systems in the literature.

and particle size are compared to FEM models, and show good agreement with an analytical model for eddy current damping forces that predicts Q to be inversely proportional to the squared particle size $Q \propto 1/d^2$. Reduction of the particle size and optimization of particle distribution and orientation, can lead to novel composites that further enhance the performance of future macroscopic levitating devices used as accelerom-

eters[19], gravimeters[20–23], or sensors for exploring macroscopic limits of quantum mechanics [5, 39–41].

3.4. METHODS

3.4.1. COMPOSITE FABRICATION

Graphite micro powders (purity >99.9%) with mean sizes from $2.7 - 22.7\,\mu$m are purchased from Nanografi Nano Technology. Particle size distribution measurements are performed using Malvern Mastersizer 3000 on 0.1% weight/volume aqueous solution of the powders using sodium dodecyl sulfate solution as surfactant. The particle size d of each type of powder is represented by the mean value of the distribution. The morphology of these powders is confirmed via Scanning Electron Microscopy (JEOL JSM-7500F).

The details of the graphite composite fabrication process are shown in Fig. 3.6. First, the two components of the epoxy (Epotek 302-3M from Gentec Benelux) are mixed at 3500 rpm for 5 minutes in a Dual Asymmetric Centrifuge mixer (DAC 150.1 FVZ-K) followed by the addition and mixing of the graphite powder at 500 rpm for 5 minutes. To reduce the viscosity of the resulting graphite-epoxy paste, ethanol is added, and further mixed at 500 rpm for 5 mins. This maximises dispersion and homogeneity of the paste with the graphite particles in the epoxy-ethanol matrix. The paste is then transferred into circular holes ($\phi = 10\,$mm) in a thin plastic mould with thickness of 0.12 mm on the top of a flat steel mould. The deposited paste is left at room temperature and pressure for 30 minutes to let the ethanol fully evaporate before curing the epoxy in order to minimise porosity. The graphite/epoxy paste is then compressed by steel moulds and cured in an oven at 100 °C for around 12 hours. After curing, an Optec micro laser cutter is used to cut the composite into square plates with desired lengths. Finally, fine sand paper (5 μm grain) is used to polish composite surface to the desired thickness.

3.4.2. MEASUREMENT

In our experiments, the excitation voltage is generated by the Polytec MSA400 vibrometer for the resonance frequency measurements, and by a function generator for the ringdown response measurements. The electrostatic force is generated as shown in Fig. 3.2a, by applying a voltage difference between the magnets beneath the levitating plate. To isolate the magnets from one another we use Kapton tape. When a voltage is applied between the two electrodes, the levitating plate acts as a floating electrode between the two electrodes, thereby forming a capacitive divider. In the area at which the plate overlaps with the electrodes, an electrostatic downward force is exerted that depends on the overlap area, voltage difference, and gap size. Since the electrostatic force is proportional to the square of the voltage, a DC offset voltage is added to make sure the electrostatic force has a component of the same frequency as the output voltage. Finally, to read out the motion, a Polytec LDV is used. The LDV measurements are conducted in a vacuum chamber over a pressure range of $10^{-6} - 1000\,$mbar at room temperature.

3.5. APPENDIX

In A1, we show the details of graphite composite fabrication process. A2 details out particle size measurement (A2.1) and particle dispersion analysis (A2.2). A3 presents the

FEM methodology used to calculate the eddy current damping in a graphite (A3.1) and a composite plate (A3.2). A4 shows the electrical conductivity measurements of composites with different volume fractions. In A5, we present the analytical model to calculate the eddy current damping of a composite plate moving in a magnetic field. Finally, in A6 we show the Qs and acceleration noise floor of state-of-the-art levitodynamic systems.

A1: COMPOSITE FABRICATION PROCESS

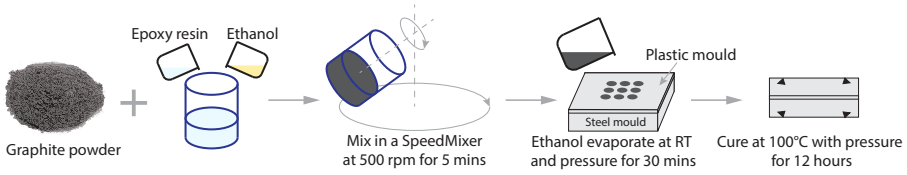

Figure 3.6: The schematic of composite fabrication process.

The details of graphite composite fabrication process is shown in Fig. 3.6.

A2: PARTICLE SIZE MEASUREMENT AND PARTICLE DISPERSION ANALYSIS

A2.1: PARTICLE SIZE MEASUREMENT

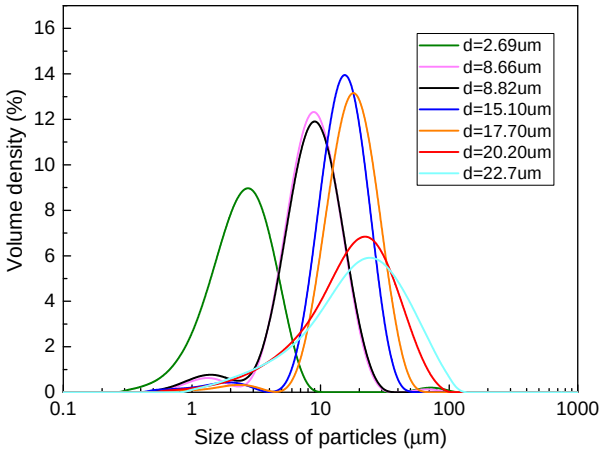

Figure 3.7: Particle size distribution for different particles used in the experiments.

Fig. 3.7 shows the size distribution of the graphite powders used in our experiments. The particle size distribution measurements are performed using Malvern Mastersizer 3000 on 0.1% weight/volume aqueous solution of the powders using sodium dodecyl sulfate solution as surfactant. The measurement of each type of powders is repeated five

times. From this figure, it can be seen that the particle size of each type of powder has a wide range of distribution. In the main text, we use the mean value of the distribution to represent the particle size d.

A2.2:PARTICLE DISPERSION ANALYSIS

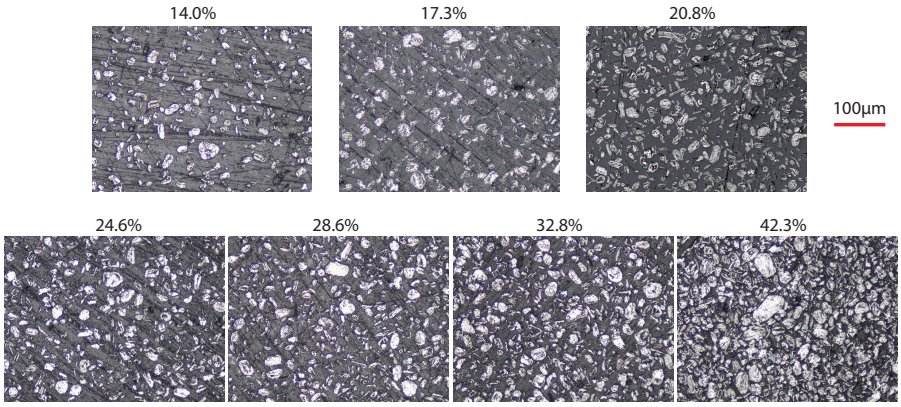

Figure 3.8: Microscopic images of composites with 17.6 μm particles and different volume fractions.

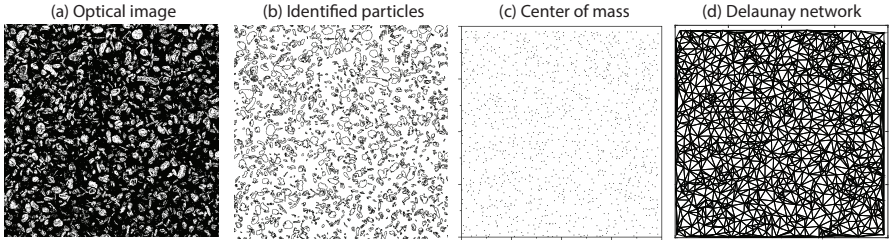

Figure 3.9: Particle dispersion analysis on a composite with 17.6 μm particles and 20.8 % volume fraction. To obtain the Area Disorder AD, we first take an image of the composite (a) and then identify the particles (b) using ImageJ. Afterwards, the particles' center of mass (c) is located, from which we build their Delaunay network (d) to calculate the AD.

Fig. 3.8 shows microscopic images of composites with 17.6 μm particles and different volume fractions. To obtain these images, samples are first polished with a fine sand paper to obtain a clear interface between the graphite particles and epoxy. The graphite particles are appearing in white color due to the reflection of light from the microscope. To quantify the dispersion quality of the particles inside epoxy, we use the Area Disorder (AD) of the Delaunay network as described in reference [42]. AD is a dimensionless quantity with values between 0 and 1. $AD = 0$ means the dispersion is perfect and particles are homogeneously distributed inside the matrix. $AD = 1$ means the dispersion is worst with clusters, as shown in Fig. 3.10. To obtain the AD, we first identify the particle boundaries (Fig. 3.9b) from the optical image (Fig. 3.9a), and then locate the particles'

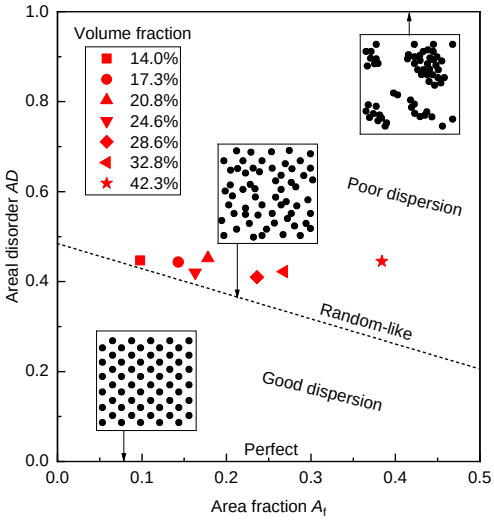

Figure 3.10: Quantitative analysis of the particle dispersion in composites with different volume fractions. The Area fraction A_f is obtained via image processing.

center of mass (Fig. 3.9c). Next, we build the Delaunay network (Fig. 3.9d) to calculate AD. Fig. 3.10 shows the AD for the composites in Fig. 3.8. From Fig. 3.10, we can see that the dispersion of our composites is random-like.

A3: COMSOL SIMULATIONS FOR OBTAINING EDDY CURRENT DAMPING FORCES

A3.1. FEM: EDDY CURRENT DAMPING IN A GRAPHITE PLATE

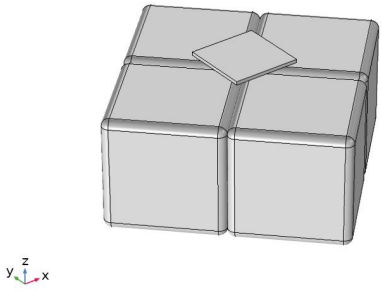

Figure 3.11: Geometry model of magnets and graphite plate.

This section details out the methodology we use to calculate the eddy current damp-

ing forces of a square graphite plate levitating above four permanent magnets. The geometry of the model is shown in Fig. 3.11.

We simulate the magnetic field using *COMSOL Multiphysics 5.6*. Assuming that the influence of the diamagnetic plate on the field is negligible, the integrated magnetic force on the plate, $\mathbf{F_B}$, can be determined using

$$\mathbf{F_B} = \nabla \int_{\mathcal{V}} \mathbf{M} \cdot \mathbf{B} \mathrm{d}\mathcal{V} = \frac{\mu_0}{2} \int_{\mathcal{V}} \nabla(\chi_x H_x^2 + \chi_y H_y^2 + \chi_z H_z^2) \mathrm{d}\mathcal{V}, \tag{3.3}$$

where χ_x, χ_y, χ_z are the magnetic susceptibility of the levitating plate in x, y, z directions, $\mathcal{V}$ is the volume of the plate, $\mathbf{B}$ is the magnetic field and $\mathbf{M}$ is the plate's magnetization. The components of the magnetic field inside the plate are $H_{x,y,z} = B_{x,y,z}/\mu$, where $\mu \approx \mu_0$ is the magnetic permeability of graphite. By calculating the magnetic force in z direction with different levitation gaps between the plate and magnets, the levitation height where the z-component of magnetic force is equal and opposite to the gravitational force is obtained. Using the levitation height, the stiffness of the magnetic force k can then obtained by taking the derivative of F_z over z at the equilibrium point. Next, the resonance frequency f_{res} is calculated using $f_{\text{res}} = \frac{1}{2\pi}\sqrt{\frac{k}{m}}$, where m is the mass of the plate.

Then, we simulate the eddy current damping of the plate. We note that when a conductor moves with velocity vector $\mathbf{v}$ through a magnetic flux density field $\mathbf{B}$, the charge carriers inside the conductor feel an electric field $\mathbf{v} \times \mathbf{B}$ due to the Lorentz' force in addition to the field from the electric potential V_e, that generates an eddy current density $\mathbf{J}$ given by

$$\mathbf{J} = -\sigma \nabla V_e + \sigma(\mathbf{v} \times \mathbf{B}), \tag{3.4}$$

where σ is the electrical conductivity. By combining Eq. (3.4) with the current continuity condition $\nabla \cdot \mathbf{J} = 0$ and the boundary condition $\mathbf{J} \cdot \mathbf{n} = 0$ ($\mathbf{n}$ is the unit vector perpendicular to the boundary), we determine the eddy current density distribution $\mathbf{J}$ numerically for known $\mathbf{v}$, σ, $\mathbf{B}$. We then evaluate the the total damping contribution due to eddy currents as follows

$$\mathbf{F_e} = \int_{\mathcal{V}} \mathbf{J} \times \mathbf{B} \mathrm{d}\mathcal{V}, \tag{3.5}$$

where integration is done over the graphite plate volume $\mathcal{V}$. Noting that the eddy current damping force $\mathbf{F}_\text{e}$ is proportional and in the opposite direction of the velocity v, we then estimate the damping coefficient c. Finally, Q of the plate can be obtained as

$$Q = \frac{2\pi m f_{\text{res}}}{c}. \tag{3.6}$$

All the parameters used in our simulations for pyrolytic graphite plates are listed in Table 3.1.

A3.2 EDDY CURRENT DAMPING IN A COMPOSITE PLATE

In this section we explain how the eddy current damping forces of a composite plate levitating above four permanent magnets are calculated. Because the magnetic susceptibility and electrical conductivity of the epoxy are negligible, the composite is modeled only by the graphite spheres to reduce the computation time, assuming that spheres are

Table 3.1: Material properties used for the simulations of the levitating pyrolytic graphite.

Property	Symbol	Value	Unit
Density	ρ	2070	kg/m^3
Susceptibility $\perp$ [13]	χ_z	-450	$\times 10^{-6}$
Susceptibility $\parallel$ [13]	$\chi_{x,y}$	-85	$\times 10^{-6}$
Conductivity $\perp$[43]	σ_z	200	S/m
Conductivity $\parallel$[43]	$\sigma_{x,y}$	200000	S/m

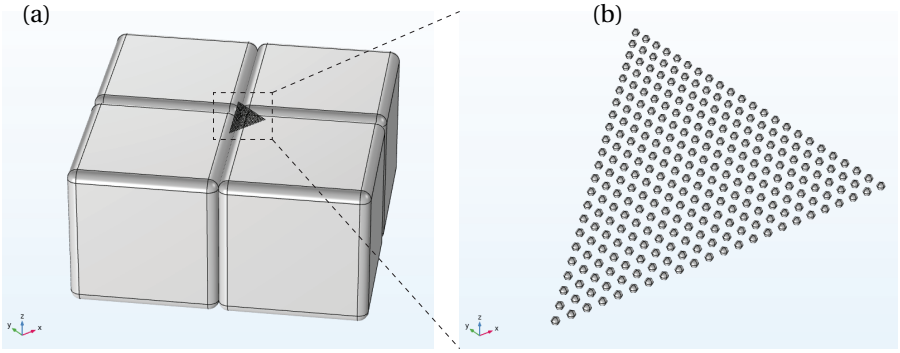

Figure 3.12: COMSOL model. (a) Geometry model of magnets and graphite particles. (b) Spherical graphite particles.

distributed homogeneously. As discussed in the main text, to account for experimental deviations from the theoretical model due to variations in particle size, composition, morphology and distribution, we use $C_r d$ as the effective particle size in the simulation for particles with mean size of d, where $C_r = 6.3$ is an effective particle size factor. Fig. 3.12a shows the geometry model of four permanent magnets and 1/8 fraction of the graphite particles. The simulation procedure is similar to that of graphite plates. The parameters used in our simulations for the composite plates are given in Table 3.2.

We note that graphite is inherently anisotropic [13]. However, in our fabrication procedure graphite particles are randomly oriented in the epoxy matrix, and thus by considering all possible orientations in the matrix, the local anisotropy can be averaged out and the effective macroscopic behavior can be viewed isotropic. For this reason , in our study we treat the magnetic susceptibility of graphite as an effective value χ_{eff} which we evaluate by fitting our FEM simulations to the measured levitation height of the composite from experiments. In Fig. 3.13 we showcase how χ_{eff} is estimated from experiments. We first measure the natural levitation gap of the composite using the Keyence microscope. By knowing the natural levitation gap and the gravitational force we then use our FEM model to estimate the magnetic force for different values of χ_{eff}, and find the best value that fits the experimental finding. In Fig. 3.13 we show this procedure for a composite plate with $1.8 \times 1.8 \times 0.09\,\text{mm}^3$, with volume fraction $V_f = 0.21$ and particle size $d = 17.6\,\mu$m. It can be seen that the green line which matches our experimental result is below the upper bound of the magnetic forces evaluated considering

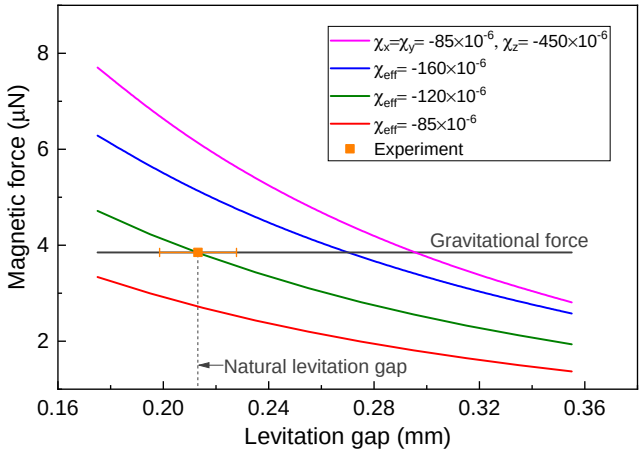

Figure 3.13: Magnetic force as a function of levitation gap obtained by COMSOL simulations using different susceptibilities (solid lines), and the measured natural levitation gap (dot).

anisotropic magnetic susceptibilities, and the evaluated effective magnetic susceptibility $\chi_{\text{eff}} = -120 \times 10^{-6}$ agrees well with the reported value in reference [44].

Table 3.2: Material properties of the graphite particles and epoxy used for the simulations of the levitating composite plates.

Property	Symbol	Value	Unit
Graphite density	ρ_g	2250	kg/m^3
Epoxy density	ρ_e	1100	kg/m^3
Graphite susceptibility	χ_{eff}	-120	$\times 10^{-6}$
Graphite resistivity[43]	ρ_r	1/200000	Ω m

Fig. 3.14a-c show the change of mass m, resonance frequency f_{res} and damping coefficient c of composite plates with different particle volume fraction V_f. Fig. 3.14d-f show the change of mass m, resonance frequency f_{res} and damping coefficient c of composite plates with different plate length L. Fig. 3.14g-i show the change of mass m, resonance frequency f_{res} and damping coefficient c of composite plates with different particle size d.

A4: ELECTRICAL CONDUCTIVITY OF THE COMPOSITES

Fig. 3.15 shows the bulk conductivity of two composites made from $d = 8.6\,\mu$m and $d = 17.6\,\mu$m particles with different volume fractions. The conductivity is measured by the two-point measurement method with Agilent 4263B LCR meter (Santa Clara, CA, USA). It can be seen from the figure that the bulk conductivity of the composite is increasing with higher graphite volume fractions.

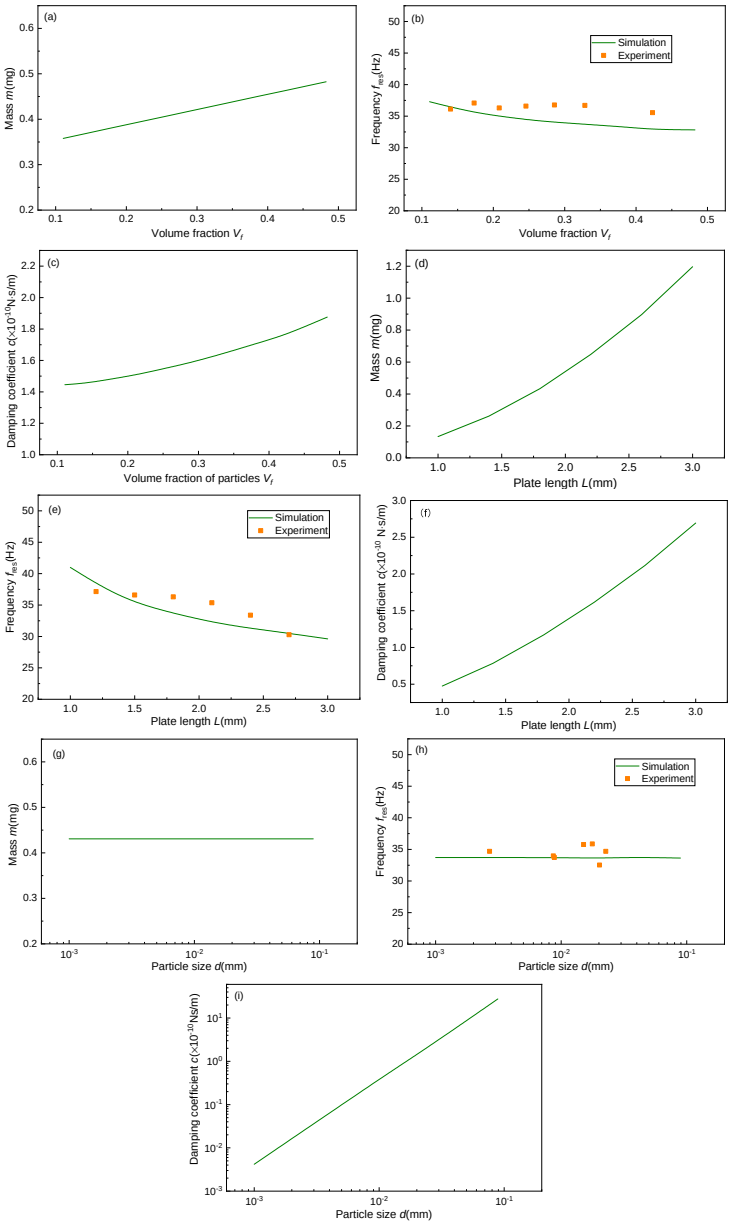

Figure 3.14: (a-c) Changes in mass m, resonance frequency f_{res} and damping coefficient c of $1.8 \times 1.8 \times 0.09\,\text{mm}^3$ composite plates with d=17.6 μm particles and different volume fraction V_{f}; (d-f) Changes in mass m, resonance frequency f_{res} and damping coefficient c of composite plates with d=17.6 μm particles and volume fraction $V_{\text{f}} = 0.21$, but different plate length L; (g-i) Changes in mass m, resonance frequency f_{res} and damping coefficient c of $1.8 \times 1.8 \times 0.09\,\text{mm}^3$ composite plates with volume fraction $V_{\text{f}} = 0.32$ and different particle size d. The lines correspond to data obtained from COMSOL simulations and dots represent measured data.

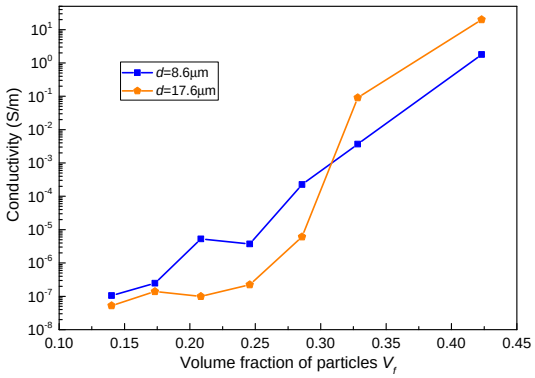

Figure 3.15: Conductivity of two composites as a function of volume fraction.

A5: ANALYTICAL MODELLING OF EDDY CURRENT DAMPING

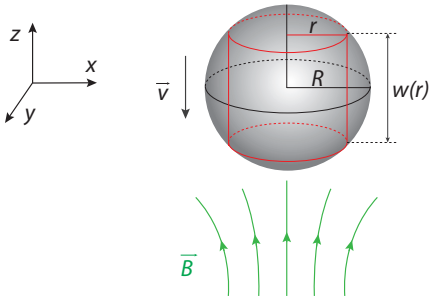

Figure 3.16: A sphere model.

In this section we obtain the Q-factor of a diamagnetic particle moving in a magnetic field, analytically. We consider a spherical particle with radius $R = d/2$ that moves inside a magnetic field $\vec{B}$ as shown in Fig. 3.16. To calculate the eddy current loss of the sphere, we assume the sphere consists of cylinders with varying radius r and height $w(r)$ as shown in Fig. 3.16. It is also assumed that the sphere is small compared to the magnetic field distribution and that the magnetic field **B** is not changing in different locations on the sphere. According to Faraday's law of induction, the induced voltage on each ring (dr) of the sphere can then be calculated as [26]:

$$emf = \frac{\mathrm{d}\Phi}{\mathrm{d}t} = \frac{\mathrm{d}(\pi r^2 B)}{\mathrm{d}t} = \pi r^2 \frac{\mathrm{d}B}{\mathrm{d}z}\frac{\mathrm{d}z}{\mathrm{d}t} = \pi r^2 v \frac{\mathrm{d}B}{\mathrm{d}z}, \tag{3.7}$$

where Φ is the magnetic flux, and v is the velocity of the sphere. The induced current in the ring will then be

$$\mathrm{d}I = \pi r^2 v \frac{\mathrm{d}B}{\mathrm{d}z}\frac{w(r)\mathrm{d}r}{2\pi r \rho_\mathrm{r}}, \tag{3.8}$$

where ρ_r is the electrical resistivity of the sphere. Using Eq. (3.7) and (3.8), the power loss in the ring can then be calculated as

$$dP = \pi r^3 v^2 \left(\frac{dB}{dz}\right)^2 \frac{w(r)dr}{2\rho_r}, \tag{3.9}$$

from which the total loss inside the sphere will become

$$P = \pi v^2 \left(\frac{dB}{dz}\right)^2 \frac{1}{2\rho_r} \int_0^R r^3 2\sqrt{R^2 - r^2} dr = \frac{2\pi v^2 R^5}{15\rho_r} \left(\frac{dB}{dz}\right)^2. \tag{3.10}$$

Finally, the eddy current loss per unit volume of the sphere becomes

$$P_{unit} = \frac{v^2 R^2}{10\rho_r} \left(\frac{dB}{dz}\right)^2. \tag{3.11}$$

Considering $P_{unit} = F_{eddy} v = c_{unit} v^2$, and using Eq. (3.11), the damping coefficient c_{unit} can then be expressed as

$$c_{unit} = \frac{R^2}{10\rho_r} \left(\frac{dB}{dz}\right)^2. \tag{3.12}$$

Which results in the following expression for the Q-factor solely due to eddy currents:

$$Q_{sphere} = \frac{2\pi m_{sphere} f_{res}}{c_{sphere}} = \frac{2\pi \rho_d V_{sphere} f_{res}}{c_{unit} V_{sphere}} = \frac{2\pi \rho_d f_{res}}{c_{unit}} = \frac{20\pi f_{res} \rho_d \rho_r}{R^2 (dB/dz)^2}, \tag{3.13}$$

in which m_{sphere} is the mass of the particle, f_{res} is the resonance frequency, ρ_d is the density and V_{sphere} is the volume of the sphere.

For a composite plate consisting of spheres of radius R dispersed in an insulating matrix, the Q can be determined similar to Eq.(3.13) as follows:

$$Q_{plate} = \frac{2\pi m_{plate} f_{res}}{c_{plate}} = \frac{2\pi \rho_p V_{plate} f_{res}}{\int_{V_{spheres}} c_{unit} dV_{spheres}} = \frac{20\pi f_{res} \rho_p \rho_r V_{plate}}{R^2 \int_{V_{spheres}} \left(\frac{dB}{dz}\right)^2 dV_{spheres}}, \tag{3.14}$$

where ρ_p is the density of the composite plate, V_{plate} is the volume of the plate, and $V_{spheres}$ is the volume of the spherical particles. For a graphite/epoxy composite plate with volume fraction of V_f, the Q is then

$$\begin{aligned} Q_{plate} &= \frac{20\pi f_{res} \rho_r V_{plate} (V_f(\rho_g - \rho_e) + \rho_e)}{(C_r R)^2 \int_{V_{spheres}} \left(\frac{dB}{dz}\right)^2 dV_{spheres}} \\ &= \frac{20\pi f_{res} \rho_r V_{plate} (V_f(\rho_g - \rho_e) + \rho_e)}{(C_r R)^2 B_2 V_f V_{plate}} \\ &= \frac{20\pi f_{res} \rho_r ((\rho_g - \rho_e) + \rho_e / V_f)}{(C_r R)^2 B_2}, \end{aligned} \tag{3.15}$$

where ρ_g is the density of graphite, ρ_e is the density of epoxy, and C_r is the apparent particle size factor that accounts for the uncertainties related to particle size, morphology and distribution. And

$$B_2 = \frac{\int_{V_{plate}} \left(\frac{dB}{dz}\right)^2 dV_{plate}}{V_{plate}}, \tag{3.16}$$

that can be obtained numerically using Comsol.

A6: Q-FACTORS AND ACCELERATION NOISE FLOOR OF STATE-OF-THE-ART LEVITODYNAMIC SYSTEMS

In Table 3.3-3.5 we list the Qs and acceleration noise floors $\sqrt{S_{\mathrm{aa}}}$ of different levitodynamic systems showed in Fig. 3.5 of the main text. In Table 3.3, the Qs were measured directly without feedback cooling either at room temperature or cryogenic temperature. In Table 3.4, we show the Qs measured at room temperature with feedback cooling and the natural Qs estimated at room temperature without feedback cooling. In Table 3.5, the reported acceleration noise floor of different levitodynamic systems under different measurement conditions are listed. The data marked with [∗] are estimated using the following equation [19]:

$$\sqrt{S_{aa}} = \sqrt{\frac{8\pi f_{\mathrm{res}} k_{\mathrm{B}} T}{mQ}} \tag{3.17}$$

where f_{res} is the resonance frequency, m is the mass, Q is the quality factor, T is the temperature and k_B is the Boltzmann constant.

Table 3.3: Q-factors of different levitodynamic systems without feedback cooling (RT: room temperature).

mass(kg)	Q	Levitation method	Temperature	Reference
3.3×10^{-18}	1.0×10^{7}	optical	RT	[9]
3.7×10^{-14}	2.1×10^{4}		RT	[27]
9.6×10^{-17}	1.5×10^{6}	electrical	RT	[12]
6.1×10^{-10}	1.3×10^{7}	superconducting	4.2K	[11]
1.1×10^{-10}	1.0×10^{6}		<90K	[32]
5.7×10^{-11}	5.0×10^{4}		5K	[33]
4.0×10^{-6}	5.5×10^{3}		5K	[19]
2.7×10^{-13}	2.0×10^{7}	diamagnetic	3K	[30]
7.8×10^{-8}	1.5×10^{5}		RT	[31]
1.0×10^{-5}	362		RT	[15]
2.3×10^{-5}	176		RT	[15]
3.9×10^{-5}	115		RT	[15]
6.3×10^{-5}	76		RT	[15]
2.3×10^{-6}	4.6×10^{5}		RT	this work

Table 3.4: *Q*-factors of different levitodynamic systems with feedback cooling.

mass(kg)	With feedback cooling		Estimated natural damping		Levitation method	Ref
	Q	Effective temperature	Q	Effective temperature		
1.4×10^{-19}	440	3mK	4.4×10^{7}	300K	optical	[10]
3.1×10^{-17}	38.6	460mK	2.5×10^{4}	300K	optical	[28]
3.0×10^{-14}	14.8	10K	445	300K	optical	[29]
2.5×10^{-10}	175	9K	5.8×10^{3}	300K	diamagnetic	[25]
3.1×10^{-15}	13.7	1.2mK	3.2×10^{6}	295K		[24]

Table 3.5: Acceleration noise floor of different levitodynamic systems showed in Fig. 3.5 of the main text. Data marked with [∗] represent the estimated value.

mass(kg)	$\sqrt{S_{aa}}$ (g/$\sqrt{\text{Hz}}$)	levitation method	Effective temperature	Reference	Note
3.3×10^{-18}	1.1×10^{-3}	optical	RT	[9]	∗
3.7×10^{-14}	1.2×10^{-4}		RT	[27]	∗
1.4×10^{-19}	3.9×10^{-3}		3mK	[10]	feedback cooling, ∗
3.1×10^{-17}	5.4×10^{-3}		460mK	[28]	feedback cooling
3.0×10^{-14}	7.0×10^{-4}		10K	[29]	feedback cooling
1.4×10^{-18}	2.3×10^{-3}		3K	[34]	feedback cooling
8.4×10^{-14}	1.2×10^{-5}		~	[35]	feedback cooling
1.4×10^{-13}	3.6×10^{-5}		1K	[36]	feedback cooling
1.5×10^{-13}	7.5×10^{-6}		~mK	[37]	feedback cooling
1.2×10^{-11}	4.0×10^{-7}		~	[17]	feedback cooling
9.4×10^{-13}	9.5×10^{-8}		50 μK	[38]	feedback cooling
9.6×10^{-17}	2.4×10^{-5}	electrical	RT	[12]	∗
6.1×10^{-10}	8.5×10^{-10}	superconducting	4.2K	[11]	∗
1.1×10^{-10}	5.0×10^{-8}		<90K	[32]	∗
5.7×10^{-11}	1.6×10^{-8}		5K	[33]	∗
4.0×10^{-6}	1.2×10^{-10}		5K	[19]	∗
2.7×10^{-13}	4.8×10^{-9}	diamagnetic	3K	[30]	∗
7.8×10^{-8}	9.7×10^{-10}		RT	[31]	-
2.5×10^{-10}	3.6×10^{-8}		9K	[25]	feedback cooling
3.1×10^{-15}	3.1×10^{-6}		1.2mK	[24]	feedback cooling, ∗
1.0×10^{-5}	2.6×10^{-9}		RT	[15]	∗
2.3×10^{-5}	2.3×10^{-9}		RT	[15]	∗
3.9×10^{-5}	2.1×10^{-9}		RT	[15]	∗
6.3×10^{-5}	1.9×10^{-9}		RT	[15]	∗
2.3×10^{-6}	1.6×10^{-10}		RT	this work	∗

REFERENCES

[1] G. S. MacCabe, H. Ren, J. Luo, J. D. Cohen, H. Zhou, A. Sipahigil, M. Mirhosseini, and O. Painter, "Nano-acoustic resonator with ultralong phonon lifetime", Science **370**, 840–843 (2020).

[2] M. Bereyhi, A. Beccari, R. Groth, S. Fedorov, A. Arabmoheghi, N. Engelsen, and T. Kippenberg, "Hierarchical tensile structures with ultralow mechanical dissipation", Nature Communications **13**, 3097 (2022).

[3] M. A. Kemp, M. Franzi, A. Haase, E. Jongewaard, M. T. Whittaker, M. Kirkpatrick, and R. Sparr, "A high q piezoelectric resonator as a portable vlf transmitter", Nature communications **10**, 1–7 (2019).

[4] A. Kumar, M. Gupta, P. Pitchappa, T. C. Tan, U. Chattopadhyay, G. Ducournau, N. Wang, Y. Chong, and R. Singh, "Active ultrahigh-q (0.2×10^6) thz topological cavities on a chip", Advanced Materials **2202370**, 1–8 (2022).

[5] S. B. Cataño-Lopez, J. G. Santiago-Condori, K. Edamatsu, and N. Matsumoto, "High-q milligram-scale monolithic pendulum for quantum-limited gravity measurements", Physical review letters **124**, 221102 (2020).

[6] D. Shin, A. Cupertino, M. H. de Jong, P. G. Steeneken, M. A. Bessa, and R. A. Norte, "Spiderweb nanomechanical resonators via bayesian optimization: inspired by nature and guided by machine learning", Advanced Materials **34**, 2106248 (2022).

[7] E. Brandt, "Levitation in physics", Science **243**, 349–355 (1989).

[8] C. Gonzalez-Ballestero, M. Aspelmeyer, L. Novotny, R. Quidant, and O. Romero-Isart, "Levitodynamics: levitation and control of microscopic objects in vacuum", Science **374**, eabg3027 (2021).

[9] J. Gieseler, B. Deutsch, R. Quidant, and L. Novotny, "Subkelvin parametric feedback cooling of a laser-trapped nanoparticle", Physical review letters **109**, 103603 (2012).

[10] J. Vovrosh, M. Rashid, D. Hempston, J. Bateman, M. Paternostro, and H. Ulbricht, "Parametric feedback cooling of levitated optomechanics in a parabolic mirror trap", JOSA B **34**, 1421–1428 (2017).

[11] A. Vinante, P. Falferi, G. Gasbarri, A. Setter, C. Timberlake, and H. Ulbricht, "Ultralow mechanical damping with meissner-levitated ferromagnetic microparticles", Physical Review Applied **13**, 064027 (2020).

[12] A. Pontin, N. Bullier, M. Toroš, and P. Barker, "Ultranarrow-linewidth levitated nano-oscillator for testing dissipative wave-function collapse", Physical Review Research **2**, 023349 (2020).

[13] M. Simon and A. Geim, "Diamagnetic levitation: flying frogs and floating magnets", Journal of applied physics **87**, 6200–6204 (2000).

[14] K. A. Mirica, F. Ilievski, A. K. Ellerbee, S. S. Shevkoplyas, and G. M. Whitesides, "Using magnetic levitation for three dimensional self-assembly", Advanced Materials **23**, 1128, 4134–4140 (2011).

[15] X. Chen, A. Keşkekler, F. Alijani, and P. G. Steeneken, "Rigid body dynamics of diamagnetically levitating graphite resonators", Applied Physics Letters **116**, 243505 (2020).

[16]X. Chen, N. Kothari, A. Keşkekler, P. G. Steeneken, and F. Alijani, "Diamagnetically levitating resonant weighing scale", Sensors and Actuators A: Physical **330**, 112842 (2021).

[17]F. Monteiro, S. Ghosh, A. G. Fine, and D. C. Moore, "Optical levitation of 10-ng spheres with nano-g acceleration sensitivity", Physical Review A **96**, 063841 (2017).

[18]D. C. Moore and A. A. Geraci, "Searching for new physics using optically levitated sensors", Quantum Science and Technology **6**, 014008 (2021).

[19]C. Timberlake, G. Gasbarri, A. Vinante, A. Setter, and H. Ulbricht, "Acceleration sensing with magnetically levitated oscillators above a superconductor", Applied Physics Letters **115**, 224101 (2019).

[20]R. Middlemiss, A. Samarelli, D. Paul, J. Hough, S. Rowan, and G. Hammond, "Measurement of the earth tides with a mems gravimeter", Nature **531**, 614–617 (2016).

[21]J. Schmöle, M. Dragosits, H. Hepach, and M. Aspelmeyer, "A micromechanical proof-of-principle experiment for measuring the gravitational force of milligram masses", Classical and Quantum Gravity **33**, 125031 (2016).

[22]C. Marletto and V. Vedral, "Gravitationally induced entanglement between two massive particles is sufficient evidence of quantum effects in gravity", Physical review letters **119**, 240402 (2017).

[23]A. Belenchia, R. M. Wald, F. Giacomini, E. Castro-Ruiz, Č. Brukner, and M. Aspelmeyer, "Quantum superposition of massive objects and the quantization of gravity", Physical Review D **98**, 126009 (2018).

[24]B. R. Slezak, C. W. Lewandowski, J.-F. Hsu, and B. D'Urso, "Cooling the motion of a silica microsphere in a magneto-gravitational trap in ultra-high vacuum", New Journal of Physics **20**, 063028 (2018).

[25]C. W. Lewandowski, T. D. Knowles, Z. B. Etienne, and B. D'Urso, "High-sensitivity accelerometry with a feedback-cooled magnetically levitated microsphere", Physical Review Applied **15**, 014050 (2021).

[26]A. Taghvaei, H. Shokrollahi, K. Janghorban, and H. Abiri, "Eddy current and total power loss separation in the iron–phosphate–polyepoxy soft magnetic composites", Materials & Design **30**, 3989–3995 (2009).

[27]T. Li, S. Kheifets, and M. G. Raizen, "Millikelvin cooling of an optically trapped microsphere in vacuum", Nature Physics **7**, 527–530 (2011).

[28]G. Ranjit, M. Cunningham, K. Casey, and A. A. Geraci, "Zeptonewton force sensing with nanospheres in an optical lattice", Physical Review A **93**, 053801 (2016).

[29]G. Ranjit, D. P. Atherton, J. H. Stutz, M. Cunningham, and A. A. Geraci, "Attonewton force detection using microspheres in a dual-beam optical trap in high vacuum", Physical Review A **91**, 051805 (2015).

[30]Y. Leng, R. Li, X. Kong, H. Xie, D. Zheng, P. Yin, F. Xiong, T. Wu, C.-K. Duan, Y. Du, et al., "Mechanical dissipation below 1 μ hz with a cryogenic diamagnetic levitated microoscillator", Physical Review Applied **15**, 024061 (2021).

[31] F. Xiong, P. Yin, T. Wu, H. Xie, R. Li, Y. Leng, Y. Li, C. Duan, X. Kong, P. Huang, et al., "Lens-free optical detection of thermal motion of a submillimeter sphere diamagnetically levitated in high vacuum", Physical Review Applied **16**, L011003 (2021).

[32] J. Gieseler, A. Kabcenell, E. Rosenfeld, J. Schaefer, A. Safira, M. J. Schuetz, C. Gonzalez-Ballestero, C. C. Rusconi, O. Romero-Isart, and M. D. Lukin, "Single-spin magnetomechanics with levitated micromagnets", Physical review letters **124**, 163604 (2020).

[33] T. Wang, S. Lourette, S. R. O'Kelley, M. Kayci, Y. Band, D. F. J. Kimball, A. O. Sushkov, and D. Budker, "Dynamics of a ferromagnetic particle levitated over a superconductor", Physical Review Applied **11**, 044041 (2019).

[34] D. Hempston, J. Vovrosh, M. Toroš, G. Winstone, M. Rashid, and H. Ulbricht, "Force sensing with an optically levitated charged nanoparticle", Applied Physics Letters **111**, 133111 (2017).

[35] A. Kawasaki, A. Fieguth, N. Priel, C. P. Blakemore, D. Martin, and G. Gratta, "High sensitivity, levitated microsphere apparatus for short-distance force measurements", Review of Scientific Instruments **91**, 083201 (2020).

[36] D. C. Moore, A. D. Rider, and G. Gratta, "Search for millicharged particles using optically levitated microspheres", Physical review letters **113**, 251801 (2014).

[37] A. D. Rider, C. P. Blakemore, G. Gratta, and D. C. Moore, "Single-beam dielectric-microsphere trapping with optical heterodyne detection", Physical Review A **97**, 013842 (2018).

[38] F. Monteiro, W. Li, G. Afek, C.-l. Li, M. Mossman, and D. C. Moore, "Force and acceleration sensing with optically levitated nanogram masses at microkelvin temperatures", Physical Review A **101**, 053835 (2020).

[39] C. Whittle, E. D. Hall, S. Dwyer, N. Mavalvala, V. Sudhir, R. Abbott, A. Ananyeva, C. Austin, L. Barsotti, J. Betzwieser, et al., "Approaching the motional ground state of a 10-kg object", Science **372**, 1333–1336 (2021).

[40] Y. Michimura and K. Komori, "Quantum sensing with milligram scale optomechanical systems", The European Physical Journal D **74**, 1–14 (2020).

[41] H. Yu, L. McCuller, M. Tse, N. Kijbunchoo, L. Barsotti, and N. Mavalvala, "Quantum correlations between light and the kilogram-mass mirrors of ligo", Nature **583**, 43–47 (2020).

[42] D. Bray, S. Gilmour, F. Guild, T. Hsieh, K. Masania, and A. Taylor, "Quantifying nanoparticle dispersion: application of the delaunay network for objective analysis of sample micrographs", Journal of materials science **46**, 6437–6452 (2011).

[43] J. Pappis and S. Blum, "Properties of pyrolytic graphite", Journal of the American Ceramic Society **44**, 592–597 (1961).

[44] M. Boukallel, J. Abadie, and E. Piat, "Levitated micro-nano force sensor using diamagnetic materials", in 2003 ieee international conference on robotics and automation (cat. no. 03ch37422), Vol. 3 (IEEE, 2003), pp. 3219–3224.

4

NONLINEAR DYNAMICS OF DIAMAGNETICALLY LEVITATING RESONATORS

The ultimate isolation offered by levitation offers new opportunities for studying fundamental science and realizing ultra-sensitive sensors. Among different levitation schemes, diamagnetic levitation is attractive because it allows stable levitation at room temperature without continuous power supply. While the dynamics of levitating objects in the linear regime is well studied, their nonlinear dynamics has remained largely unexplored. Here, we experimentally and theoretically study the nonlinear dynamic response of graphite resonators that levitate in permanent magnetic traps. By large amplitude actuation of the diamagnetic plates, we drive them into nonlinear regime while measuring their motion using laser Doppler interferometry. In contrast to common nanomechanical resonators, that show an increased stiffness at high amplitude due to nonlinear geometric effects, we observe a resonance frequency reduction with amplitude that is attributed to the softening effect of the magnetic force. To account for this, we analyze the asymmetric magnetic potential and construct a model that captures the experimental nonlinear dynamic behavior over a wide range of excitation forces. We also investigate the linearity of damping forces on the plate, concluding that while eddy current damping is linear over a large range, gas damping opens a route for tuning nonlinear damping forces via the squeeze-film effect.

Parts of this chapter are to be submitted in a journal by X. Chen, Tjebbe de Lint, F. Alijani, P. G. Steeneken.

4.1. INTRODUCTION

Gaining control over the dynamics of levitating objects has been a long sought goal, both because contactless levitation provides extreme isolation from external sources of heat and friction and because it allows six degrees-of-freedom motion. Recently, the interest in the field of levitodynamics[1] has surged, stimulated by the demonstration of quantum ground state cooling [2, 3] and the use of extremely high-Q levitating resonators for highly-sensitive sensors [4–6]. Diamagnetic levitation has the advantage of being the only passive levitation method that does not require continuous energy supply or cryogenic temperatures [5, 7, 8], which differentiates it from other kinds of levitation schemes [1, 9] like optical, superconducting and electrical levitation. Moreover, the passive, zero power nature of diamagnetic levitation does not incur heating and noise that can be limits in optical and electrical schemes[4, 10, 11]. Moreover, suitably designed magnetic traps from permanent magnets allow stable diamagnetic levitation in high vacuum without active feedback[8], enabling levitation of high-mass macroscopic objects, that provide increased sensitivity in accelerometers[12] and gravitational field sensors[13, 14].

In contrast to the low-amplitude linear dynamics of levitating resonators[5, 7], their large-amplitude motion has received relatively little attention. Since damping forces are small in levitating systems, small forces are often sufficient to drive resonators into the high-amplitude regime[15, 16] which is relevant for applications like levitating mirrors, translation stages, rotors and pumps. Moreover, high-amplitude oscillation improves the signal-to-noise ratio of resonant sensors[17, 18]. However, the amplitude of these devices cannot be increased indefinitely due to the presence of nonlinear effects which constrain the operation range of levitating devices and affecting their performance. A good understanding of the nonlinear dynamic effects that govern the dynamics of levitating resonators in the high-amplitude regime is therefore important for their application.

Here, we study the nonlinear dynamics of diamagnetic graphite plates that stably levitate in a magnetic trap formed by four permanent magnets. By measuring the frequency response of the plates in vacuum and driving their motion by base excitation, the nonlinearity of the resonant motion is determined and analyzed. By characterization of the magnetic forces it is shown that the magnetic levitation potential is the largest source of nonlinearity. By rising the driving force, the frequency response of the plate in the nonlinear dynamic regime is obtained, in close agreement with models based on the measured nonlinear magnetic stiffness. Finally, we perform nonlinear dynamic measurements in air, which show that eddy current damping is linear, while squeeze-film gas-damping forces contribute strongly to nonlinear damping.

4.2. RESULTS

4.2.1. EXPERIMENTAL METHODS

The magnetic levitation system used in our experiments consists of a pyrolytic graphite plate and four permanent magnets, as shown in Fig. 4.1b. The graphite is purchased from MTI Corporation and cut into a $10 \times 10 \times 0.28\,\mathrm{m}^3$ plate using a Optec micro laser cutter, after which its surface is polished using sand paper with 5 μm grains to improve the reflected optical readout signal. The plate levitates stably above four cubic NdFeB

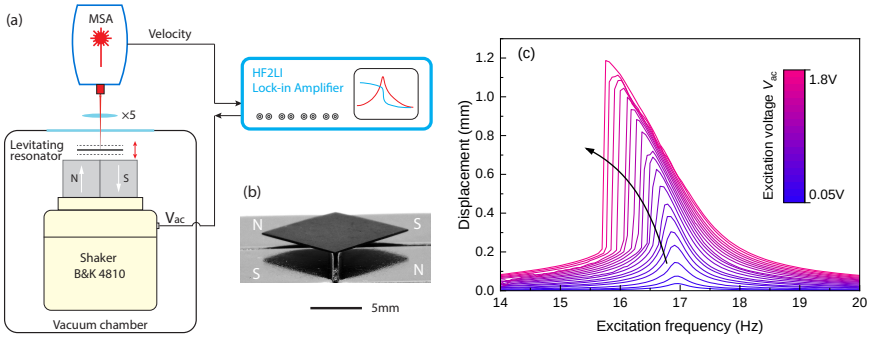

Figure 4.1: Measurement setup and nonlinear frequency response of a diamagnetically levitating plate. (a) Schematic of the experimental setup consisting of a Polytec Laser Doppler Vibrometer MSA400 for velocity readout and a Bruel & Kjaer shaker 4810 for base excitation. The excitation voltage is generated by a Zurich lock-in amplifier HF2LI that drives the levitating plate to vibrate in the vertical direction. The vibration signal is recorded by the MSA vibrometer and transferred to the lock-in amplifier for signal analysis. (b) Image of a $10 \times 10 \times 0.28\,\mathrm{m}^3$ plate levitating over four 12 mm cubic NdFeB magnets with alternating magnetization, where N stands for north pole and S stands for south pole. (c) Frequency response curves of the levitating plate excited by different driving voltage when backwards sweeping the frequency from 20 Hz to 14 Hz.

4

magnets in a checkerboard arrangement with alternating out-of-plane magnetization (Fig. 4.1b). In order to obtain a minimum magnetic potential, the plate rotates under the effect of the magnetic field until it attains a 45° angle between its edges and the edges of the magnets. The natural levitation gap where the gravitational force of the plate equals the magnetic force is $H_0 = 1.18\,\mathrm{mm}$, as measured by a Keyence digital microscope (VHX-6000).

To drive the levitating plate into motion, we use a mini shaker which is attached under the magnets as shown in Fig. 4.1a. To detect the motion of the levitating plate, we use a Polytec Laser Doppler Vibrometer to measure the out-of-plane velocity of the plate. The spectral response of the plate is obtained by sweeping the excitation frequency around the plate's resonance using a Zurich Lock-in Amplifier. To eliminate effects[7] of air damping, measurements are conducted in a vacuum chamber at a pressure below 10^{-5}mbar. Fig. 4.1c shows the frequency response of the levitating plate when sweeping the excitation frequency downward from 20 Hz to 14 Hz, for different driving voltages. When the driving voltage is small $V_{ac} = 0.05\,\mathrm{V}$, the frequency response of the plate is linear with a resonance frequency of $f_\mathrm{r} = 16.9\,\mathrm{Hz}$ and a quality factor of $Q = 48$. With the excitation voltage increasing from 0.05 to 1.8 V, the peak frequency decreases and the displacement amplitude increases. Since the natural levitation gap is $H_0 = 1.18\,\mathrm{mm}$, the plate almost touches the magnets when driving with 1.8 V at the peak frequency, obtaining a displacement amplitude close to H_0 (see Fig. 4.1c). In the following we keep the driving voltage on the shaker below 1.8 V, to prevent impact of the plate on the magnets. The observed dynamics of the diamagnetic plate is clearly nonlinear, resembling a Duffing resonator with negative nonlinear stiffness. To analyze the origin of this nonlinear dynamics, characterization of the magnetic forces is needed.

4.2.2. NONLINEAR MAGNETIC FORCE

To analyze the nonlinear dynamic behaviour of the levitating plate, we first determine the stiffness of the magnetic force using experimental and analytic methods. As shown in the inset of Fig. 4.2a, there are only two forces acting on the plate when it is levitating in static equilibrium: the magnetic force and gravitational force. Since the gravitational force is independent of displacement, only the magnetic force influences the plate's stiffness.

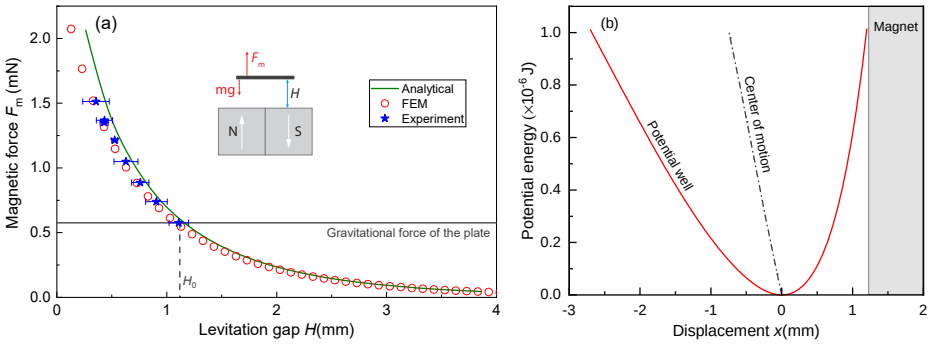

Figure 4.2: Position-dependent nonlinear magnetic force on the levitating plate. (a) The total mass m_{tot} of the levitating pyrolytic graphite plate is varied by adding non-magnetic polymer blocks. For each datapoint the levitation gap H between the bottom of the plate and the top of the permanent magnets is measured using a Keyence digital microscope, while the magnetic force is determined from the static equilibrium with the gravitational force $|F_m| = m_{\text{tot}}$. H_0 stands for the natural levitation gap of the plate. Experimental data are compared to FEM and analytical simulations. (b) Potential energy of the plate as a function of its displacement x ($x = H_0 - H$) based on the FEM $F_{\text{m}} - H$ curve in Fig. 4.2a. The dot-dash line shows its center of motion (midpoint between maximum and minimum displacement) when the plate is in free vibration.

To determine the position dependent magnetic force experimentally, we add non-magnetic polymer blocks with different weights on top of the diamagnetic graphite plate and measure the mass m_{tot} of the plate with blocks, from which we determine the magnetic force in static equilibrium which equals the gravitational force $F_m = m_{\text{tot}}g$. For each mass value, we measure the levitation gap H between plate and magnet using a Keyence digital microscope. To correct for non-uniformities in plate height, we measure the levitation gap on all four corners and obtain the average gap H. The results are shown in Fig. 4.2a, from which a clear reduction of the magnetic force with increasing gap H is observed. Since we cannot easily reduce the gravitational force on the plate below mg, where m is the mass of the graphite plate without polymer blocks, the levitation gap cannot be raised above H_0, the equilibrium gap for which $F_m(H_0) = mg$.

To determine the full $F_m(H)$ curves, also for $H > H_0$, we perform analytic and finite element method calculations. The magnetic force of the four magnets on the diamagnetic plate can be analytically calculated using:

$$\begin{aligned} \mathbf{F_B} &= \nabla \int_{\mathcal{V}} \mathbf{M} \cdot \mathbf{B} \mathrm{d}\mathcal{V} \\ &= \frac{\mu_0}{2} \int_{\mathcal{V}} \nabla(\chi_x H_x^2 + \chi_y H_y^2 + \chi_z H_z^2) \mathrm{d}\mathcal{V}, \end{aligned} \tag{4.1}$$

where $\mathcal{V}$ is the volume of the plate, $H_{x,y,z}$ are the components of the magnetic field vector, **M** is the magnetization vector and **B** the magnetic flux density vector. In this analysis it is assumed that the plate does not significantly affect the magnetic field, since its relative magnetic permeability is close to 1. To calculate the magnetic force acting on the plate, we model the magnetic field of the four permanent magnets analytically using the charge model[19] and numerically using COMSOL Multiphysics (see details of modelling in A1 and A2). In Fig. 4.2a the calculated magnetic force F_{m} is plotted as a function of levitation gap H for both methods. It can be seen that the COMSOL simulations correspond well with the experimental data, while a small discrepancy is observed for the analytical model, especially for small values of H. This discrepancy is attributed to the fact that the edges of the cube magnets are not sharp, but slightly rounded, an effect that is included in FEM but not in the analytical model.

In the linear regime, the magnetic stiffness around the equilibrium position H_0 is obtained from the slope of the graph in Fig. 4.2a, $k_L = \frac{\mathrm{d}F_z}{\mathrm{d}H} = 0.6625\,\mathrm{N/m}$. Knowing the mass of the plate $m = 5.88 \times 10^{-5}\,\mathrm{kg}$, the resonance frequency of the vertical rigid body mode of the plate is found to be $f_{res} = \frac{1}{2\pi}\sqrt{\frac{k_{\mathrm{L}}}{m}} = 16.89\,\mathrm{Hz}$, which matches closely with the measured value of $f_{\mathrm{res}} = 17.0\,\mathrm{Hz}$ (Fig. 4.1c).

However, for large amplitude motion, nonlinear terms in the force-displacement curve need to be taken into account. We describe the motion of the plate in terms of its displacement $x = H_0 - H$ with respect to the equilibrium position, for the total restoring force is given by $F_{\mathrm{r}} = F_{\mathrm{m}} - mg$. Fig. 4.2b shows the potential energy obtained by $\int F_{\mathrm{r}}\mathrm{d}x$ using the simulated magnetic force (red circles in Fig. 4.2a). It is observed from Fig. 4.2b that interestingly, the potential well is not symmetric around the axis $x = 0$, in contrast with many non-levitating mechanical systems that derive their nonlinear stiffness from nonlinear geometric effects. As a consequence, the center of motion (middle between maximum and minimum displacement) will be amplitude dependent and will not coincide with H_0 for large amplitude motion. For the maximal free vibration amplitude that the plate can sustain before colliding with the magnet, it displays a large assymmetry in its maximal displacement (zero kinetic energy) positions x_{max}=1.18 mm and x_{min}−2.5 mm, as shown in Fig. 4.2b.

The restoring force F_{r} of the plate as a function of its displacement x between $-3.0\,\mathrm{mm} < x < 1.2\,\mathrm{mm}$, as simulated by FEM, is plotted in Fig. 4.3a. A linear fit of the data at $x = 0$ is shown as a black solid line. It is interesting to note from Fig. 4.3a that, unlike conventional mechanical spring structures, like double-clamped beams that have symmetric force-displacement curves for reflection around $x = 0$, the force-displacement curve of the levitating plate is asymmetric. Whereas asymmetries induced by external forces in nonlinear resonators [20, 21] have recently received interest from the community for affecting nonlinear parameters and inducing nonlinear phenomena like frequency combs, this asymmetry is intrinsic in the diamagnetically levitating plates, due to the asymmetric arrangement of the permanent magnets below the plate and the effect of gravity. As a consequence of the asymmetry, the force-displacement curve in Fig. 4.3a shows hardening when $x > 0$ and softening when $x < 0$, implying that the magnetic force can not be fully described by a third order polynomial with Duffing-type nonlinear stiffness. To illustrate this, and determine the minimal degree of polynomial needed to capture the magnetic nonlinearity, we fit the FEM data around $x = 0$ with

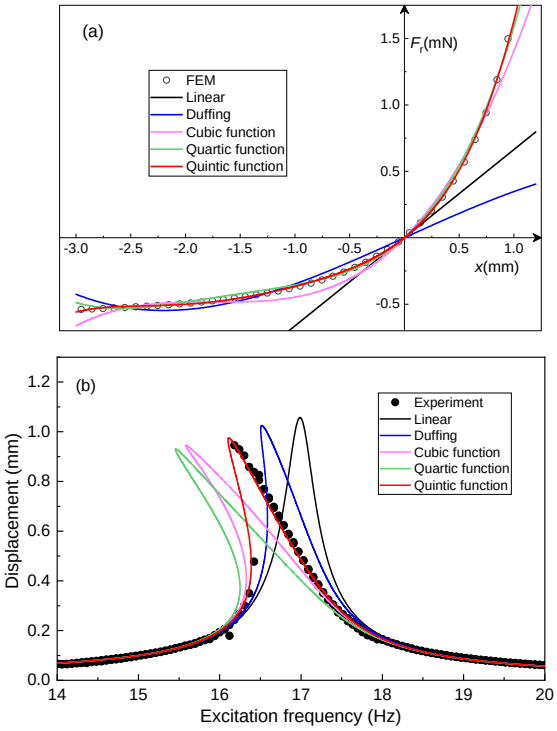

Figure 4.3: (a) Restoring force $F_r = F_m - mg$ of the levitating plate as a function of its displacement x when the plate is in free vibration. The hollow circles stand for the data obtained from FEM simulations and the lines are fits by polynomials from linear to quintic degree. (b) Frequency response curves of the plate with a driving voltage $V_{ac} = 1.5$V obtained by experiments (dots) and nonlinear dynamic simulations based on the polynomial stiffness functions from Fig. a (solid lines).

polynomials from first to fifth degree in Fig. 4.3a, and list the fit parameters in Table 4.1. The functional form of the polynomials is $F_r = k_{m1}x + k_{m2}x^2 + k_{m3}x^3 + k_{m4}x^4 + k_{m5}x^5$. We conclude from the fits that only the quintic, fifth degree polynomial fits well to the FEM data and will use this function constructing the plate's equation of motion and analyzing its nonlinear dynamics.

Table 4.1: Fit parameters of the polynomial restoring force obtained from Fig. 4.3a.

Function	k_{m1}(N/m)	k_{m2}(N/m^2)	k_{m3}(N/m^3)	k_{m4}(N/m^4)	k_{m5}(N/m^5)
Linear	0.6625	-	-	-	-
Duffing	0.3732	-	-2.571×10^4	-	-
Cubic	0.8110	479.4	9.381×10^4	-	-
Quartic	0.7338	564.0	2.315×10^5	3.549×10^7	-
Quintic	0.6625	530	3.25×10^5	1.114×10^8	1.474×10^{10}

4.2.3. DYNAMIC MODELLING

After having determined the restoring force $F_r(x)$, the equation of motion of the plate under base excitation can be written as:

$$m\ddot{x} + c_e\dot{x} + F_r(x-y) = 0. \tag{4.2}$$

where c_e is the linear damping coefficient due to eddy currents [7], $y = a\cos(\omega t)$ is the motion of the base as driven by the shaker, and the conversion between the base motion and the input voltage is $a = 0.0158V_{ac}$ (see also A3 for more details). For the quintic polynomial stiffness function, the nonlinear equation of motion is:

$$\begin{aligned} m\ddot{x} \quad + \quad & c_e\dot{x} + k_{m1}(x-y) + k_{m2}(x-y)^2 + \\ & k_{m3}(x-y)^3 + k_{m4}(x-y)^4 + k_{m5}(x-y)^5 = 0. \end{aligned} \tag{4.3}$$

Next, we nondimensionalize the system using the natural levitation gap H_0 and the natural period T. In terms of the nondimensional variables $\hat{x} = \frac{x}{H_0}$ and $\hat{t} = \frac{t}{T}$, the nondimensional equation of motion becomes:

$$\begin{aligned} \ddot{\hat{x}} \quad + \quad & 2\zeta_e\dot{\hat{x}} + \hat{x} - f_1\cos(\Omega\hat{t}) + \\ & \alpha\left(\hat{x} - f_1\cos(\Omega\hat{t})\right)^2 + \beta(\hat{x} - f_1\cos(\Omega\hat{t}))^3 + \\ & \alpha_2\left(\hat{x} - f_1\cos(\Omega\hat{t})\right)^4 + \beta_2(\hat{x} - f_1\cos(\Omega\hat{t}))^5 = 0, \end{aligned} \tag{4.4}$$

where $\alpha = \frac{k_{m2}H_0}{k_{m1}}$, $\beta = \frac{k_{m3}H_0^2}{k_{m1}}$, $\alpha_2 = \frac{k_{m4}H_0^3}{k_{m1}}$, $\beta_2 = \frac{k_{m5}H_0^4}{k_{m1}}$, $\zeta_e = \frac{c_e}{2\sqrt{k_{m1}m}}$, $f_1 = \frac{a}{H_0}$ and $\Omega = \frac{\omega}{\omega_{res}}$.

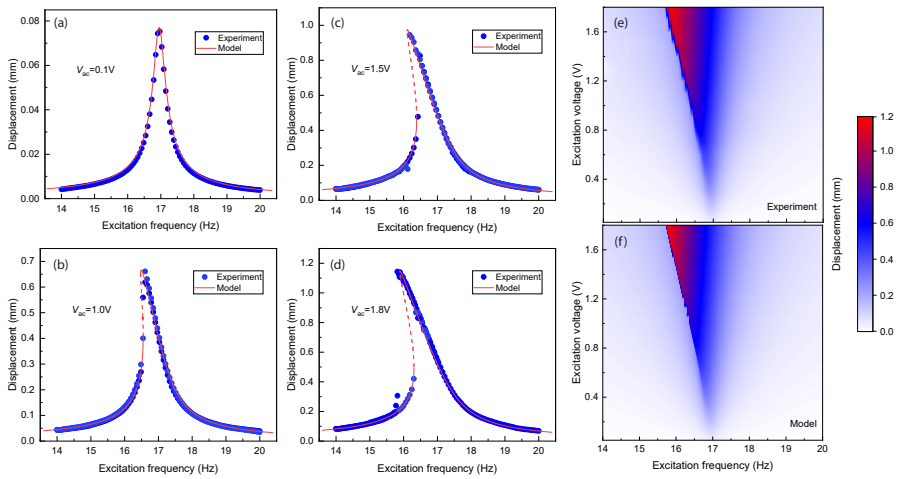

Figure 4.4: Comparison between the measured and modelled nonlinear frequency response of the levitating plate. (a)-(d) Experimental and modelled frequency response curves at four different driving voltages. The dots represent the experimental data and the lines represent the modelled data with stable (solid line) and unstable (dashed) solutions. Experimental (e) and modelled (f) frequency response curves with a wide range of driving voltages from 0.1 V to 1.8 V, where the color represents the vibration amplitude.

Using the stiffness parameters in Table 4.1, we solve equation Eq. (4.4) using AUTO [22] and obtain the amplitude-frequency curves for the 5 polynomial stiffness functions

determined from Fig. 4.3a and plot them in Fig. 4.3b, comparing it to the experimental data (Fig. 4.1c) for a driving voltage $V_{ac} = 1.5\,V$. We thus confirm that the quintic polynomial stiffness function corresponds well to the experimental response function at this driving force, in contrast to lower order polynomial stiffness function. We note that, even though the quartic function can capture the stiffness reasonably well (see Fig. 4.3a), it deviates substantially from the experimental frequency response curve. In Figs. 4.4a-d the experimental data for different driving voltages are compared to simulations based on the equation of motion (4.4) and the quintic polnomial nonlinear magnetic force. Fig. 4.4e shows the experimental frequency response curves for all the curves shown in Fig. 4.1c which correspond well to the modelled curves in Fig. 4.4f over a large range of displacement. This correspondence provides confidence that nonlinear dynamics might also prove to be a useful tool for determining the nonlinear stiffness in levitating systems where no analytical models for the trap potential are available.

4.2.4. GAS-INDUCED NONLINEAR DAMPING

After characterizing the nonlinear stiffness, we next study the nonlinearity of the damping in the levitating plate. It is known that eddy current forces dominate damping mechanism in vacuum[7]. The fact that we obtained close agreement between experiment and model in Fig. 4.4 while using only a single quality factor $Q = 48$, indicates that the eddy current damping force is quite linear, proportional to the plate velocity. This can also be seen from Fig. 4.5a, where the normalized maximum displacement x_{max}/a is almost independent of the driving amplitude a, a signature that nonlinear terms in the eddy current damping force are small.

Since operating in air is favorable for many types of sensors, we next measure the levitating plate's frequency response in open air to study the influence of air on its nonlinear dynamics. The experimental procedure is similar as shown in Fig. 4.1a, except that the experiments are conducted in air at atmospheric pressure at room temperature without the vacuum chamber. In Fig. 4.5b, we show normalized frequency response curves for four excitation forces. In contrast to the results measured in vacuum (Fig. 4.5a), a clear reduction in the normalized amplitude is observed when driven at higher voltages. This reduction is a clear signature of nonlinear damping, which originates from air damping [23]. Because the air gap between the levitating plate and the magnets is relatively small ($H_0 = 1.189\,mm$), it is likely that the major source of nonlinear damping is squeeze-film damping [24], which is proportional to $\dot{x}/H^3$) , leading to the following equation of motion:

$$m\ddot{x} + c_e\dot{x} + \frac{c_n}{(1-\frac{x-y}{H_0})^3}\dot{x} + F_r(x-y) = 0, \tag{4.5}$$

where c_n is the nonlinear squeeze-film damping coefficient. Using Reynold's equation, the damping coefficient of a square plate can be written as [25]:

$$c_n = \frac{0.42\mu(L+\Delta L)^4}{H_0^3}, \tag{4.6}$$

where $\mu = 1.825 \times 10^{-5}\,kg/(m\cdot s)$ is the viscosity of air under atmospheric conditions,

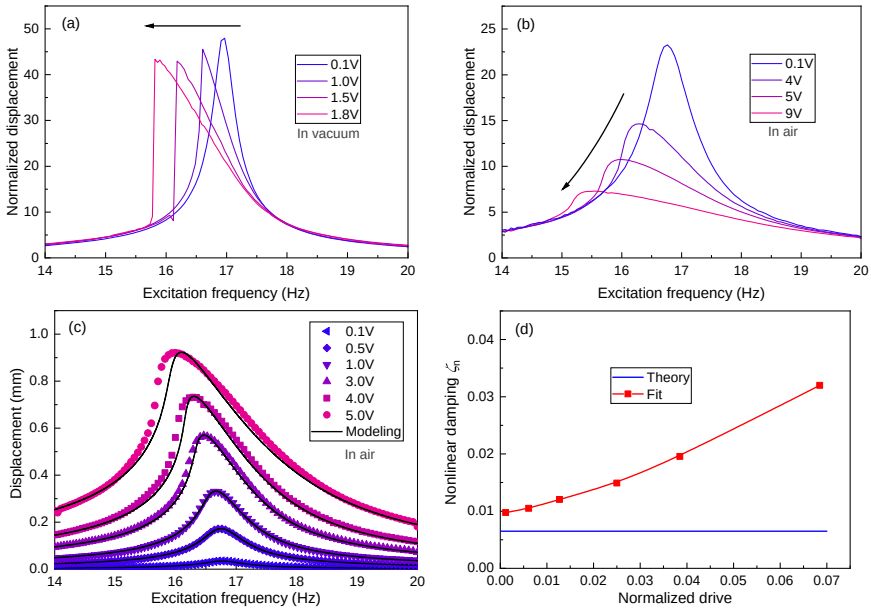

Figure 4.5: Air-induced nonlinear damping. (a) Normalized frequency response curves with different excitation voltages measured in vacuum. (b) Normalized frequency response curves with different excitation voltages measured in air. (c) Frequency response curves with different excitation voltages measured in air and their corresponding modelled curves using Eq. (4.5). (d) Nonlinear damping ratio ζ_n as a function of normalized drive f_1. The red line represents the damping ratio used in fitting the curves shown in Fig. 4.5c. The blue line coresponds to the damping ratio calculated from Eq. (4.6).

$L = 10\,\text{mm}$ is the side length of the square plate and $\Delta L = 1.3H_0$ is the elongation of the plate taking into account the border effects.

Using c_n as a fit parameter, we can model the frequency response curves of the plate in air using Eq. (4.5) for different driving levels, as shown in Fig. 4.5c. We also note that in order to get a good fit, we need to adjust the resonance frequencies slightly due to the significant effect of air damping (see A4 for the resonance frequencies used in the fitting). It can be seen that the experimental data is quite well fitted by the squeeze-film damping model, although we did observe that the fitted value of the squeeze-film damping constant c_n depended on the driving amplitude. This can be seen in 4.5d, where we plot the nonlinear squeeze-film damping ratio $\zeta_n = \frac{c_n}{2\sqrt{k_{m1}\,m}}$ versus normalized drive amplitude. When the driving force is small and the plate is in linear regime, the theoretical Q factor is $Q = 1/(2\zeta_e + 2\zeta_n) = 29.6$, which is close to the linear $Q = 24.8$. With increasing driving force, the normalized damping ratio increases from 0.01 to 0.03, deviating from the theoretical value more with increasing amplitude, indicating that more sophisticated damping models will be needed to fully capture the nonlinear dynamic air damping of levitating plates.

4.3. CONCLUSIONS

In conclusion, we have explored the nonlinear dynamics of diamagnetically levitating graphite plates. Using gravitational force, we characterized the nonlinearity of the magnetic force field in which the plate is trapped. With dynamic measurements, we observe that the intrinsic nonlinearity of the repulsive magnetic force causes a spring softening nonlinearity that leads to lower peak amplitude for increasing driving. Due to asymmetries in the magnetic potential, it is found that a quintic polynomial is needed to describe the force-displacement function with sufficient accuracy. Thus good agreement between experimental and simulated nonlinear dynamic frequency response is obtained in vacuum. Finally, we compare the normalized frequency response of the plate in air at atmospheric conditions, concluding that the eddy current damping is nearly linear and the squeeze film effect leads to strong nonlinear damping. This study of the nonlinear dynamics of levitating systems provides insight into the effects of the nonlinear stiffness of a magnetic trap and squeeze film damping forces on the nonlinear dynamics of levitating plates in the presence of base excitation. Moreover, it demonstrates an approach for analyzing the nonlinear dynamics of other levitating systems that will likely become of increasing relevance considering the growing interest in the field of levitodynamics.

4.4. APPENDIX

A1. MAGNETIC FIELD CALCULATION BY ANALYTICAL MODELING

In this section, we determine the magnetic field **B** outside a rectangular permanent magnet using the charge model following the derivation in reference [19]. We first introduce the charge model of determining the magnetic field of a unit magnet source, and then expand it to one rectangular permanent magnet.

THE CHARGE MODEL

The charge model is a useful method to calculate the magnetic field distribution of permanent magnets. In this model, a magnet is taken as a distribution of equivalent 'magnetic charge', which is the source of magnetic field. For a current-free region and magnetostatic field, $\nabla \times \mathbf{H} = 0$ and $\nabla \cdot \mathbf{B} = 0$, where $\mathbf{H}, \mathbf{B}$ are the magnetic field strength and magnetic flux density due to a magnetic source, respectively. Then, the irrotational magnetic vector field $\mathbf{H}$ can be written as the gradient of the magnetic scalar potential ϕ_m:

$$\mathbf{H} = -\nabla \phi_m. \tag{4.7}$$

Because $\mathbf{B} = \mu_0(\mathbf{H}+\mathbf{M})$, where μ_0 is the vacuum permeability and $\mathbf{M}$ is the magnetization, combining Eq. (4.7) and $\nabla \cdot \mathbf{B} = 0$ results in:

$$\nabla^2 \phi_m = \nabla \cdot \mathbf{M}. \tag{4.8}$$

For a free space without boundary conditions, we can solve Eq. (4.8) using Green's function $G(\mathbf{x},\mathbf{x_0})$ for ∇^2 and obtain a particular solution:

$$\phi_{\mathrm{m}}(\mathbf{x}) = \int G(\mathbf{x},\mathbf{x_0})\nabla'\cdot\mathbf{M}(\mathbf{x_0})\mathrm{d}v_0 \tag{4.9}$$

$$= -\frac{1}{4\pi}\int \frac{\nabla'\cdot\mathbf{M}(\mathbf{x_0})}{|\mathbf{x}-\mathbf{x_0}|}\mathrm{d}v_0, \tag{4.10}$$

where $\mathbf{x}$ is the observation point, $\mathbf{x_0}$ is the source point, ∇' operates on the primed coordinates, and the integration is over the volume for which the magnetization exists. Assuming $\mathbf{M}$ is confined in a volume V with boundary surface S and falls abruptly to zero outside of this volume, Eq. (4.10) can be written as:

$$\phi_{\mathrm{m}}(\mathbf{x}) = -\frac{1}{4\pi}\int_V \frac{\nabla'\cdot\mathbf{M}(\mathbf{x_0})}{|\mathbf{x}-\mathbf{x_0}|}\mathrm{d}v_0 + \frac{1}{4\pi}\oint_S \frac{\mathbf{M}(\mathbf{x_0})\times\hat{\mathbf{n}}}{|\mathbf{x}-\mathbf{x_0}|}\mathrm{d}s_0, \tag{4.11}$$

where $\hat{\mathbf{n}}$ is the outward unit normal to S. Therefore, the volume charge densities ρ_{m} and surface charge densities σ_{m} can be defined as:

$$\rho_{\mathrm{m}} = -\nabla\cdot\mathbf{M} \tag{4.12}$$

$$\sigma_{\mathrm{m}} = \mathbf{M}\cdot\hat{\mathbf{n}}. \tag{4.13}$$

For free space, $\mathbf{B} = \mu_0\mathbf{H}$, and subtituting Eq. (4.11) into Eq. (4.7) obtains:

$$\mathbf{B}(\mathbf{x}) = \frac{\mu_0}{4\pi}\int_V \frac{\rho_{\mathrm{m}}(\mathbf{x_0})(\mathbf{x}-\mathbf{x_0})}{|\mathbf{x}-\mathbf{x_0}|^3}\mathrm{d}v_0 + \frac{\mu_0}{4\pi}\oint_S \frac{\sigma_{\mathrm{m}}(\mathbf{x_0})(\mathbf{x}-\mathbf{x_0})}{|\mathbf{x}-\mathbf{x_0}|^3}\mathrm{d}s_0, \tag{4.14}$$

MAGNETIC FIELD OF ONE PERMANENT MAGNET

For a permanent magnet as shown in Fig. 4.6, assuming that its magnetization is $\mathbf{M} = M_{\mathrm{r}}\hat{z}$ along z direction and its dimension can be denoted by two points P1(x_1, y_1, z_2) and

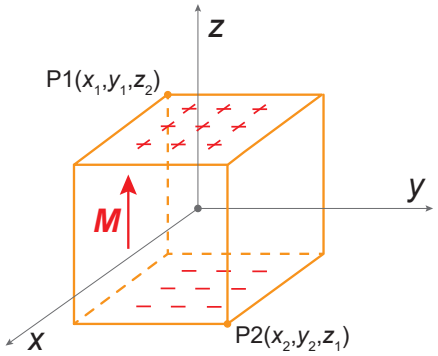

Figure 4.6: Schematic of one permanent magnet with magnetization $\mathbf{M}$ and its corresponding coordinate system. The charge densities on the top and bottom surfaces of the magnet are represented with + and -, respectively.

P2(x_2, y_2, z_1), its magnetic field $\mathbf{B}$ can be calculated using the charge model. For permanent magnets, the volume charge density inside the magnets is zero $\rho_m = -\nabla \cdot \mathbf{M} = 0$, while the surface charge densities on top and bottom surfaces are:

$$\sigma_m = \begin{cases} M_r & (z = z_2) \\ -M_r & (z = z_1). \end{cases} \tag{4.15}$$

Based on Eq. (4.14), the magnetic field of the rectangular magnet is:

$$\mathbf{B}(x,y,z) = \frac{\mu_0 M_r}{4\pi} \sum_{k=1}^{2} (-1)^k \times \int_{y_1}^{y_2} \int_{x_1}^{x_2} \frac{[(x-x_0)\hat{\mathbf{x}} + (y-y_0)\hat{\mathbf{y}} + (z-z_k)\hat{\mathbf{z}}]\mathrm{d}x_0\mathrm{d}y_0}{[(x-x_0)^2 + (y-y_0)^2 + (z-z_k)^2]^{3/2}}. \tag{4.16}$$

Therefore, by integrating Eq. (4.16) with respect to x_0 and y_0, we can obtain the x-component of the magnetic field:

$$B_x(x,y,z) = \frac{\mu_0 M_r}{4\pi} \sum_{k=1}^{2} \sum_{m=1}^{2} (-1)^{k+m} \ln[\frac{(y-y_1) + [(x-x_m)^2 + (y-y_1)^2 + (z-z_k)^2]^{1/2}}{(y-y_2) + [(x-x_m)^2 + (y-y_2)^2 + (z-z_k)^2]^{1/2}}], \tag{4.17}$$

and the y-component of the magnetic field:

$$B_y(x,y,z) = \frac{\mu_0 M_r}{4\pi} \sum_{k=1}^{2} \sum_{m=1}^{2} (-1)^{k+m} \ln[\frac{(x-x_1) + [(x-x_1)^2 + (y-y_m)^2 + (z-z_k)^2]^{1/2}}{(x-x_2) + [(x-x_2)^2 + (y-y_m)^2 + (z-z_k)^2]^{1/2}}]. \tag{4.18}$$

Similarly, the z-component of the magnetic field can be obtained:

$$B_z(x,y,z) = \frac{\mu_0 M_r}{4\pi} \sum_{k=1}^{2} \sum_{n=1}^{2} \sum_{m=1}^{2} (-1)^{k+n+m} \tag{4.19}$$

$$\times \tan^{-1}[\frac{(x-x_n)(y-y_m)}{z-z_k} \frac{1}{[(x-x_n)^2 + (y-y_m)^2 + (z-z_k)^2]^{1/2}}]. \tag{4.20}$$

Normally, the magnetic property of a permanent magnet is described by its remanent magnetic flux density B_r, and $B_r = \mu_0 M_r$. Therefore, with a known B_r and demensions, the magnetic field outside a permanent magnet can be calculated using Eq. (4.17), Eq. (4.18) and Eq. (4.19). For example, for a magnet with $B_r = 1.4\,\mathrm{T}$ and dimensions of $10 \times 10 \times 10\,\mathrm{mm}^3$ ($x_1 = -5, x_2 = 5, y_1 = -5, y_2 = 5, z_1 = -5, z_2 = 5$), its magnetic field B_x, B_y, B_z along a line ($x = 2\,\mathrm{mm}, y = 3\,\mathrm{mm}, 5\,\mathrm{mm} < z < 10\,\mathrm{mm}$) are calculated using Eq. (4.17-4.19) and shown in Fig. 4.7. For comparison, we also use a finite element method (COMSOL Multiphysics) to calculate the magnetic field of the same magnet and the results are also shown in Fig. 4.7, from which a good agreement between the two methods is observed.

MAGNETIC FIELD OF AN ARRAY OF MAGNETS

For an array of multiple permanent magnets, the magnetic field in free space can also be determined using Eq. (4.17-4.19). For example, for a magnet array as shown in Fig. 4.8, it magnetic field can be calculated by:

$$\mathbf{B}(x,y,z) = \sum_{i=1}^{4} \mathbf{B}_i(x,y,z), \tag{4.21}$$

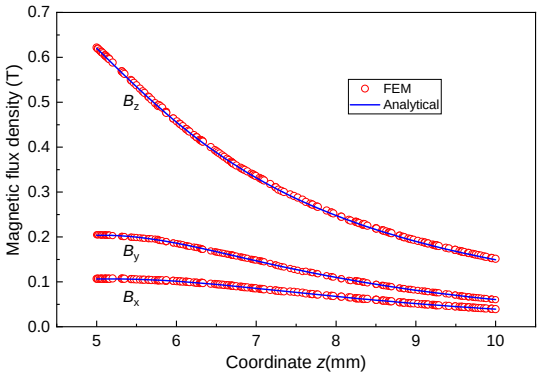

Figure 4.7: Schematic of one magnet with magnetization **M** and its corresponding coordinate system.

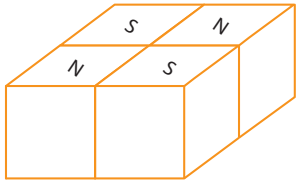

Figure 4.8: An array of four permanent magnets with alternating magnetic poles, where 'N' represents the north pole and 'S' the south pole, respectively.

where $\mathbf{B}_i(x, y, z)$ is the magnetic filed of the $i-$th magnet.

After the magnetic field is determined, the magnetic force applied on the graphite plate can be calculated with:

$$\begin{aligned}\mathbf{F_B} &= \nabla \int_{\mathcal{V}} \mathbf{M} \cdot \mathbf{B} \mathrm{d}\mathcal{V} \\ &= \frac{\mu_0}{2} \int_{\mathcal{V}} \nabla(\chi_x H_x^2 + \chi_y H_y^2 + \chi_z H_z^2) \mathrm{d}\mathcal{V},\end{aligned} \tag{4.22}$$

where $\mathcal{V}$ is the volume of the plate, $H_{x,y,z}$ are the components of the magnetic field vector, **M** is the magnetization vector and **B** the magnetic flux density vector. In this analysis it is assumed that the plate does not significantly affect the magnetic field, since its relative magnetic permeability is close to 1. All the parameters used in our calculations for pyrolytic graphite plates are listed in Table 4.2.

A2. MAGNETIC FIELD CALCULATION BY FEM MODELING

In order to compare with the analytical modeling and take into account the fillets on the edges of the magnets, we also use FEM method to calculate the magnetic force. The geometry model of the magnets and graphite plate is shown in Fig. 4.9. The magnets are with dimensions of $12 \times 12 \times 12\,\mathrm{mm}^3$ and with rounded edges with a fillet radius of 1 mm. The remanent magnetic flux density of the magnets is $B_\mathrm{r} = 1.4\,\mathrm{T}$. The material

Table 4.2: Material properties used for the simulations of the levitating pyrolytic graphite.

Property	Symbol	Value	Unit
Density	ρ	2070	kg/m^3
Susceptibility $\perp$ [26]	χ_z	-450	$\times 10^{-6}$
Susceptibility $\parallel$ [26]	$\chi_{x,y}$	-85	$\times 10^{-6}$

properties of the $10 \times 10 \times 0.28\,\text{mm}^3$ graphite plate are listed in Table 4.2. Using *COMSOL Multiphysics 5.6*, we can simulate the magnetic field and then calculate the magnetic force using Eq. (4.22).

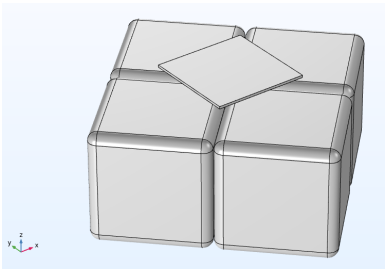

Figure 4.9: Geometry model of one graphite plate levitating over four permanent magnets.

A3. CHARACTERIZATION OF SHAKER

To determine the relations between the output motion and driving voltage of the shaker, we shine the laser directly on the magnets and measure their displacement amplitude a with different driving voltages V_{ac}. The measurement results for 4 different driving frequencies are shown in Fig. 4.10. It can be seen that the displacement of the shaker is approximately liner with the driving voltage and $a = 0.0158 V_{\text{ac}}$.

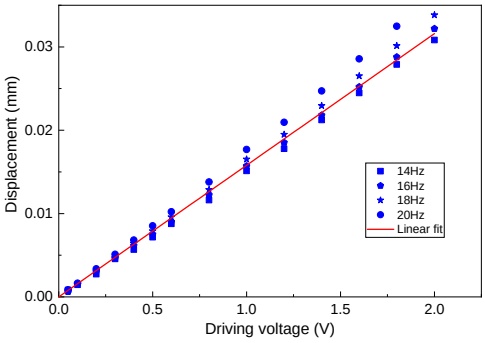

Figure 4.10: Displacement amplitude of the shaker as a function of driving voltages for four driving frequencies.

A4. LINEAR RESONANCE FREQUENCIES IN THE FITTING OF FIG. 4.5C

Table 4.3 lists the Linear resonance frequencies used for the frequency response curve fitting in Fig. 4.5c.

Table 4.3: Linear resonance frequencies used for the frequency response curve fitting in Fig. 4.5c

Driving voltage (V)	0.1	0.5	1	3	4	5
Resonance frequency (Hz)	16.78	16.80	16.82	16.86	16.89	16.92

REFERENCES

[1] C. Gonzalez-Ballestero, M. Aspelmeyer, L. Novotny, R. Quidant, and O. Romero-Isart, "Levitodynamics: levitation and control of microscopic objects in vacuum", Science **374**, eabg3027 (2021).

[2] U. Delić, M. Reisenbauer, K. Dare, D. Grass, V. Vuletić, N. Kiesel, and M. Aspelmeyer, "Cooling of a levitated nanoparticle to the motional quantum ground state", Science **367**, 892–895 (2020).

[3] L. Magrini, P. Rosenzweig, C. Bach, A. Deutschmann-Olek, S. G. Hofer, S. Hong, N. Kiesel, A. Kugi, and M. Aspelmeyer, "Real-time optimal quantum control of mechanical motion at room temperature", Nature **595**, 373–377 (2021).

[4] J. Millen, T. Deesuwan, P. Barker, and J. Anders, "Nanoscale temperature measurements using non-equilibrium brownian dynamics of a levitated nanosphere", Nature nanotechnology **9**, 425–429 (2014).

[5] C. W. Lewandowski, T. D. Knowles, Z. B. Etienne, and B. D'Urso, "High-sensitivity accelerometry with a feedback-cooled magnetically levitated microsphere", Physical Review Applied **15**, 014050 (2021).

[6] G. Ranjit, M. Cunningham, K. Casey, and A. A. Geraci, "Zeptonewton force sensing with nanospheres in an optical lattice", Physical Review A **93**, 053801 (2016).

[7] X. Chen, A. Keşkekler, F. Alijani, and P. G. Steeneken, "Rigid body dynamics of diamagnetically levitating graphite resonators", Applied Physics Letters **116**, 243505 (2020).

[8] F. Xiong, P. Yin, T. Wu, H. Xie, R. Li, Y. Leng, Y. Li, C. Duan, X. Kong, P. Huang, et al., "Lens-free optical detection of thermal motion of a submillimeter sphere diamagnetically levitated in high vacuum", Physical Review Applied **16**, L011003 (2021).

[9] E. Brandt, "Levitation in physics", Science **243**, 349–355 (1989).

[10] V. Jain, J. Gieseler, C. Moritz, C. Dellago, R. Quidant, and L. Novotny, "Direct measurement of photon recoil from a levitated nanoparticle", Physical review letters **116**, 243601 (2016).

[11] N. Bullier, A. Pontin, and P. Barker, "Characterisation of a charged particle levitated nano-oscillator", Journal of Physics D: Applied Physics **53**, 175302 (2020).

[12]C. Timberlake, G. Gasbarri, A. Vinante, A. Setter, and H. Ulbricht, "Acceleration sensing with magnetically levitated oscillators above a superconductor", Applied Physics Letters **115**, 224101 (2019).

[13]R. Middlemiss, A. Samarelli, D. Paul, J. Hough, S. Rowan, and G. Hammond, "Measurement of the earth tides with a mems gravimeter", Nature **531**, 614–617 (2016).

[14]J. Schmöle, M. Dragosits, H. Hepach, and M. Aspelmeyer, "A micromechanical proof-of-principle experiment for measuring the gravitational force of milligram masses", Classical and Quantum Gravity **33**, 125031 (2016).

[15]Y. Leng, R. Li, X. Kong, H. Xie, D. Zheng, P. Yin, F. Xiong, T. Wu, C.-K. Duan, Y. Du, et al., "Mechanical dissipation below 1 μ hz with a cryogenic diamagnetic levitated microoscillator", Physical Review Applied **15**, 024061 (2021).

[16]J. Gieseler, L. Novotny, and R. Quidant, "Thermal nonlinearities in a nanomechanical oscillator", Nature physics **9**, 806–810 (2013).

[17]L. Villanueva, E. Kenig, R. Karabalin, M. Matheny, R. Lifshitz, M. Cross, and M. Roukes, "Surpassing fundamental limits of oscillators using nonlinear resonators", Physical review letters **110**, 177208 (2013).

[18]C. Zhao, G. Sobreviela, M. Pandit, S. Du, X. Zou, and A. Seshia, "Experimental observation of noise reduction in weakly coupled nonlinear mems resonators", Journal of Microelectromechanical Systems **26**, 1196–1203 (2017).

[19]E. P. Furlani, *Permanent magnet and electromechanical devices: materials, analysis, and applications* (Academic press, 2001).

[20]J. S. Ochs, G. Rastelli, M. Seitner, M. I. Dykman, and E. M. Weig, "Resonant nonlinear response of a nanomechanical system with broken symmetry", Physical Review B **104**, 155434 (2021).

[21]A. Keşkekler, H. Arjmandi-Tash, P. G. Steeneken, and F. Alijani, "Symmetry-breaking-induced frequency combs in graphene resonators", Nano letters **22**, 6048–6054 (2022).

[22]E. J. Doedel, A. R. Champneys, T. F. Fairgrieve, Y. A. Kuznetsov, B. Sandstede, X. Wang, et al., "Auto97", Continuation and bifurcation software for ordinary differential equations (1998).

[23]M. Bao and H. Yang, "Squeeze film air damping in mems", Sensors and Actuators A: Physical **136**, 3–27 (2007).

[24]M. H. Sadd and A. K. Stiffler, "Squeeze film dampers: amplitude effects at low squeeze numbers", Journal of Engineering for Industry **97**, 1366–1370 (1975).

[25]T. Veijola, A. Pursula, and P. Råback, "Extending the validity of squeezed-film damper models with elongations of surface dimensions", Journal of Micromechanics and Microengineering **15**, 1624 (2005).

[26]M. Simon and A. Geim, "Diamagnetic levitation: flying frogs and floating magnets", Journal of applied physics **87**, 6200–6204 (2000).

5

DIAMAGNETICALLY LEVITATING RESONANT WEIGHING SCALE

Diamagnetic levitation offers stable confinement of an object from its environment at zero power, and thus is a promising technique for developing next generation unclamped resonant sensors. In this work, we realize a resonant weighing scale using a graphite plate that is diamagnetically levitating over a checkerboard arrangement of permanent magnets. We characterize the bending vibrations of the levitating object using laser Doppler vibrometry and use microgram glass beads to calibrate the responsivity of the sensor's resonance frequency to mass changes. The sensor is used for real-time measurement of the evaporation rate of nano-litre droplets with high-accuracy. By analyzing the resonator's frequency stability, we show that the millimeter graphite sensor can reach mass resolutions down to 4.0 ng*, relevant to biological and chemical sensing concepts.*

Parts of this chapter have been published in Sensors and Actuators A: Physical **330**, 112842 (2021) [1]

5.1. INTRODUCTION

Mechanical resonators are nowadays being adopted in billions of products, including quartz crystals, Micro-Electro-Mechanical Systems (MEMS), and acoustic wave resonators for time-keeping, frequency referencing and electronic filtering, but also for addressing a wide range of sensor applications in modern technology. These resonant sensors can be used to measure parameters like mass [2–4], stiffness [5], density [6], viscosity [7], and pressure [8], for a diverse range of applications, ranging from environmental monitoring to life sciences [9–11]. The working principle of these devices is based on tracking a resonance frequency f_r of the sensor that depends on the sensing parameter. In this framework, the minimum resonance frequency change that can be detected by the sensor, its limit of detection, depends both on its responsivity and on the uncertainty σ_a in the resonance frequency measurement. For low uncertainty or low operation power, a high mechanical quality factor Q of the resonance is beneficial. However, Q can be substantially degraded through clamping, friction, adhesion and aerodynamic losses [12].

In literature great efforts have been undertaken to reduce these dissipation mechanisms in resonant sensors. For instance, optimizing clamping points by high tension tethers [13], or using bulk acoustic modes [7], acoustic Bragg mirrors [14], and phononic crystals [15], have been used for boosting Q of resonant sensors and isolating them from their environment. Ultimate confinement of a sensor though can be obtained by levitating it, which therefore has the potential to significantly improve Q of resonant sensors.

Levitation of objects can be realized in different ways, using optics, acoustics, or magnetic forces [16]. Among them, diamagnetic levitation stands out as the only method that obtains stable levitation at room temperature without power consumption [17]. Such passive levitation is important in many practical, high-volume microscale applications, not only because it is difficult to guarantee a continuous power supply for levitation, but also because collapse of a levitating microstructure in the absence of power leads to failure by adhesion. Additionally, unlike optical levitation [18], passive levitation does not dissipate power that can heat the levitating object. Interestingly, many materials are diamagnetic, exhibiting negative magnetic susceptibility [19], thus making diamagnetic levitation potentially a widely applicable method, especially at the microscale where larger magnetic field gradients can be achieved such that also weakly diamagnetic materials can be levitated. During the last decade, liquid droplets [20] and small solid particles [21] have been levitated stably by micro magnets. In addition, diamagnetic levitation has shown the potential for realizing accelerometers [22], energy harvesters [23], density [24], and force sensors [25].

In this paper, we propose a resonant mass sensor based on diamagnetic levitation. The sensor comprises a pyrolytic graphite plate that is passively levitating over a checkerboard arrangement of permanent magnets. Compared to conventional clamped resonant mass sensors, the levitating sensor offers contactless and free motion of the resonator in the absence of clamping and friction forces, potentially leading to higher Q and thus more sensitive sensor design. We characterize the first 10 bending modes of the levitating plate in the kHz regime using a Polytec laser Doppler vibrometer (LDV), and calibrate its mass responsivity using glass microbeads. With the calibrated plate we measure the mass evaporation rate of small liquid droplets on the plate, which is found

to be in good agreement with estimates made using the droplet volume. Finally, we characterize the Allan deviation of the resonance frequency σ_a and use it to show that the mass resolution of the weighing scale is as low as a few nano-grams (ng).

5.2. MASS SENSING WORKING PRINCIPLE

The working principle of a resonant mass sensor is based on the frequency shift δf of the resonant mode when a mass δm is attached to the resonator. The dynamics of the bare plate can be described by an effective stiffness K_{eff} and an effective mass $M_{\text{eff,plate}}$. When a small mass δm is placed at the anti-node, the effective mass becomes $M_{\text{eff}} = M_{\text{eff,plate}} + \delta m$, and the resonance frequency can be written as $f_{\text{r}} = \frac{1}{2\pi}\sqrt{\frac{K_{\text{eff}}}{M_{\text{eff}}}}$. Assuming that the added mass does not influence K_{eff} and the quality factor Q of the resonator, the following relation between δf and δm can be obtained by differentiating the resonance frequency f_{r} with respect to δm:

$$\delta m = -\frac{1}{\mathscr{R}}\delta f, \tag{5.1}$$

in which $\mathscr{R} = \frac{f_{\text{r}}}{2M_{\text{eff,plate}}}$ is the mass responsivity of the resonator.

From Eq. (5.1), it can be shown that the sensitivity of a resonant sensor is determined by the mass responsivity $\mathscr{R}$ and the minimum detectable frequency shift δf. It is known that $\mathscr{R}$ is determined by the structure and material properties of the resonator, while the minimum detectable frequency change is determined by the short- and long-term resonance frequency stability of the device that can be evaluated by the Q factor and amplitude of oscillation [26]. It is also worth noting that in the presence of adsorbates, the resonance frequency shift δf is a convolution of both the stiffness and the mass. However, the stiffness effect comes into play at regions where the resonator undergoes high changes of curvature, close to the nodal lines [27, 28]. Therefore, by placing an added adsorbate or particle close to an anti-node, this effect can be minimized.

5.3. EXPERIMENTS

Experiments are performed on levitating pyrolytic graphite plates, which are used to measure the mass of glass beads or liquid droplets that are placed on their surface (Fig. 4.1a). The graphite is purchased from MTI Corporation and is cut using a micro laser cutter to obtain $10 \times 10 \times 0.24$ mm^3 plates. The surface of the plate is polished using a sand paper with 5 μm grain to improve the reflected optical readout signal. In order to levitate the plates, a checkerboard arrangement of 4 cubic permanent NdFeB magnets with alternating out-of-plane magnetization is used (Fig. 4.1b). The remanent magnetic flux density of the magnets is $B_r = 1.4$ T.

To determine the frequency response of the graphite plate, we use an experimental setup that comprises a Polytec MSA-400 laser Doppler vibrometer (LDV) to measure the out-of-plane velocity of the plate and a Zurich UHFLI lock-in amplifier to drive the levitating plate into resonance through a dedicated electromagnetic coil (Fig. 4.1c) that is surrounding the permanent magnets. The current through the coil generates an alternating magnetic field in the vertical direction that actuates the permanent magnets. The motion of the magnets modulates the magnetic field on the plate and brings it into res-

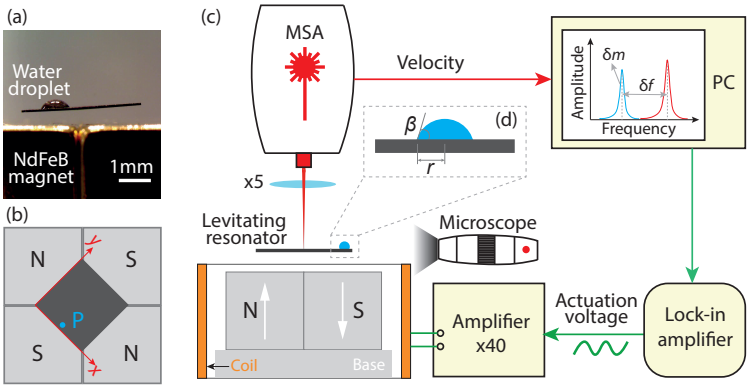

Figure 5.1: Levitating resonator and experimental setup. (a) Levitating pyrolytic graphite plate above 4 NdFeB magnets with alternating magnetization. A water droplet is dispensed on top of the graphite plate; (b) Top view of the levitating plate (not to scale) shows the position (point P) of the droplet, where N and S stand for north and south pole of the magnet, respectively; (c) Schematic of the sensing principle and the measurement setup comprising a Polytec LDV, an electromagnetic excitation coil, a lock-in amplifier for actuation and readout and, a USB microscope to measure the dimensions of the droplet. The actuation voltage is amplified by a 40× voltage amplifier that drives the levitating plate into resonance via a coil; (d) Schematic of a sessile liquid droplet as captured by the in-plane microscope on the surface of the graphite plate (not to scale), where β is the contact angle and r is the contact radius.

onance. Although there is also a direct electromagnetic force on the plate from the coil, this force is estimated to be significantly smaller than the forces generated by the motion of the permanent magnets. To detect the velocity of the resonator, the LDV laser beam is focused on the plate surface and the vibrometer signal obtained by the MSA laser head is analyzed using the Polytec decoder. Next, the acquired velocity is transferred to the Polytec PSV software for frequency response analysis and obtaining the resonance frequencies and Q factor, or the lock-in amplifier for evaluating the frequency stability in closed loop. To accurately measure the dimensions of the droplet, an in-plane oriented microscope is also used in our setup (Fig. 4.1a,d). The microscope is used to trace the variations in the contact angle β and contact radius r of the liquid droplet throughout evaporation. All our experiments are conducted at atmospheric conditions and at room temperature.

5.4. RESULTS AND DISCUSSION

5.4.1. DYNAMIC CHARACTERIZATION

To characterize the resonant response of the levitating plate, we place the bare plate on the magnets and excite the plate with a periodic chirp signal over a large frequency range. Once we identify a resonance peak, we perform a narrow-band frequency sweep around the resonance frequency while positioning the laser on the anti-node (point of maximum amplitude) of the excited mode. The outcome of this procedure is shown in Fig. 5.2 where the first 10 resonance modes of the levitating plate are found. In Fig. 5.2, for each resonance peak a schematic of the corresponding mode shape as determined by the LDV is also shown. To extract the quality factor associated with the modes, we fit

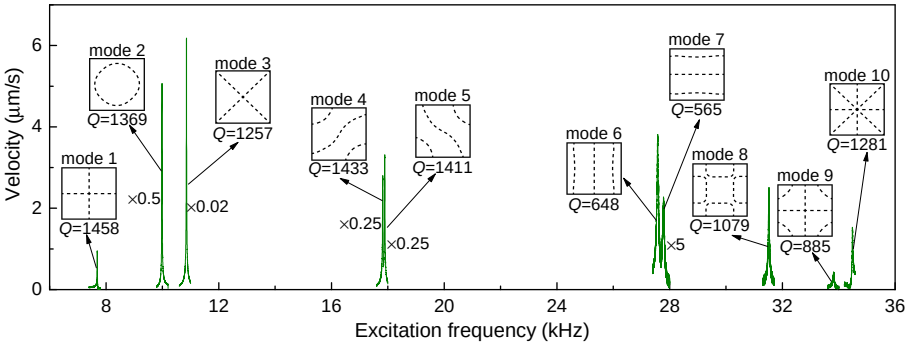

Figure 5.2: Experimental resonance peaks, Q-factors and mode shapes, as experimentally determined by the LDV, of 10 bending modes of the graphite plate with dimensions of $10 \times 10 \times 0.24$ mm, levitating above 4 cubic NdFeB magnets with side length of 12 mm. The dashed lines indicate the nodal lines of the measured modes. Peaks have been rescaled by the indicated factors, and Q factors determined by fits. In particular mode 3 has a high amplitude, which is attributed to its efficient actuation by the magnet configuration (Fig. 4.1b).

5

a Lorentzian to each resonance peak and obtain $Q \approx 1500$ for the first five modes of vibration in air, which is much higher than the Q of the levitating plate's rigid body modes [17]. It is noted that the Q of the resonator is a result of three main energy dissipation sources: material damping, air damping and eddy current damping. The relatively high Qs observed in air make our graphite resonator an interesting candidate for mass sensing applications, where high Qs are beneficial for improving detection limits [26].

5.4.2. MASS RESPONSIVITY OF THE RESONATOR

To calibrate the responsivity of the resonant mass sensor, small glass beads with mass δm are placed on the graphite plate. This causes a change in the resonance frequency δf associated with a bending mode. We choose to perform our mass measurements using the 3^{rd} bending mode since it has the highest amplitude of all modes of vibration (see Fig. 5.2), i.e., this mode has the highest signal-to-noise ratio. We attribute the high amplitude of the third mode mainly to the high efficiency actuation due to the resemblance of the mode shape (Fig. 5.2) to the magnet configuration(see Fig. 4.1b), while noting that the direction of the force of the coil on the magnets depends on their respective magnetization direction.

Eq. (5.1) states that in order to obtain the added mass δm, it is essential to first determine the responsivity of the sensor. Here, we use glass beads of diameter 250 μm with known density to obtain the experimental mass responsivity $\mathscr{R}_{\text{exp}}$. The glass beads are placed using water droplets created by syringe near the anti-node of the 3^{rd} bending mode (point P: $x = 5$ mm, $y = 1$ mm in Fig. 5.3c and Fig. 4.1b). To add the glass beads, the graphite plate is removed from the experimental setup, and is then placed back to measure the resonance frequency in the presence of added particles. We note that since the levitation system does not require any clamping, no calibration is required every time the resonator is placed back on top of the magnets. The frequency shift of the resonator after adding different numbers of glass beads is plotted in Fig. 5.3a. A linear relationship is apparent between the added mass and the frequency shift, with a slope

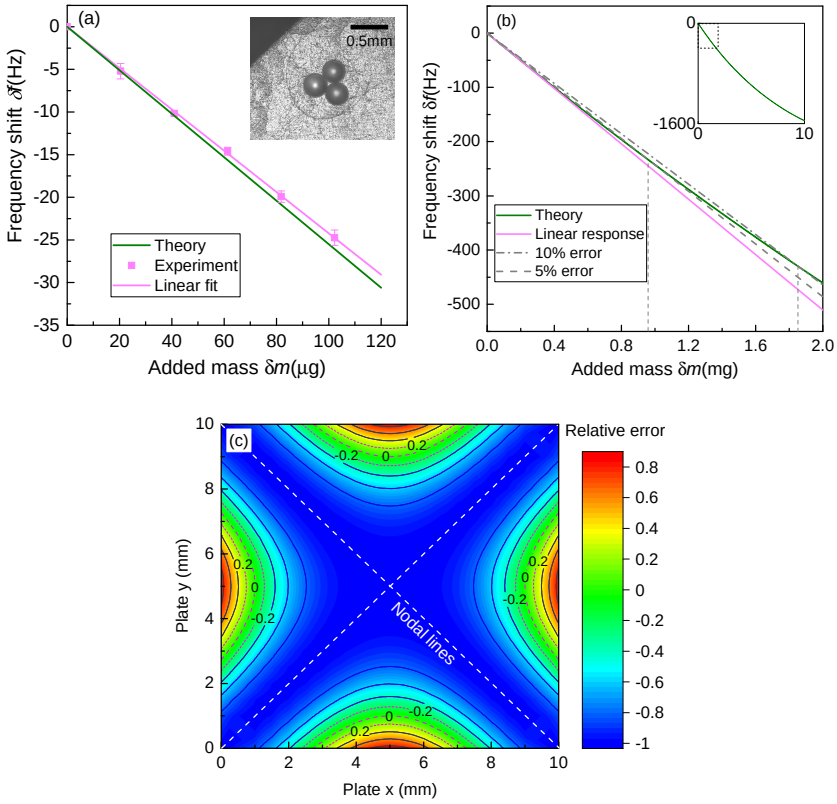

Figure 5.3: Mass responsivity and error analysis. (a) Frequency shift as a function of the mass of the added glass beads, as obtained from experiments and as estimated using Rayleigh-Ritz method. The inset shows an image of three glass beads on top of the levitating plate, taken with a microscope; (b) Frequency shift as a function of the added mass obtained numerically, showing a linear relationship between the frequency shift and added mass; (c) Relative error ($\frac{\delta m_P - \delta m}{\delta m}$), where δm is the actual added mass and δm_P is the mass calculated from Eq. (5.1) using the mass responsivity of point P ($\mathscr{R}_P$).

of $-0.24\,\mathrm{Hz}/\mu\mathrm{g}$ that is the experimental mass responsivity $\mathscr{R}_{\mathrm{exp}}$ of our resonator, from which $M_{\mathrm{eff,exp}} = 2.24 \times 10^{-5}\,\mathrm{kg}$.

In order to evaluate the accuracy of our measurements, we construct a numerical model of the levitating plate using the Rayleigh-Ritz method [29, 30] and calculate the resonance frequency shifts of the plate with added mass (details of the numerical modelling can be found in Appendix A1). Using the numerical model, we determine the frequency shift δf as a function of add mass δm which is placed on point P. Our numerical results are also included in Fig. 5.3a obtaining a theoretical mass responsivity $\mathscr{R}_{\mathrm{th}} = -0.25\,\mathrm{Hz}/\mu\mathrm{g}$ in good agreement with the experimental value. Using the numerical model, we can estimate the range of δm over which the shift in the resonance frequency δf varies linearly with the added mass. For this, we perform simulations over a large number of added mass increments and find that when the added mass is below 0.96 mg,

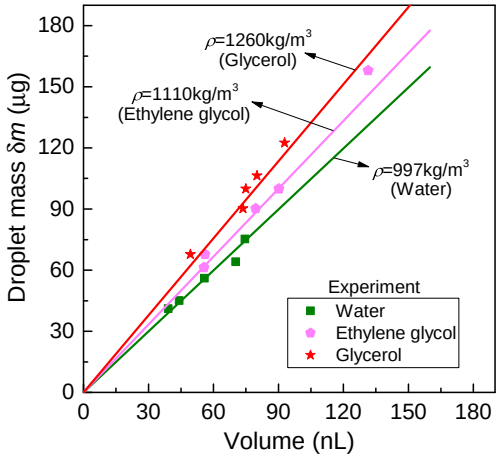

Figure 5.4: Plot of the estimated droplet mass from the change in the resonance frequency of the graphite plate, versus droplet volume determined from the microscope image for droplets of water, ethylene glycol and glycerol placed near the antinode position P.

the relative error between the real and the estimated mass using Eq. (5.1) is less than 5 % (see Fig.5.3b). This result suggests that we can use Eq. (5.1) with confidence to measure mass changes smaller than 1 mg. We note that this value is much smaller than the bearing capacity of the levitating plate which is estimated to be 227 mg (4 times the plate's mass).

In addition, when using bending vibrations for mass sensing, the position where the mass is placed on the resonator can influence the accuracy of the mass responsivity [27]. To investigate how the position of the added mass affects the accuracy of our measurements, we use the same model to estimate the frequency shift associated with a certain mass (10 μg) added at different locations on the plate. The result of this numerical study is shown in Fig. 5.3c, and highlights the error that can be induced in determining δm, if the added mass is placed on different locations. The relative error can be expressed as $\frac{\delta m_P - \delta m}{\delta m}$, where δm is the actual mass of the particle and δm_P is the mass determined from Eq. (5.1) using the mass responsivity of point P ($\mathscr{R}_P$). It could be seen that putting the point mass 0.3 mm away from point P ($x = 5$ mm, $y = 0.7$ mm) results in an error of 20 %, indicating that the sensor is pretty sensitive to the placement. Also, this error grows when placing the added mass further away from P and closer to the nodal lines. Therefore, the choice of vibration mode to be used for sensing, depends on the number and distribution of nodal lines associated with that mode. Among the identified mode shapes shown in Fig. 5.2, the first three bending modes have the lowest number of nodal lines while exhibiting a decent Q. Therefore, they are ideal resonances for investigating the mass sensing concept, especially for droplets which require a certain amount of contact area.

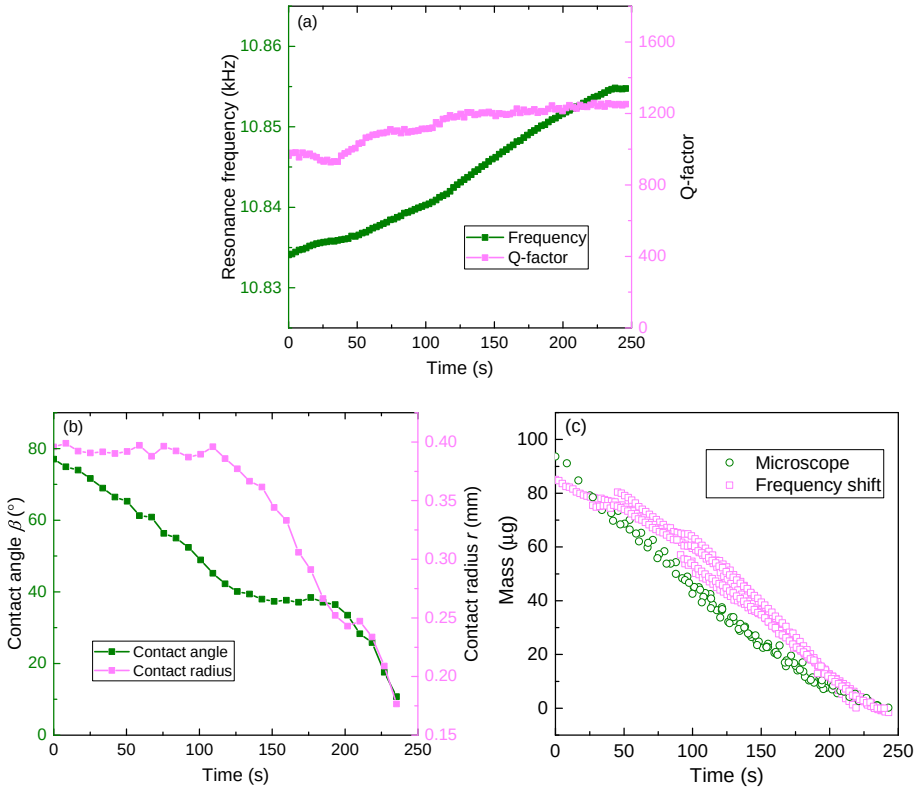

Figure 5.5: Measuring evaporation rate of water droplets. (a) Resonance frequency (green) and Q-factor (pink) as a function of time while the water droplet is evaporating, measured using the setup shown in Fig. 5.1c; (b) Contact angle (green) and contact radius (pink) measurements during evaporation; (c) Measured mass of 4 water droplets with different initial volume as a function of time, obtained using both the in-situ microscope (green) and frequency shift method (pink).

5.4.3. MEASURING LIQUID DENSITY AND EVAPORATION RATE

Measuring the mass and density of liquid droplets has many applications in bio/chemical technologies [9, 31–33]. Here, we measure the density of different liquids and evaporation rate (mass change over time) of nL volume droplets using our calibrated levitating graphite plate. To measure liquid density, we first dispense droplets of different liquids and volume using a syringe near the anti-node of the resonator (point P in Fig. 5.1b) and detect the frequency shift due to the added mass. Next, using the experimental mass responsivity $\mathscr{R}_{\text{exp}}$ determined in Section 5.4.2, we estimate δm associated with the dispensed droplets. At the same time, using an in-situ microscope and an image processing code implemented in Matlab (details given in Appendix A2), we measure the volume of the droplets by estimating their contact radius r and contact angle β (Fig. 5.1d). In Fig. 5.4 we report the mass of droplets of water, ethylene glycol, and glycerol of different volumes, measured using our resonator. It can be observed that the measured values follow the theoretical curves for known densities of these liquids.

To investigate the applicability of our levitating resonator for real-time sensing, we next use the resonant levitating mass sensor for detecting the evaporation rate of water droplets using resonance frequency shifts. We dispense droplets of different volumes, and estimate evaporation rate as $\dot{m} = \delta m/\delta t$, where δm is the mass change over time δt as evaluated using Eq. (5.1). Fig. 5.5a shows the real-time change of resonance frequency and Q of the resonator during the evaporation of a 94 nL water droplet. An increase in the resonance frequency of the resonator is observed consistent with a decrease in the volume of the droplet. It is seen that the rate df_r/dt increases after $120s$ and becomes zero beyond $250s$ confirming complete evaporation of the droplet. In Fig. 5.5a, the Q of the resonance mode in the presence of the droplet is around ~ 1000 and increases to around 1200 after evaporation. The change of the Q is due to the viscous damping from the interaction between the water droplet and air. However, the influence of the change of Q on the observed resonance frequency shift is found to be negligible during evaporation since $f_r = f_u\sqrt{1-(\frac{1}{2Q})^2}$, where f_u is the undamped resonance frequency. It should also be noted that surface interactions between the droplet might affect the stiffness K_{eff} and might be extracted separately by monitoring both amplitude and frequency of the resonator.

To compare our results to a second method for estimating mass change from volume change assuming constant density, we also use the in-situ microscope of the setup to monitor the volumetric changes of the water droplet. In Fig. 5.5b we show the variation of droplet's contact angle β and contact radius r during evaporation using this second method (see Appendix A2). It can be seen that the droplet initially evaporates in the constant contact radius mode until $120s$, after which r starts to decrease linearly in time. This decrease is consistent with the increase in df_r/dt that we observed in Fig. 5.5a, since the resonance frequency is influenced by the distribution of the added mass (see Fig. 5.3c). By detecting β and r throughout evaporation, we can now calculate the volume changes and, accordingly, the mass of the water droplet using this second technique ($m = \frac{\pi\rho}{3}(\frac{r}{\sin\beta})^3(2+\cos\beta)(1-\cos\beta)^2$ [34]).

We repeat the same experiment for 4 water droplets of nL volumes and compare the mass estimations by both methods. These measurements are summarized in Fig. 5.5c where it can be observed that the estimated mass using our resonator is close to the one obtained by tracing volumetric changes using the microscope, with differences attributed to measurement errors.

5.4.4. FREQUENCY STABILITY

The mass precision of resonant mass sensors depends on the resolution with which frequency changes due to added particles/droplets can be determined. Therefore, the mass resolution or the minimum detectable particle mass is influenced not only by the responsivity $\mathscr{R}$ of the resonant sensor, but also by its frequency stability. In other words, for a mass change δm to be detected by the frequency change δf, it is essential that the shift in the frequency is greater than the frequency imprecision σ_a of the resonator [35]. This frequency imprecision depends on the time τ over which a frequency measurement is averaged, and can be defined as the Allan deviation of consecutive resonance frequency

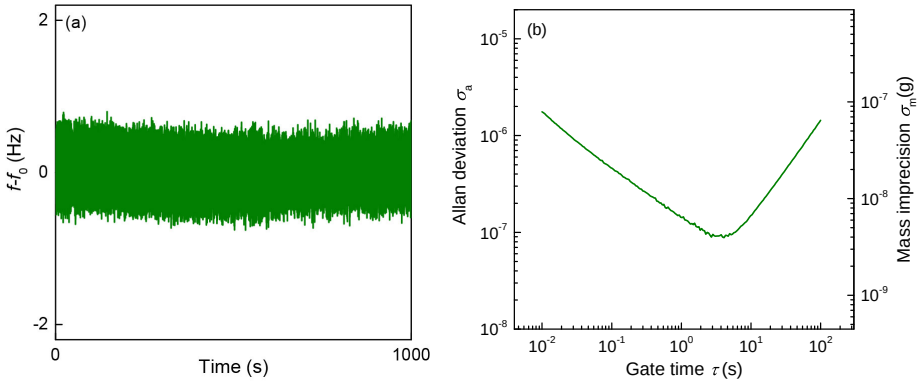

Figure 5.6: Frequency stability measurement. (a)Frequency fluctuation as a function of time; (b)Allan deviation and mass imprecision as a function of gate time of the levitating plate measured using a LDV and lock-in amplifier.

5

measurements each averaged over a time period τ (gate time) as follows:

$$\sigma_a = \sqrt{\frac{1}{2N}\sum_{n=0}^{N-1}\left(\frac{\bar{f}_{n+1}-\bar{f}_n}{f_0}\right)^2}, \tag{5.2}$$

in which $\bar{f}_n$ is the time average of the frequency measurement during the n^{th} gate time within a total N intervals and f_0 is the mean frequency calculated over the frequency tracking operation. To measure the frequency stability and thus Allan deviation of our levitating resonator, we use the PLL of the Zurich UHFLI lock-in amplifier and operate our measurements in closed loop. The PLL uses the output phase of the resonator's 3^{rd} bending mode to control the excitation frequency applied to the coil using a PI controller with proportional constant k_p and integral constant k_i. To implement the PLL, we use constants k_p =−1.4 Hz/deg and k_i = −2.8 Hz/deg/s that ensure a stable closed-loop operation and establish a PLL bandwidth of 111.6 Hz. Moreover, to maintain the resonator close to resonance, we set the phase set-point to $\pi/2$ after correcting for the shift introduced by the equipment.

Fig. 5.6a shows the recorded resonance frequency data in a time span of 1000 s and Fig. 5.6b shows its associated Allan deviation σ_a. We observe that the Allan deviation is approximately proportional to $\tau^{-1/2}$ for short gate times, which can be attributed to white noise sources, like from thermomechanical noise or from the LDV and actuation system [36]. For long gate times, the Allan deviation is proportional to τ which might be attributed to drift. Using the measured Allan deviation and experimental mass responsivity, we evaluate the mass imprecision of our resonant sensor ($\sigma_m = 2M_{\text{eff,exp}}\sigma_a$[36]), and report the values in Fig. 5.6b. The minimum mass imprecision is found to be 4.0 ng at τ = 3 s, which shows the potential of our resonant weighing scale for detecting mass changes due to particles down to a few ng, for example the mass fluctuation in cells [37].

5.5. CONCLUSIONS

In summary, we demonstrate a diamagnetically levitating graphite mass sensor that is electromagnetically driven into resonance. We use a laser Doppler vibrometer to characterize the first 10 elastic modes of the resonator and use glass beads with known mass to calibrate the mass responsivity of the levitating plate. By dispensing nano-liter droplets of different liquids and tracking the resonance frequency changes, we show the potential of the weighing scale to measure small mass changes due to the evaporation of the liquid. Finally, by operating the resonator in closed loop and measuring the Allan deviation of the frequency fluctuations, we show that mass resolutions down to a few nano-gram are within reach with low cost millimeter scale diamagnetically levitating sensors, showing the potential of these resonators for biological and chemical sensing applications.

5.6. APPENDIX

A1: RAYLEIGH-RITZ METHOD

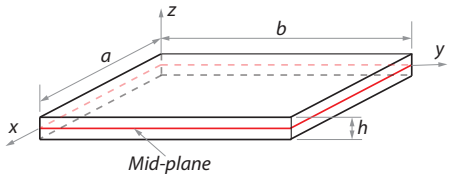

Figure 5.7: Geometry of the rectangle plate and coordinate system

A rectangular plate with in-plane dimensions a and b and thickness h is considered in an orthogonal coordinate system $(O : x, y, z)$, as shown in Fig. 5.7. Three displacements u, v and w are used to describe the plate middle surface deformation. The strain-displacement relations of the plate can be written as:

$$\begin{aligned} \epsilon_x &= \epsilon_{x_0} + zk_x, \\ \epsilon_y &= \epsilon_{y_0} + zk_y, \\ \gamma_{xy} &= \gamma_{xy_0} + zk_{xy}, \end{aligned} \tag{5.3}$$

where

$$\begin{aligned}
\epsilon_{x_0} &= \frac{\partial u}{\partial x}, \\
\epsilon_{y_0} &= \frac{\partial v}{\partial y}, \\
\gamma_{xy_0} &= \frac{\partial v}{\partial x} + \frac{\partial u}{\partial y}, \\
k_x &= -\frac{\partial^2 w}{\partial x^2}, \\
k_y &= -\frac{\partial^2 w}{\partial y^2}, \\
k_{xy} &= -\frac{\partial^2 w}{\partial x \partial y}.
\end{aligned} \tag{5.4}$$

The kinetic energy of the plate is obtained as:

$$T_\mathrm{p} = \frac{1}{2}\rho h \int_0^a \int_0^b (\dot{u}^2 + \dot{v}^2 + \dot{w}^2)\mathrm{d}x\mathrm{d}y + \frac{1}{2} m_\mathrm{add}(\dot{u}(x_a, y_a)^2 + \dot{v}(x_a, y_a)^2 + \dot{w}(x_a, y_a)^2), \tag{5.5}$$

where the overdot indicates differentiation with respect to time, and m_add is the mass of the added particle. Moreover, x_a and y_a are the x, y coordinates of the point where the particle is attached.

The elastic strain energy of the plate assuming isotropic material properties is [29]:

$$\begin{aligned}
U_\mathrm{p} = &\frac{1}{2}\frac{Eh}{1-\nu^2}\int_0^a \int_0^b (\epsilon_{x_0}^2 + \epsilon_{y_0}^2 + 2\nu\epsilon_{x_0}\epsilon_{y_0} + \frac{1-\nu}{2}\gamma_{xy_0}^2)\mathrm{d}x\mathrm{d}y \\
&+ \frac{1}{2}\frac{Eh^3}{12(1-\nu^2)}\int_0^a \int_0^b (k_x^2 + k_y^2 + 2\nu k_x k_y + \frac{1-\nu}{2}k_{xy}^2)\mathrm{d}x\mathrm{d}y,
\end{aligned} \tag{5.6}$$

where E is the Young's modulus and ν is the Poisson's ratio. In order to obtain natural frequencies and modes of vibration of the plate, we assume synchronous motion and express displacements u, v and w in the follwoing form:

$$\begin{aligned}
u(x, y, t) &= U(x, y)g(t), \\
v(x, y, t) &= V(x, y)g(t), \\
w(x, y, t) &= W(x, y)g(t),
\end{aligned} \tag{5.7}$$

where the functions $U(x, y), V(x, y)$ and $W(x, y)$ represent the mode shapes, while $g(t)$ is harmonic time function and is the same for all displacements. To obtain mode of vibration we use power polynomials:

$$\begin{aligned}
U(x, y) &= \sum_{m=0}^{M}\sum_{n=0}^{N} a_{mn} x^m y^n, \\
V(x, y) &= \sum_{m=0}^{M}\sum_{n=0}^{N} b_{mn} x^m y^n, \\
W(x, y) &= \sum_{m=0}^{M}\sum_{n=0}^{N} c_{mn} x^m y^n.
\end{aligned} \tag{5.8}$$

In order to find the linear free vibration response, a vector p comprising all unknown coefficients of Eq. (5.8) is built as follows:

$$\mathrm{p} = \{a_{00}, ..., a_{mn}, b_{00}, ..., b_{mn}, c_{00}, ..., c_{mn}\}. \tag{5.9}$$

The dimension of vector p is N_{max} that is equal to the total number of unknowns in Eq. (5.8). Therefore, $N_{max} = 3(M+1)(N+1)$. Next, the Lagrange equations of motion are obtained by assuming $\mathrm{g}(t) = \mathrm{p}g(t)$ where $g(t) = e^{j\omega t}$ with j being the imaginary unit and ω the vibration frequency as follows:

$$\frac{\mathrm{d}}{\mathrm{d}t}\frac{\partial T_p}{\partial \dot{g}_k} - \frac{\partial T_p}{\partial g_k} + \frac{\partial U_p}{\partial g_k} = 0, k = 1, ..., N_{max}, \tag{5.10}$$

which results in

$$(-\omega^2 \mathrm{M} + \mathrm{K})\mathrm{p} = 0, \tag{5.11}$$

where M is the mass matrix and K is the stiffness matrix of dimension $N_{max} \times N_{max}$. Setting the determinant of the vector p equal to zero, the eigenvalues will be obtained and substituting each eigenvalue into Eq. (5.11) gives its corresponding eigenvector. In order to obtain the natural mode corresponding to the i_{th} eigenvector, we substitute the coefficients a_{mn}, b_{mn}, and c_{mn} with a^i_{mn}, b^i_{mn} and c^i_{mn} which are the components of the $i-$th eigenvector obtained from Eq. (5.8) as:

$$\begin{aligned} U^{(i)}(x,y) &= \sum_{m=0}^{M}\sum_{n=0}^{N} a^{(i)}_{mn} x^m y^n, \\ V^{(i)}(x,y) &= \sum_{m=0}^{M}\sum_{n=0}^{N} b(i)_{mn} x^m y^n, \\ W^{(i)}(x,y) &= \sum_{m=0}^{M}\sum_{n=0}^{N} c(i)_{mn} x^m y^n. \end{aligned} \tag{5.12}$$

It is worth to note that in order to avoid matrix ill-conditioning in using power polynomials, high numerical accuracy is required. In this work the software *Mathematica 11.3* has been used with 300 digits of accuracy to avoid matrix ill-conditioning.

Using this model, by comparing the estimated resonance frequencies and the experimental resonance frequencies from Fig. 5.2 of the paper, we find that the graphite plate has an experimentally estimated Young's modulus $E = 3.72 \times 10^{10}$ Pa and Poisson's ratio $\nu = -0.25$ in reasonable agreement with literature values [38]. After that, by changing the m_{add}, we can calculate the frequency shift δf, thus calculating the mass responsivity of the third mode at point P to be $\mathscr{R}_{\mathrm{th}} = -0.25\,\mathrm{Hz}/\mu\mathrm{g}$.

A2: IMAGE PROCESSING METHOD

Typically, a liquid droplet can be viewed as a spherical cap when the contact radius of the droplet is smaller than the capillary length [39–41]. The capillary length l_{c} of a droplet can be obtained as

$$l_{\mathrm{c}} = \sqrt{\frac{\sigma}{\rho g}}, \tag{5.13}$$

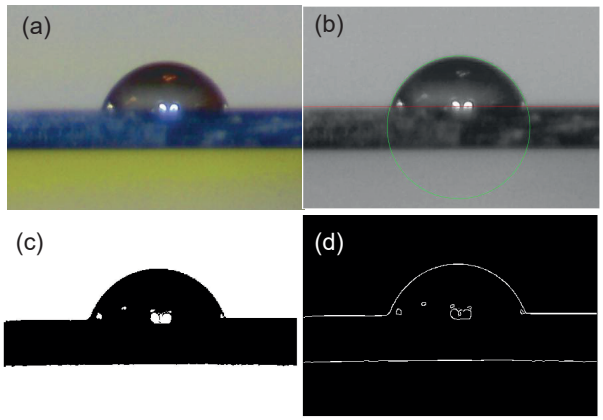

Figure 5.8: Image processing method. (a)Image of a droplet on top of the plate; (b) Gray scale image and a fitted circle and straight line; (c) Black and white image; (d) Edges of the droplet and plate.

where σ and ρ are the surface tension and density of the liquid, respectively, and g is the gravitational constant. For a water droplet, the capillary length is 2.7 mm which is much larger than the maximum contact radius of the droplet measured in our experiments i.e. $r = 0.4$ mm. The same holds true for our measurements with ethylene glycol ($r = 0.5$ mm) and glycerol ($r = 0.4$ mm) whose capillary lengths are 2.1 mm and 2.3 mm, respectively. Therefore, the droplets in our experiments can be seen as spherical caps, and their side view can be fitted with a circle.

After taking an image of the sessile droplet on the surface of graphite plate, we extract the contact radius r and contact angle β using an image processing method using Matlab. We first convert the image taken by the microscope (Fig. 5.8a) into grey scale (Fig. 5.8b) to make the edges of the droplet and plate more clear. Next, the grey picture is converted to black and white (Fig. 5.8c), and from this image, droplet and plate edges are identified (Fig. 5.8d). Finally to obtain the contact radius and contact angle, a line is drawn at the edge of the plate and a circle is fitted using three points on the edge of the droplet (see Fig. 5.8b). With the fitted circle and the straight line, the contact angle and radius are calculated in pixels. Using the known thickness of the plate as a reference, these values are then converted to mm.

REFERENCES

[1] X. Chen, N. Kothari, A. Keşkekler, P. G. Steeneken, and F. Alijani, "Diamagnetically levitating resonant weighing scale", Sensors and Actuators A: Physical **330**, 112842 (2021).

[2] K. Jensen, K. Kim, and A. Zettl, "An atomic-resolution nanomechanical mass sensor", Nature nanotechnology **3**, 533 (2008).

[3] J. Chaste, A. Eichler, J. Moser, G. Ceballos, R. Rurali, and A. Bachtold, "A nanomechanical mass sensor with yoctogram resolution", Nature nanotechnology **7**, 301–304 (2012).

[4]Y.-T. Yang, C. Callegari, X. Feng, K. L. Ekinci, and M. L. Roukes, "Zeptogram-scale nanomechanical mass sensing", Nano letters **6**, 583–586 (2006).

[5]Y. Zhang, "Detecting the stiffness and mass of biochemical adsorbates by a resonator sensor", Sensors and Actuators B: Chemical **202**, 286–293 (2014).

[6]P. Belardinelli, S. N. Souza, E. Verlinden, J. Wei, U. Staufer, F. Alijani, and M. K. Ghatkesar, "Second flexural and torsional modes of vibration in suspended microfluidic resonator for liquid density measurements", Journal of Micromechanics and Microengineering **30**, 055003 (2020).

[7]G. Wingqvist, J. Bjurström, L. Liljeholm, V. Yantchev, and I. Katardjiev, "Shear mode aln thin film electro-acoustic resonant sensor operation in viscous media", Sensors and Actuators B: Chemical **123**, 466–473 (2007).

[8]B. Morten, G. De Cicco, and M. Prudenziati, "Resonant pressure sensor based on piezoelectric properties of ferroelectric thick films", Sensors and Actuators A: Physical **31**, 153–158 (1992).

[9]P. S. Waggoner and H. G. Craighead, "Micro-and nanomechanical sensors for environmental, chemical, and biological detection", Lab on a Chip **7**, 1238–1255 (2007).

[10]B. N. Johnson and R. Mutharasan, "Biosensing using dynamic-mode cantilever sensors: a review", Biosensors and bioelectronics **32**, 1–18 (2012).

[11]M. A. Cooper, *Label-free biosensors: techniques and applications* (Cambridge University Press, 2009).

[12]S. Schmid, L. G. Villanueva, and M. L. Roukes, *Fundamentals of nanomechanical resonators*, Vol. 49 (Springer, 2016).

[13]R. A. Norte, J. P. Moura, and S. Gröblacher, "Mechanical resonators for quantum optomechanics experiments at room temperature", Physical review letters **116**, 147202 (2016).

[14]W. Wang and D. Weinstein, "Acoustic bragg reflectors for q-enhancement of unreleased mems resonators", in 2011 joint conference of the ieee international frequency control and the european frequency and time forum (fcs) proceedings (IEEE, 2011), pp. 1–6.

[15]A. H. Ghadimi, S. A. Fedorov, N. J. Engelsen, M. J. Bereyhi, R. Schilling, D. J. Wilson, and T. J. Kippenberg, "Elastic strain engineering for ultralow mechanical dissipation", Science **360**, 764–768 (2018).

[16]E. Brandt, "Levitation in physics", Science **243**, 349–355 (1989).

[17]X. Chen, A. Keşkekler, F. Alijani, and P. G. Steeneken, "Rigid body dynamics of diamagnetically levitating graphite resonators", Applied Physics Letters **116**, 243505 (2020).

[18]J. Gieseler, B. Deutsch, R. Quidant, and L. Novotny, "Subkelvin parametric feedback cooling of a laser-trapped nanoparticle", Physical review letters **109**, 103603 (2012).

[19]M. Simon and A. Geim, "Diamagnetic levitation: flying frogs and floating magnets", Journal of applied physics **87**, 6200–6204 (2000).

[20]H. Chetouani, C. Jeandey, V. Haguet, H. Rostaing, C. Dieppedale, and G. Reyne, "Diamagnetic levitation with permanent magnets for contactless guiding and trapping of microdroplets and particles in air and liquids", IEEE Transactions on Magnetics **42**, 3557–3559 (2006).

[21]C. Pigot, H. Chetouani, G. Poulin, and G. Reyne, "Diamagnetic levitation of solids at microscale", IEEE Transactions on Magnetics **44**, 4521–4524 (2008).

[22]D. Garmire, H. Choo, R. Kant, S. Govindjee, C. Sequin, R. Muller, and J. Demmel, "Diamagnetically levitated mems accelerometers", in Transducers 2007-2007 international solid-state sensors, actuators and microsystems conference (IEEE, 2007), pp. 1203–1206.

[23]S. Palagummi and F. Yuan, "A bi-stable horizontal diamagnetic levitation based low frequency vibration energy harvester", Sensors and Actuators A: Physical **279**, 743–752 (2018).

[24]Q.-H. Gao, W.-B. Li, H.-X. Zou, H. Yan, Z.-K. Peng, G. Meng, and W.-M. Zhang, "A centrifugal magnetic levitation approach for high-reliability density measurement", Sensors and Actuators B: Chemical **287**, 64–70 (2019).

[25]Q. Li, K.-S. Kim, and A. Rydberg, "Lateral force calibration of an atomic force microscope with a diamagnetic levitation spring system", Review of scientific instruments **77**, 065105 (2006).

[26]K. L. Ekinci, Y. T. Yang, and M. L. Roukes, "Ultimate limits to inertial mass sensing based upon nanoelectromechanical systems", Journal of applied physics **95**, 2682–2689 (2004).

[27]D. Ramos, J. Tamayo, J. Mertens, M. Calleja, and A. Zaballos, "Origin of the response of nanomechanical resonators to bacteria adsorption", Journal of Applied Physics **100**, 106105 (2006).

[28]P. Belardinelli, L. Hauzer, M. Šiškins, M. Ghatkesar, and F. Alijani, "Modal analysis for density and anisotropic elasticity identification of adsorbates on microcantilevers", Applied Physics Letters **113**, 143102 (2018).

[29]F. Alijani and M. Amabili, "Theory and experiments for nonlinear vibrations of imperfect rectangular plates with free edges", Journal of Sound and Vibration **332**, 3564–3588 (2013).

[30]F. Alijani, M. Amabili, P. Balasubramanian, S. Carra, G. Ferrari, and R. Garziera, "Damping for large-amplitude vibrations of plates and curved panels, part 1: modeling and experiments", International Journal of Non-Linear Mechanics **85**, 23–40 (2016).

[31]M. Alvarez and L. M. Lechuga, "Microcantilever-based platforms as biosensing tools", Analyst **135**, 827–836 (2010).

[32]K. Y. Gfeller, N. Nugaeva, and M. Hegner, "Rapid biosensor for detection of antibiotic-selective growth of escherichia coli", Applied and environmental microbiology **71**, 2626–2631 (2005).

[33]V. Kumar, J. W. Boley, Y. Yang, H. Ekowaluyo, J. K. Miller, G. T.-C. Chiu, and J. F. Rhoads, "Bifurcation based mass sensing using piezoelectrically actuated microcantilevers", Applied Physics Letters **98**, 153 510 (2011).

[34] A. D. Polyanin and A. V. Manzhirov, *Handbook of mathematics for engineers and scientists* (CRC Press, 2006).

[35] M. Sansa, E. Sage, E. C. Bullard, M. Gély, T. Alava, E. Colinet, A. K. Naik, L. G. Villanueva, L. Duraffourg, M. L. Roukes, et al., "Frequency fluctuations in silicon nanoresonators", Nature nanotechnology **11**, 552 (2016).

[36] T. Manzaneque, P. G. Steeneken, F. Alijani, and M. K. Ghatkesar, "Method to determine the closed-loop precision of resonant sensors from open-loop measurements", IEEE Sensors Journal **20**, 14262–14272 (2020).

[37] D. Martinez-Martin, G. Flaschner, B. Gaub, S. Martin, R. Newton, C. Beerli, J. Mercer, C. Gerber, and D. J. Müller, "Inertial picobalance reveals fast mass fluctuations in mammalian cells", Nature **550**, 500–505 (2017).

[38] A. Garber, "Pyrolytic materials for thermal protection systems", Aerospace Engineering **22**, 126–137 (1963).

[39] M. Härth and D. W. Schubert, "Simple approach for spreading dynamics of polymeric fluids", Macromolecular Chemistry and Physics **213**, 654–665 (2012).

[40] A.-M. Cazabat and G. Guena, "Evaporation of macroscopic sessile droplets", Soft Matter **6**, 2591–2612 (2010).

[41] H. Hu and R. G. Larson, "Evaporation of a sessile droplet on a substrate", The Journal of Physical Chemistry B **106**, 1334–1344 (2002).

6

Conclusions and Outlook

6.1. CONCLUSIONS

This dissertation aims at providing new insights into the dynamics of diamagnetically levitating resonators for developing ultra-low noise devices and sensors. In the previous four chapters, we studied both the rigid body and elastodynamics of a levitating resonator through modeling and experiments, with each chapter focusing on different topics and using different experimental strategies. We now summarize the main findings from our measurements and theoretical studies, and discuss their potential on the future research about diamagnetic levitation.

RIGID BODY DYNAMICS

In Chapter 2 we studied the rigid body dynamics of a diamagnetically levitating graphite resonator to have a better understanding of its stiffness and damping mechanisms. Through dynamic measurements and numerical simulations, we demonstrated that the stiffness and damping of a levitating resonator are determined by the magnetic field that enables the levitation. By calculating the magnetic force as a function of levitation height, we determined the natural levitation height and resonance frequencies, which agreed well with the detected rotational and translational modes. Moreover, to find out the dissipation root of the levitating resonator, we conducted measurements in vacuum conditions and modeled the damping using FEM methods. The good agreement between the measured Q factors and simulations provided strong evidence that eddy current damping is dominant in a diamagnetically levitating resonator in rigid body dynamics. With modeling, we found that the Q factors are increasing when scaling the resonator down and predicted that Q factors above 100 million might be attainable when the resonator size reduces to micro scale. The study in this Chapter not only revealed the relations between the magnetic field and the levitating resonator's stiffness and damping, but also provided a method to model magnetic stiffness and eddy current damping in more general situations.

After finding out the underlying dissipation source in the levitating resonators, the next step was to decrease the damping. Instead of reducing the resonator size as predicted in Chapter 2, in Chapter 3 we improved the Q factors by fabricating diamagnetic composites in order to keep the resonators at macroscopic scale, noting that high-Q macroscopic resonators are advantageous in sensing applications, e.g., accelerometers or gravimeters, and are interesting in quantum mechanics. The composites were made by randomly dispersing micro graphite particles in an epoxy matrix. The results showed that millimeter composite plates are able to levitate stably above permanent magnets in high vacuum (10^{-6}mbar) with graphite volume fraction as low as 14 % due to the strong diamagnetic property of graphite. Meanwhile, by isolating the graphite particles using insulating epoxy, eddy currents are confined inside the particles and damping can be remarkably diminished. With those composites, Q factors as high as nearly 0.5 million are achieved at room temperature for resonators with mass bigger than 1 mg. We also studied the dependency of damping on particle size, volume fraction and plate size, concluding that the damping is most sensitive to particle size with Q inversely proportional to the square of particle size $Q \propto 1/d^2$. The combination of large mass and high Q make these levitating composite resonators attractive for realizing room temperature accelerometers with theoretical noise levels as low as $0.16\,\mathrm{ng}/\sqrt{\mathrm{Hz}}$, that are comparable

to superconducting levitodynamic systems at cryogenic temperatures. Reduction of the particle size and optimization of particle distribution and orientation, can lead to novel composites that further enhance the performance of future macroscopic levitating devices used as accelerometers, gravimeters, or sensors for exploring macroscopic limits of quantum mechanics. More generally, the proposed method in Chapter 3 can be used to reduce eddy current damping in areas where eddy currents are a limiting factor of performance, such as in applications of energy harvesters, rotors, bearings and trains based on magnetic levitation, as well as transformer cores.

To get a more comprehensive understanding of the dynamics of a diamagnetically levitating system, we explored the nonlinear dynamics of a levitating graphite resonator in Chapter 4. We actuated the levitating resonator using a shaker and conducted the dynamic measurements in vacuum, thus its stiffness was not influenced by either the excitation method such as electrostatic force or the air squeeze force. The experimental results showed that the frequency response curves of the levitating resonators exhibit softening behaviour. Since their stiffness is solely governed by magnetic field, by measuring and modeling the magnetic force as a function of displacement, we concluded that the effective magnetic stiffness is softening even though the restoring force is strongly asymmetric around the motion at origin. By modeling the dynamic response, we found that the cubic Duffing nonlinearity coefficient does not suffice to fully capture the large amplitude motion of a levitating resonator, and quintic functions are required to fully probe its stiffness with accuracy. Furthermore, measurements in both air and vacuum conditions showed that the eddy current damping is approximately linear with the vibration amplitude, while the air damping is strongly nonlinear and amplitude dependent. The study in this Chapter provides new insights into the dynamics of a diamagnetic levitation system in terms of nonlinear stiffness and damping. This is crucial especially when the levitating resonator's size shrinks down to micro scale where the nonlinear regime is more easily reached due to the low damping. On the other hand, the study provides new opportunities for bifurcation-based sensors which might be superior compared to linear resonant sensors in certain cases.

ELASTODYNAMICS

In the rigid body dynamics, the levitating resonator's stiffness and damping are coupled to the magnetic field that is required for the levitation. Therefore, the levitating object is not truly free from its environment. However, with the frequency increasing, magnetic field and gravitational forces become negligible compared to the elastic forces of the material, such that a levitating object can be viewed as truly free in terms of its elastodynamics. In Chapter 5, we investigated the bending vibrations of a diamagnetically levitating graphite resonator and developed a resonant mass sensor. Using an electromagnetic actuator, the elastic modes of the levitating resonator can be sufficiently excited and its first 10 modes were detected, which agreed well with our analytical model for an all edge free plate. Based on the frequency shift of the resonator, we detected mass changes and developed a mass sensor using its third mode and calibrated its mass responsitivity using micro glass beads. To validate the sensor, we utilized it to measure the density of three kinds of liquids and detected the real-time evaporation of water droplets. Finally by measuring the Allan deviation of the sensor's frequency stability, we determined the

detectable mass resolution to be 4 ng. The study in this Chapter demonstrated that diamagnetic levitation can be used to develop easy to use sensors for biological or chemical applications.

In summary, we studied diamagnetic levitation because it is the only passive levitation method that does not require any energy input and its strong magnetic potential can enable levitation of macroscopic objects. With a checkerboard arrangement of four permanent magnets, millimeter plates can be stably levitated. In this thesis, we focused on the resonant response of the levitating plates in both rigid body and elastic modes, with the goal towards attaining low-noise devices. We believe the findings in this thesis, especially in the aspects of magnetic stiffness, eddy current damping and elastodynamics, will shed light on the future studies and applications of diamagnetic levitation. Due to its nature of being passive and compatible to macro objects, diamagnetic levitation is as simple as it is promising in the development of next-generation unclamped low-noise devices that require macroscopic mass or length, such as accelerometers, gravimeters and platforms for testing macroscopic limits of quantum mechanics.

6.2. OUTLOOKS AND RECOMMENDATIONS

In addition to the above studies, there are many other topics about diamagnetic levitation that are worthy to follow up. We list some of them in this section.

6.2.1. INFLUENCE OF MAGNET ARRANGEMENT ON THE RIGID BODY DYNAMICS

In the above studies, from Chapters 2 to 5, the plate is levitating above a 2×2 array of magnets, as shown in Fig. 6.1a. However, there are many other magnet arrangements that can generate a potential well required for stable levitation, for example the 4×4 and 5×5 array of magnets as shown in Fig. 6.1a. Here we study the dependency of

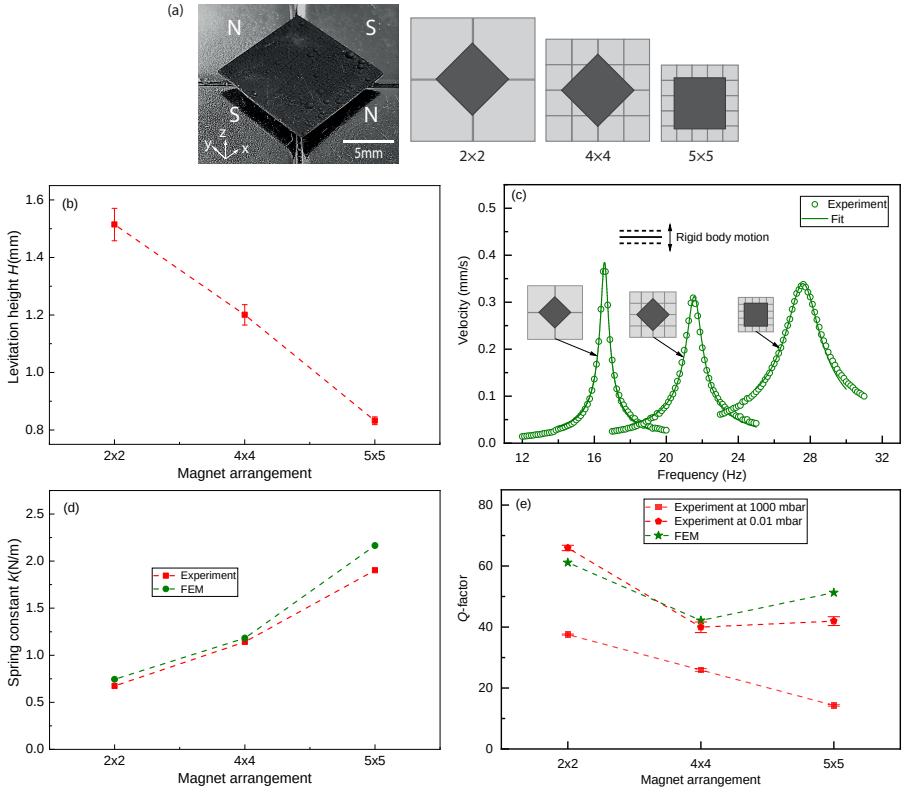

Figure 6.1: (a) Image of a $10.24 \times 10.24 \times 0.28\,\text{mm}^3$ pyrolytic graphite plate levitating above 4 cubic neodymium magnets with alternating magnetization, where N and S stand for north and south pole of the magnet, respectively; and schematic of three magnet arrangements: 2×2, 4×4 and 5×5. The edge lengths of the cube magnets used in these configurations are 12, 5 and 3 mm, respectively; (b) Frequency response curves of the levitating plate over 3 different magnet arrangements in air and fitted curves using a damped harmonic oscillator model. The inset shows the associated rigid body motion schematically; (c) Spring constant of the resonator obtained by experiments and FEM simulations; (d) Levitation height of the plate over three magnet arrangements measured using Keyence Digital Microscope VHX-6000; (d) Q-factor measured in air and vacuum(0.01 mbar) as well as those obtained by FEM simulations.

levitation height, resonance frequencies and Q-factor of a levitating plate on magnet arrangements.

The magnet arrangements, as shown in Fig. 6.1a, consist of cubic magnets with size of 12 mm (2 × 2 array), 5 mm (4 × 4 array) and 3 mm (5 × 5 array). With these three magnet arrangements, a $10.24 \times 10.24 \times 0.28\,\mathrm{mm}^3$ pyrolytic graphite plate can levitate stably above them and their levitation heights are show in Fig. 6.1b. From Fig. 6.1b, we observe a clear decreasing trend of levitation height with smaller magnets, which is because the magnetic field of smaller magnets diminishes faster with distance, thus generating a smaller magnetic field at the plate location even though their remanent magnetic fields of the magnets themselves are the same. Using the experimental setup in Fig. 2.1, we can detect the frequency response of the plate levitating above these magnet arrays in air (see Fig. 6.1c). From the figure, we see that the resonance frequency of the plate is increasing with smaller magnets. This can be explained by their increasing stiffness (see Fig. 6.1d) due to the smaller levitation height which increases the magnetic field gradient. In Fig. 6.1c, we also plot the spring constant k for the 3 magnet arrangement calculated using COMSOL simulations (see A3 in Chapter 3 for more details), which agrees well with the measurements.

Next, we study the influence of magnet arrangements on the damping of the levitating plate in both air and vacuum conditions. In Fig. 6.1e, the experimental Q-factor at atmospheric (1000 mbar) and low pressure (0.01 mbar) is plotted for the 3 magnet arrangements. It is seen that at low pressure the Q-factor increases significantly, because gas damping is eliminated at this pressure level (see Fig. 2.3a). At atmospheric pressure, the air damping is dominant, thereby the Q is decreasing with smaller levitation gaps (see Fig. 6.1e). At low pressure, the main damping source of the levitating resonator is eddy currents. Therefore, the Qs for different magnet arrangements can be calculated by only considering the eddy current damping and are shown in Fig. 6.1e, which match well with the trend of measured results in vacuum. It is noted that the dependency of eddy current damping on magnet arrangements is a combined effect from the magnetic field distribution, levitation height and resonance frequency.

In conclusion, in Fig. 6.1, we show that the rigid body dynamics of a diamagnetically levitating plate is strongly dependent on the magnet arrangements. For the 3 magnet arrangements studied in this section, we find that the levitation height is decreasing with smaller magnets, which results in a increase in the resonance frequencies and a decrease in the Q in air. For the eddy current damping, the Q shows a complicated dependency on the magnet arrangement, which can be well captured by our numerical modeling.

In the future, we can tune the resonance frequencies and damping by using different magnet arrangements, in order to meet different application requirements. Moreover, using the numerical modeling methods, we can accurately predict the stiffness and Q of a diamagnetically levitating resonator with any magnet arrangement.

6.2.2. ELASTODYNAMICS OF A LEVITATING RESONATOR

From the previous section, we know that even though the levitating resonator is free from mechanical constraints, its rigid body dynamics are still coupled with the magnetic field that supplies the levitation force, i.e., its resonance frequencies and Q-factors are dependent on the magnetic field. Therefore, the levitating resonator is not truly free in

terms of rigid body dynamics. However, the story for elastodynamics is different. In this section, we will study the influence of the magnet arrangements on the elastodynamics of a levitating resonator and then use the levitation to study the elastodynamics of a free plate.

Like in Chapter 5, using the experimental setup in Fig. 5.1c, we can excite and measure the kHz bending modes of a $10.24 \times 10.24 \times 0.28\,\text{mm}^3$ levitating plate over a 2×2 magnet array. Fig.6.2a shows the first 10 resonance peaks and their corresponding mode shapes of the levitating plate. To investigate how the magnetic field influences the bending modes, we measure the resonance frequencies and Qs of the first 3 elastic modes of the plate levitating over 3 different magnet arrangements. In contrast to the rigid body dynamics (Fig. 6.1c), Fig. 6.2b shows that the kHz elastic resonance frequencies are independent from the magnet arrangements. This implies that the bending rigidity which determines the elastic resonance frequencies of the levitating plate is not influenced by the magnetic field.

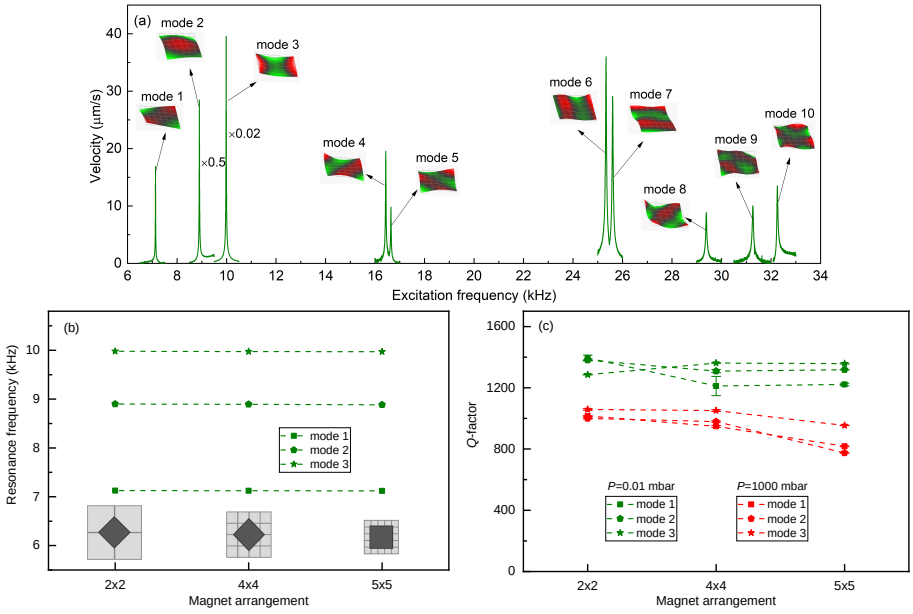

Figure 6.2: (a) Experimental resonance peaks and mode shapes of 10 elastic modes of a $10.24 \times 10.24 \times 0.28\,\text{mm}^3$ levitating plate over the 2×2 magnet arrangement in air; (b) Resonance frequency of the first three elastic modes of the plate levitating over 3 magnet arrangements measured in air; (c) Q-factor of the first three elastic modes of the plate levitating over different magnet arrangements measured in air and vacuum (0.01 mbar).

Next we study the damping of the bending modes of the levitating plate, by measuring the Qs of the first 3 modes of the plate over different magnet arrangements in both atmospheric (1000 mbar) and vacuum (0.01 mbar) pressures, and show the results in Fig. 6.2c. It can be seen from the figure that the Qs have a slight decreasing trend with smaller magnets in air due to the smaller levitation gaps (Fig. 6.1b). However, when conducting experiments in vacuum conditions, the dependency of Qs on magnet arrangements is

not significant (see Fig. 6.2c), which contrasts with the Qs of rigid body modes (see Fig. 6.1e). This is because for kHz bending modes, the material damping is dominant and it is independent from magnetic field. Therefore, from Fig. 6.2b-c, we can conclude that the elastodynamics of a levitating plate is independent from the magnetic field and the levitating plate can be approximated to be truly free.

Since the levitating plate is free from mechanical constrains and magnetic field, it can be modelled as a free plate and used for material property characterization. Using the same analytical method described in Section 5.6A1, we can identify the Young's modulus and Poission's ratio of the levtitating material by comparing the calculated and measured resonance frequencies. The material we use in our experiments is pyrolytic graphite, and its Young's modulus and Poisson's ratio are estimated to be $E = 21.679\,\text{GPa}$ and $\nu = -0.213$, respectively, as shown in Fig. 6.3a. In Fig. 6.3a, we also include the data calculated by FEM simulations using the estimated E and ν, which agree well with the analytical and measured results. In order to further validate our analytical modelling, the same experiments are performed on plates with different dimensions. The good agreement between analytical and experimental data (see Fig. 6.3b-c) verifies that elastodynamics of diamagnetically levitating objects can be very well modelled as free vibrations of floating structures.

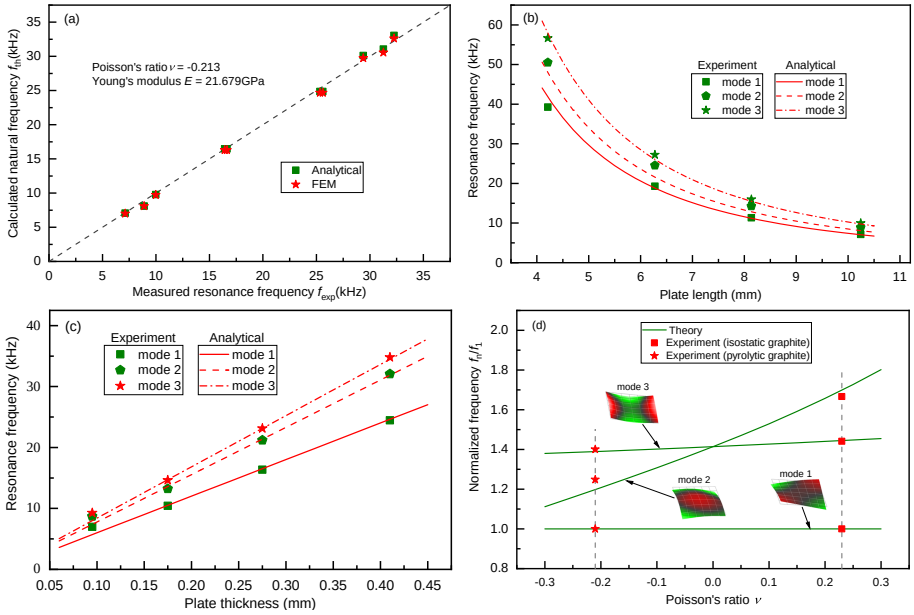

Figure 6.3: (a) Comparison between the measured resonance frequencies and the estimated ones obtained by analytical and FEM methods using the identified E, ν; (b) Comparison between the measured and estimated resonance frequencies of plates with different lengths and the same thickness of 0.28 mm; (c) Comparison between the measured and estimated resonance frequencies of plates with different thickness and the same length of 10.24 mm; (d) The change of the normalized first three frequencies f_n/f_1 (f_1 is the frequency of mode 1) with Poisson's ratio ν obtained by the analytical method, and the measured first three resonance frequencies of a $10.24 \times 10.24 \times 0.28\,\text{mm}^3$ pyrolytic graphite ($\nu = -0.213$) and an $9.48 \times 9.48 \times 0.46\,\text{mm}^3$ isostatic graphite plate (ν=0.230, purchased from Tokai Carbon).

An interesting observation here is the negative Poisson's ratio that is extracted for the pyrolytic graphite resonator ($\nu = -0.21$). The negative Poisson's ratio is found to be in agreement with previously reported values [1]. Materials with a negative Poisson's ratio are also called auxetic materials. To highlight the role of such auxetic behavior on the dynamics of our diamagnetically levitated resonator, we model the elastic modes of a plate with varying Poisson's ratio. It is noted that the normalized resonance frequencies are only dependent on Poisson's ratio, independent from the Young's modulus and plate dimensions [2]. Thereby, in Fig. 6.3d, we show the change on the normalized resonance frequencies of the first 3 modes and their mode shapes as a function of ν. It is interesting to observe that, the order of mode 2 and mode 3 swaps when the Poisson's ratio changes from negative to positive. In Fig. 6.3d, we also plot the measured data of a pyrolytic graphite ($\nu = -0.213$) and an isostatic graphite plate (ν=0.230), which verifies our theoretical observations.

This result shows the potential of modal analysis in determining the auxetic nature and Poisson's ratio of materials. We also note that the swap of mode shapes only occurs in plates with free boundary conditions, while the clamped plates do not demonstrate this unique property (see Fig. 6.4). Thereby, it concludes that the presented levitating resonant measurement methodology provides a useful platform for characterizing material properties of thin plates, since the levitating objects can be viewed as free plates.

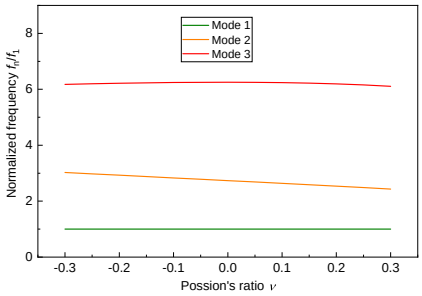

Figure 6.4: Change of the normalized resonance frequency f_n/f_1 (f_1 is the frequency of mode 1) with Poisson's ratio ν of the first 3 modes of a $10\times10\times0.2\,\mathrm{mm}^3$ single-clamped plate. The data is obtained by FEM simulations.

A future direction of studying diamagnetically levitating resonators is to utilize the resonators' elastodynamics further and this research field is in fact rarely exploited in literature. Unlike other levitation methods, diamagnetic force enables levitation of large objects and free boundary conditions of the levitating structures. Thus, it provides a unique platform to study the elastodynamics of a free structure that is completely isolated from its environment, which is useful in material characterization based on dynamics [3]. For example, by depositing a thin layer of any material on top of a millimeter graphite plate, the material's properties can be identified by looking at its dynamic response. Moreover, with the reduction of size, structures of many diamagnetic materials can be levitated. This will not only enable property characterization of different materials, but also make it possible to study many interesting phenomena like the resonance of water droplets.

6.2.3. DIAMAGNETICALLY LEVITATING COUPLED RESONATORS

While the studies from Chapter 2-5 are concerned with the dynamics of only one levitating resonator, it is interesting to study the dynamics of two resonators levitating above a magnet array and investigate the coupling mechanism between them. This is because through coupling, sensitivity of resonant sensors can be significantly improved [4, 5].

Here we study the dynamics of two levitating resonators that are coupled through air[1]. The two graphite plates are levitating above four NdFeB magnets with alternating magnetizations, as shown in Fig. 6.5a. The dimensions of the plates are $4 \times 4 \times 0.2\,\text{mm}^3$ and $8 \times 8 \times 0.2\,\text{mm}^3$, respectively. Therefore, they levitate at different heights, with the large plate on the top and the small one on the bottom, as shown in Fig. 6.5b. In order to shine a laser on the smaller plate and detect its motion, a hole with a diameter of 2 mm is cut at the center of the larger plate (see Fig. 6.5b). The experimental setup used to measure the dynamic response of the levitating resonators is shown in Fig. 6.5b. To excite the levitating plates, we place a piezoelectric disc beneath the magnets. The excitation signal is generated by a function generator (junction box) and amplified by a amplifier, which is then connected to the piezo disc. To detect the motion of the plates, a Polytec MSA400 is used to measure the velocity of the vibration by shining a laser beam on the plate. Finally, the detected signal is transferred to a PC for frequency response analysis. The experiments are conducted in a vacuum chamber with pressure from 0.003 mbar to 1000 mbar.

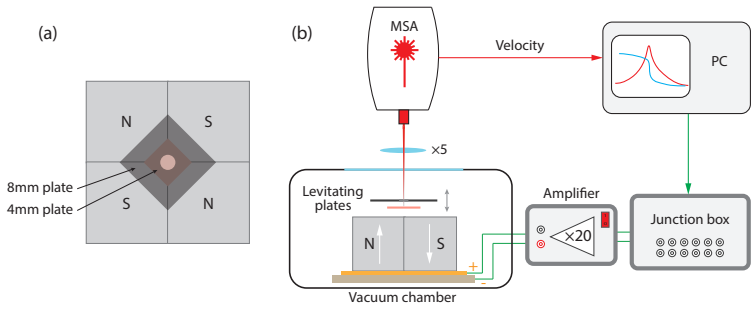

Figure 6.5: Levitating resonators and measurement setup. (a) Top view of two graphite plates levitating over four NdFeB magnets (also see the side view in Fig. 6.5b). The big plate has a hole at the center to enable the motion detection of the small plate beneath it. (b) Schematic of the measurement setup comprising a MSA400 Polytec LDV for the read out and piezoelectric excitation method. The actuation voltage is generated by the LDV junction box and is amplified by a 20 × voltage amplifier that drives the levitating plate into resonance using base actuation through the piezo disc. By focusing a MSA laser beam on the plate, the vibration signal is detected,and the acquired velocity is transferred to a PC for frequency response analysis.

To identify the resonance frequency of the plates individually, we place one plate above the magnet array at a time and measure its frequency response. The frequency response curves of the two plates measured in both air and vacuum conditions are shown in Fig. 6.6. At atmospheric pressure, we observe resonance of the plates at 22.8 Hz for the 4 mm plate and at 18.1 Hz for the 8 mm plate, respectively. The mode shapes cor-

[1] Parts of the results about coupled resonators were measured and analyzed together with Chris Wattjes for his Bachelor Honours Programme project

responding to these resonances are the rigid vertical motion, as schematically shown in Fig. 6.6. When measured in vacuum (0.003 mbar), the resonance peaks become sharper (see Fig. 6.6), corresponding to higher Qs due to the removal of air damping. It is noted that the resonance frequency of the small plate has a slight decrease in vacuum, which we contribute to the reduction in mass loading by the surrounding gas. In contrast, the resonance frequency of the larger plate increases slightly in vacuum. This is possibly because for this plate, the frequency is more influenced by the stiffness due to the surrounding gas and the stiffness is smaller in vacuum.

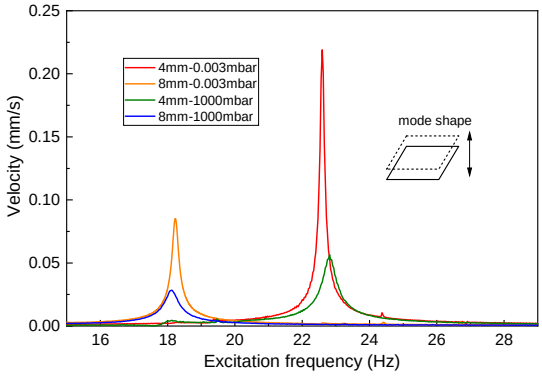

Figure 6.6: Frequency response of the 4 mm and 8 mm levitating plates in air (1000 mbar) and vacuum (3×10^{-3} mbar). The data is measured individually by placing each plate above the magnets. The inset shows the mode shape of the resonance.

To study the coupling effects, we place both the plates above the magnets and measure the frequency response of the small plate at different pressures. The results are shown in Fig. 6.7. In the figure, we show that when the pressure is low (below 0.23 mbar), only one peak is observed at around 22.8 Hz, which agrees with the resonance frequency of the small plate measured individually (see Fig. 6.6). With the pressure increasing, a second peak shows up in the frequency response curves at a pressure of 1.4 mbar. The second mode is at around 18.3 Hz, which is corresponding to the resonance frequency of the larger plate (see Fig. 6.6). This indicates that a coupled mode on the small plate is triggered by the big plate through air damping. The two peaks exist together at a certain range of pressure. After a certain pressure, only the resonance frequency related to the larger plate (around 18.3 Hz) is detected in the frequency response curve of the small plate. The reason is that at high pressure, the air drag force from the big plate is significant, thereby dominating the small plate's motion by driving it to move together.

To better understand the coupling mechanism between the two levitating resonators, a dynamic model of the system is needed. One example is a two degree-of-freedom system shown below:

$$\begin{aligned} m_1\ddot{x} + c_1\dot{x} + k_1 x + k_c(x-y) + c_c(\dot{x}-\dot{y}) &= F_1 \cdot \sin(\omega t), \\ m_2\ddot{y} + c_2\dot{y} + k_2 y - k_c(x-y) - c_c(\dot{x}-\dot{y}) &= F_2 \cdot \sin(\omega t), \end{aligned} \tag{6.1}$$

where m_1, c_1, k_1, x are the mass, viscous damping coefficient, stiffness and displacement

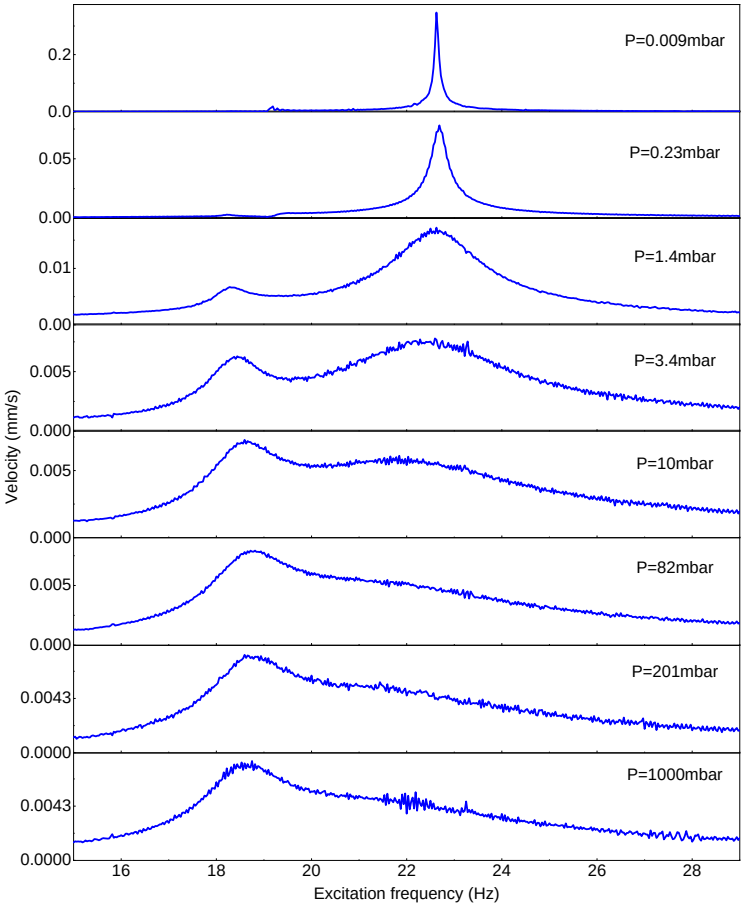

Figure 6.7: Frequency response curves of the 4 mm plate measured in different pressures, when both the plates are placed above the magnets.

of the small plate; and m_2, c_2, k_2, y are the mass, viscous damping coefficient, stiffness and displacement of the big plate; $F \cdot \sin(\omega t)$ is the driving force; k_c is the coupling stiffness, which is a function of pressure. It is interesting to note that in this system (Eq. (6.1)), c_1, c_2, k_c are all changing with pressure. The term c_c, that depends on the pressure dependent squeeze-film damping in the gap between the plates, also causes coupling.

More detailed modeling is needed to understand the coupling mechanism by comparison with the measurements. The coupling terms k_c and c_c can be physically interpreted by analysing the stiffness or damping force due to the gas pressure between the two resonators. Apart from coupling through gas, the levitating resonators can also be coupled through forces like electrostatic force or laser beams. We have tried to study the coupling effects using electrostatic force for two millimeter levitating plates, but the force is not strong enough to observe the coupling phenomenon. By reducing the size of

the levitating resonators, it is still possible to couple the resonators through electrostatic force. One more interesting topic to pursue might be coupling two levitating graphite plates using laser light, since the heat induced by laser is able to control the motion of a graphite plate [6].

6.2.4. DIAMAGNETICALLY LEVITATING MICRO OBJECTS

Reducing the size of diamagnetic levitation systems will bring many new possibilities. First, according to Fig. 2.3e in Chapter 2, the Q of levitating resonators increases significantly with reduced size. Moreover, based on the size reduction law [7], small objects can be levitated easier and this makes it possible for the levitation of a wide variety of materials with weak diamagnetism. Finally, with a smaller structure, mass is smaller and frequency is higher, which is important for applications like force sensing.

Here we demonstrate the successful levitation of a micro particle above a millimeter permanent magnet. To levitate an object above a single permanent magnet, we modify the magnetic field distribution by cutting holes on the surface of the magnet, as shown in Fig. 6.8a. With the cutting, the magnet will possess a potential well that enables stable levitation of a particle. Fig. 6.8b shows a $10 \times 5 \times 3\,\mathrm{mm}^3$ NdFeB magnet with an array of holes with radius of 200 μm and different depths. The holes are cut using a Lasea femtosecond micro laser cutter and the depths are controlled by applying different cutting time during the fabrication process. With the cut magnet, graphite particles with nominal size of 20 μm purchased from Sigma-Aldrich are spread above the holes using a cotton stick. The particles fall down freely and randomly towards the magnet, and some of them are trapped inside the holes. Fig. 6.8c demonstrates a particular case of successful trapping of a particle inside a hole with radius of 200 μm and depth of 350 um. The particle levitates inside the hole with a distance of approximately 100 μm to the top surface of the magnet. In contrast to our simulations where the particle is at the center of the hole, the trapped particle levitates at an off-centered position, as shown in Fig. 6.8c. The

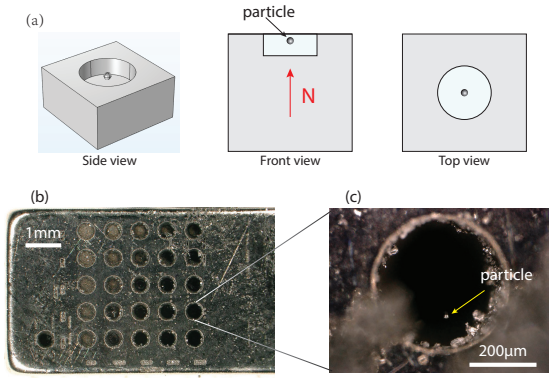

Figure 6.8: (a) Schematic of a micro sphere levitating inside a hole of a permanent magnet in three viewing directions (not to scale). N stands for the north pole of the magnet. (b) A NdFeB magnet with an array of holes with radius of 200 μm and different depths. The holes are cut using a Lasea micro laser cutter. (c) A 20 μm graphite particle levitating inside a hole of a magnet. The radius and depth of the hole are 200 μm and 350 μm, respectively.

reason might be that the cut is not perfectly round through the depth and the bottom of the hole is not flat, which influences the distribution of the magnetic field. Moreover, in our experiments, successful levitation of one or multiple particles are observed in holes with depths from 300 μm to 480 μm.

In the future, more systematic research can be done to study how the dimensions of the holes and particles influence the stable levitation by both simulations and experiments. Afterwards, it would be interesting to study the dynamics of the levitating particles. Based on the prediction in Fig. 2.3e of Chapter 2, the Q of the levitating micro particles is expected to be significantly higher under high vacuum conditions. With the extremely low damping and isolation from environment, highly sensitive force or acceleration sensors could be developed.

6.2.5. HIGH-Q LEVITATING MACROSCOPIC RESONATORS

Levitating macroscopic structures has many advantages. Firstly, the shape is more controllable for a macroscopic structure and the loading of it in a levitation trap is easier, which makes a resonator more compatible with different applications. Moreover, for many sensors, e.g., accelerometer and gravimeter, a larger mass results in a better sensitivity because mass is directly coupled with the force or phenomena to be sensed. In quantum mechanics, there is an increasing interest in observing the quantum superposition and entanglement in macroscopic objects, and high-Q levitating macroscopic resonators might make this possible.

In Chapter 3, we demonstrate a high-Q levitating resonator based on diamagnetic composites, and conclude that there are still a lot of improvements that can be made to push their Qs further. One drawback in the composite materials is that the particles are randomly dispersed inside the epoxy matrix without control of the particles' size, shape and distribution. Therefore the Q of the composite resonator is still limited by the eddy current damping due to the imperfect fabrication. To overcome these limitations, we propose a new fabrication method to reduce the eddy currents by laser cutting. The fabrication procedure is shown in Fig. 6.9a. We first coat a thin layer of epoxy resin on the bottom surface of a graphite sheet and let the epoxy cure in open air. We then use a laser cutter to cut through the graphite sheet and make a pattern. To maintain the rigidity, epoxy resin is again used to fill the trench in the graphite sheet. After curing, sand paper is used to polish the composite into desired thickness. A particular sample with grids of 100 μm is shown in Fig. 6.9b.

Due to the strong diamagnetism of the graphite, we were able to levitate these meshed graphite samples. In the future, we will measure their Qs in high vacuum. By tailoring the graphite grid size, shape and distribution in a controllable way, the Q of a millimeter meshed graphite plate with grids below 10 μm is predicted to be above 1 million. With a combination of high Q and large mass by designing the composites, it is possible to realize ultra-sensitive accelerometers or gravimeters.

Another direction that is worthy of investigation is using these high-Q composites as platforms for quantum experiments. The first step for quantum experiments is to prepare these resonators at quantum ground state, which seems not yet possible for these levitation systems at room temperature due to their low Q and frequency. However, by engineering the composites and magnetic field, it could be possible to have the Q and

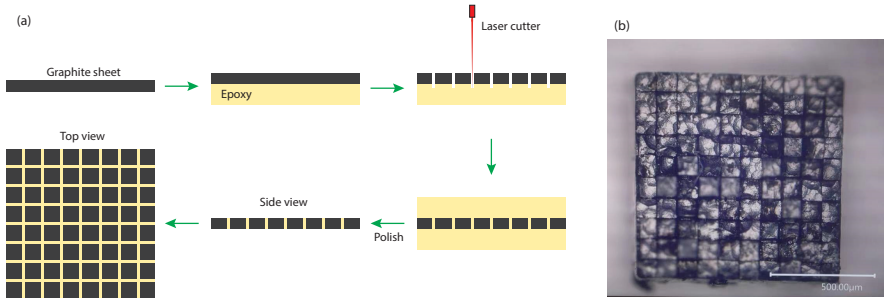

Figure 6.9: (a) Fabrication process of composites. A layer of epoxy resin is first coated on the bottom surface of a graphite sheet and wait for 10 minutes to let the epoxy cure; after which a Lasea laser cutter is used to cut through the graphite and make a pattern. To maintain the rigidity, epoxy resin is again used to fill the trench in the graphite sheet. After the epoxy is cured, sand paper is used to polish the composite into desired thickness. (b) A graphite sample after laser cutting.

frequency of a levitating resonator reach $Q = 1 \times 10^8$ and $f = 2000\,\text{Hz}$, where quantum ground state cooling might become achievable [8]. The efforts are worthy to make, since diamagnetic levitation shows a significant potential compared to optical and electrical levitation which can only levitate micro objects, and superconducting levitation that requires operation in cryogenic temperatures.

This outlook shows only a few examples of the large number of avenues that might still be explored in the field of levitodynamics using diamagnetic devices. Hopefully, this thesis will contribute to paving the way for future levitation-based science and applications.

REFERENCES

[1] A. Garber, "Pyrolytic materials for thermal protection systems", Aerospace Engineering **22**, 126–137 (1963).

[2] A. W. Leissa, *Vibration of plates*, Vol. 160 (Scientific, Technical Information Division, National Aeronautics, and Space Administration, 1969).

[3] D. Davidovikj, F. Alijani, S. J. Cartamil-Bueno, H. S. van der Zant, M. Amabili, and P. G. Steeneken, "Nonlinear dynamic characterization of two-dimensional materials", Nature communications **8**, 1–7 (2017).

[4] C. Zhao, M. H. Montaseri, G. S. Wood, S. H. Pu, A. A. Seshia, and M. Kraft, "A review on coupled mems resonators for sensing applications utilizing mode localization", Sensors and Actuators A: Physical **249**, 93–111 (2016).

[5] M. S. Hajhashemi, A. Rasouli, and B. Bahreyni, "Improving sensitivity of resonant sensor systems through strong mechanical coupling", Journal of Microelectromechanical Systems **25**, 52–59 (2015).

[6] M. Kobayashi and J. Abe, "Optical motion control of maglev graphite", Journal of the American Chemical Society **134**, 20593–20596 (2012).

[7] O. Cugat, J. Delamare, and G. Reyne, "Magnetic micro-actuators and systems (magmas)", IEEE Transactions on magnetics **39**, 3607–3612 (2003).

[8] Y. Seis, T. Capelle, E. Langman, S. Saarinen, E. Planz, and A. Schliesser, "Ground state cooling of an ultracoherent electromechanical system", Nature communications **13**, 1–7 (2022).

ACKNOWLEDGEMENTS

Four years of my PhD study are going to end when I am writing this page. It is worth spending some time looking back. In short, I am grateful that I made the choice to go to Delft 4 years ago. TU Delft is such a wonderful place with world-class facilities and nice people. Through the journey, I have grown a lot as a researcher and also as a person. While the above chapters of this thesis are focused on scientific contents, to make the thesis complete, this chapter is vital to tell the stories behind the data and allow me to express my gratitude to my supervisors, colleagues, friends, and families who have supported me all the way through.

First and foremost, I would like to express my deepest gratitude to my two supervisors **Farbod** and **Peter**. I was so lucky to have both of you as my supervisors. I could still remember the excitement when I received the offer from you after 3 interviews. It was you who made all this possible and brought me to a new and interesting field that combines dynamics and physics. I appreciate a lot that you were always there to give me guidance and support whenever I needed it, and at the same time gave me plenty of freedom to explore the topics.

Farbod, as my daily supervisor, thank you for being there with me at every moment of my PhD. I truly learned a lot from you both in science and personal development. I still remember that in our first interview, you asked me if I could say something about what I had learned about vibration and I could not give you a straight answer. But now, with your help, I accomplished a doctoral thesis about dynamics. You are the one who trained me on how to use LDV and taught me the fundamentals of dynamics in the Engineering Dynamics course. I have to say that the course you taught was so clear and easy to follow, which was the best course I had ever taken. The 'Best Lecturer' you earned also proved that. I can also remember the encouragement you gave me 'be confident, no one knows better than you for your own project' before I gave my first international conference presentation in Rome, which truly gave me much confidence, not just in that conference but at every moment when I needed strength. I am also grateful for all the moments you sat together with me to solve all kinds of difficulties. Your passion and insights into science are influential in making me a good researcher.

Peter, as my promotor, I feel truly promoted by you. Thank you for all your help. The first impression of you was 'nice', which gave me the most direct motivation for going to Delft when I was making the decision. All your help and support after I started my PhD proved that I made the right decision. Thank you for going to the labs and helping me tackle technical problems in person. I could still remember that the first resonance peaks of the levitating plate I observed were under your help. I enjoyed a lot the discussions with you. Your input and insight into physics and diamagnetic levitation were always helpful and inspiring. Whenever asked, you could always give many solutions, not just general ideas, but detailed methods to solve problems step by step. Yes, you were strict on every detail of each step of theoretical derivation and experiment procedures, but I

did learn pretty much by answering your questions and feel 'promoted' after your questions were answered. It was something I learned from you and it will be a fortune of me for the rest of my research career. I am also grateful that you would think in my place and help me with many things.

I sincerely thank both of you for raising me to be a mature researcher by teaching me how to think and conduct research independently, how to tackle problems, how to pursue a higher level of research, and how to be confident and present myself; also for all the help and support you gave me.

Secondly, I would like to thank the committee members in my PhD defense, which are **Prof. Herre van der Zant** from TUD, **Prof. Andrei Metrikine** from TUD, **Prof. Ping Koy Lam** from A*STAR in Singapore, **Prof. Jason Twamley** from OIST in Japan, and **Dr. Selim Hanay** from Bilkent University in Turkey. Thank you all for spending time to read my thesis and give comments. Also thank you all for being present in my defense and I look forward very much to the discussions.

I gratefully acknowledge China Scholarship Council (CSC) without which my PhD research and thesis would not have been possible.

During the 4-year PhD project, I also received lots of help from other professors. The first in line is our collaborator **Kunal** in the Faculty of Aerospace Engineering. Thanks a lot for lending your hands and promising to collaborate when we reached out to you for new material fabrication. Your support and input during the experimental and paper-writing phases helped us a lot. It was a pleasant experience to work with you and get to know the fancy 3D-printing projects going on in your labs.

I also want to express my gratitude to **Murali** for giving me much support in many projects, like the liquid sensing topic. Besides, I appreciate a lot that we had many pleasant talks which I enjoyed pretty much, including the one we had in Rome at my first international conference, as well as many ones we had on Friday afternoon after work. It was relaxing to talk with you and we would cover topics from culture to philosophy. You also inspired me a lot and gave me advice on how to choose after PhD. Thank you and wish you all the best in the research of MEMS.

Next, I would like to thank **Gerard** for your help with choosing the parts of my vacuum system and for many nice inputs in every Tuesday morning meeting. **Richard**, we tried to collaborate on a levitation project. Even though it did not work out, I still like the many novel ideas you had in mind, like the 'critical point drying' method. It was also nice to work with you in the Engineering Dynamics course. I also would like to thank **Sabina** and **Wouter** in the DMN group, who gave me comments in the DMN meetings. In addition, many thanks to **Just, Alejandro, Marcel, Andres, Fred, Hassan, Hans, Ivan, Nandini** for creating such a great environment in PME and for the nice talks we had.

Since a major component of my PhD project was based on experiments, I could not finish my thesis without the support of our kind technicians. Thank **Rob** for all the help in the management and ordering stuff; **Patrick** for helping with the vacuum system and the equipment in the optics lab; **Gedion** for training and helping with the laser cutters and 3D-printing devices; **Spiridon** for responding quickly on part manufacture; **Bradley** for helping with electronic/electrical measurements. Besides, I want to say thank you to all the secretaries in PME, **Marli, Lisette, Marianne, Birgit, Corrine**, who made our life in PME easier.

Moving to the nice postdocs and PhDs in PME, I would say it was all of you that made me have a great time in PME. First, I would like to express my gratitude to my colleagues in the ENIGMA group. **Ata**, thank you for the nice job on your master project, so I could start the levitation project quickly. I also want to thank you for helping me set up the experiments when I just started my PhD and for the help with Comsol and AUTO. It was also great to have you as my friend. I enjoyed the time we had in the Utrecht summer school, and I believe you can always find the right fresh grass you like and have a happy life :). Thank you for being my paranymph. **Irek**, we went to pick up the bacteria from the Apply Science faculty together, and now your bacteria had made you a big success in science and your career. Congrats again! I also want to thank you for proposing me to use the ENIGMA turbopump which led to the success of my later measurements. I enjoyed pretty much the ping pong games we played at the spot near Delft station, as well as the talk we had in Arnhem. By the way, the book I told you about is called 'Dream of the Red Chamber'. Please let me know how you like it if you have the chance to read it. **Abhilash**, thank you a lot for your help when I looked for a job. I learned a lot from you about how to present myself. I also enjoyed the time when we were at the Utrecht summer school. Wish you a bright future in ASML and go further in integrating AI with engineering. **Zichao**, thank you for serving me the Youpo noodle at your house. I tried it myself later many times, but it was never as good as yours. And, I still remember your promise to invite me to your house for other homemade foods when you are skillful in cooking. Also, thank you for helping me in the labs, and helping with me moving house. **Ali**, you always work hard in the office and are passionate about mathematical models. I enjoyed the time we worked together as TAs and the time we were in Ireland.

I also want to extend my gratitude to my office mates in room G130. **Tomas**, you gave me lots of help when I just started my project. Thank you for helping me with the LDV, Zurich lock-in amplifier, vacuum chamber, Allan deviation and many other things. I was grateful that each time I came to you for help, you were always patient to answer my questions. I also enjoyed a lot the lunch and coffee breaks we had together. **Satadal**, another postdoc in our office and a know-everything person in PME. Thank you for your help with the conductivity measurements, and I could always learn something new from you during our lunch and coffee breaks. **Sabiju**, you accompanied me in the office through my whole four years. I enjoyed a lot your company and the talks we had about research, life and many others. Thank you a lot for your help when I searched for a job and also for the dinner in your house before I left Delft. I hope your life will not be 'miserable' anymore and best wishes to your families. **Minxing**, another know-everything person in our office. Thank you for teaching me tennis and I will keep playing it. It was also pleasant to talk with you since you always proposed many novel ideas. I wish you will fulfill your goal in research and business in the end. **Andrea**, we also spent 4 years together in G130. Thank you for your help in the labs, and I enjoyed the time together during the course in Den Haag. I also want to thank **Gurhan** for being a nice desk mate and for sharing with me all kinds of information; **Jian** for the nice suggestions when I just came to Delft; **Saleh** for training me with the SEM and I enjoyed a lot the lunches together before Covid; **Kai Wu** for taking me to all kinds of nice restaurants; **Yuheng** for the nice talks we had; and also thank **Pieter, Simona, Nils, Qais** for being nice office mates.

I also have a nice memory in PEM due to many nice colleagues. **Yong**, the most hard-working PhD in PME. No matter when I went to office, you were always there. It was reassuring to have somebody like you around. I enjoyed a lot the conversations we had and the foods you prepared for me. Of course, thank you a lot for all the help with my research and life. **Hanqing**, a reliable man and another hard-working PhD in PME. I still remember the bicycle trip we had toward Zoetermeer. Thank you for your help in the lab and life, and for being my paranymph. I also want to thank **Lidan** for your help when I just went to Delft; **Qi Wang** for helping me with finding a job; **Long Wu** for helping me get started in PME; **Martin Lee** for your help with the graphene and vacuum parts; **Alkisti, Cristina, Guishan** and **Andre** for your company in the lunches and coffee breaks we had at the beginning of my PhD; **Daniel** for inviting me to your boat; **Niranjan** for your help with finding a job; **Zhichao** for your humours and all kinds of information and suggestions; **Xinxin** for playing tennis with me on weekends; **Matthijs** for your help with the vacuum chamber and the nice talks with had during lunches; **Vincent** for helping me with the STEP method; **Rajit, Vibhas, Arnoud, Stijn** for the footballs we did; **Yujiang, Sifeng, Xiliang, Chao, Kai, Yang, Binbin, Mingkai, Ze Yu** for the fun things we did together; **Gabriele, Roberto** for the ping pong games we played. I also would like to thank other fellows from our department: **Pierpaolo, Sandre, Hadi, Martin, Makars, Dongil, Maurits, Dong Hoon, Masoud, Ruben, Ahmed, Lucas** and many others.

I want to thank **Nimit, Tjebbe** and **Eli** for working with me on the diamagnetic levitation as your master projects; and also **Chris** and other students for working with me on your bachelor projects. I am grateful that you all contributed to this thesis.

Outside PME, there are also many people who have given me help. First, I want to thank our collaborator **Satya** from the Faculty of Aerospace Engineering, who helped me a lot in the high Q topic for the composite fabrication and material characterization. It was my pleasure to work with you. I do remember all the coffee talks before we did experiments. It was so nice to work together and I learned a lot from you about composite fabrication, 3D printing and piezo transducers. Wish everything goes well with your PhD project. Secondly, I want to express my gratitude to **Jiahui** from the Department of Biomechanical Engineering for helping me fabricate the first diamagnetic composite, which gave me faith in pursuing the high Q project.

Apart from the above-mentioned colleagues, there are also many friends in the Netherlands who accompanied me all the way through my PhD. It was you who share my happiness and bitterness, and make my life more colorful. First and foremost, I would like to thank **Shuo** and **Lubin** for being with me through the four years. **Shuo**, we have known each other from the day we departed for Netherlands in Guangzhou. I was grateful that our friendships became firmer with time going on. I was touched and grateful that you always took my business as yours and helped me without reservation. We have been through lots of things together and I believe I would always remember them in my heart. I wish everything goes well with your research and I believe a brighter future is waiting for you. **Lubin**, I am grateful that I have a friend like you whom I could come for any help without a second thought. It was you who came to help me when I was locked out of the door, who took me when I needed a place to live and who beared the heaviest luggage when we had the bicycle trip around Netherlands. All these could not be simply appreciated by words. I do and will continue to remember all the roads we

had cycled together and the rains we had been caught in. I also want to thank **Wenxuan** for all kinds of help and the company you gave me. You are such a distinctive friend in my life and taught me many things. I have learned how to be more confident and brave from you. Talking with you I would see different aspects of things. Surely, special thanks to **Dengxiao** for all the delicious foods and for taking care of us each time when we were on a trip together. It was pleasant to travel with you, since you could always cheer up the whole team. I will also miss the time we played Majiang.

In addition, I would like to thank **Guoshuai** for making us laugh; **Tian Tao** and **Xiang Wang** for the great time we had in Belgium and many gatherings; **Yang Hu** and **Shanshan** for the crazy bicycle trip we had; **Fengqi** for your help when I just arrived in Delft; **Chao Ma, Yunpeng** for the card-playing time; **Chunyan** for helping me find a house; **Xiuli, Min Zhang, Nan Tao** for the company when we just started our life in Delft; **Yan Yuan** for giving me pain killers for my teeth; **Xuetong** for the useful information you shared with me. I also want to thank **Coco, Tianlong, Mingliang, Max, Yi Luo, Guoding, Yuqian, Yueting, Yageng, Bowen, Ziying** for the great time we had. I am also grateful that I have some nice friends from Waganigen, and thank **Ke Peng, Maomao, Jingwei** for going to Delft to celebrate my birthday with me; **Yuxin, Kaisheng, Markus** for the nice trips we had. Besides, I was lucky to have some great friends from Rotterdam and Leiden. Thank **Yueyang, Yu An, Huimin, Xiaowei, Patrick, Ziru, Xiaozhou, Hongyu** who gave me a memorable time.

Next, I would like to express my deep gratitude to **Dailing**. Thank you for being by my side to share my happiness, listen to me talking about levitation and give me suggestions on how to make a figure better. You made my last two year PhD life more fulfilling and complete. We always had many common topics to talk about and I was happy that we could understand each other most of the time. I also enjoyed all the weekends we were together and the trips we went on. I am sorry that I can not accompany you by your side in the near future, but as we agree we will end up in the same city one day.

Last but not least, I want to thank my family for all the support. 父母在，不远游。然而而立之年，还离家越来越远。感谢妈妈、姐姐和哥哥一直坚守着这个家，让我无论在哪里都有一个可以寄托的港湾。感谢妈妈对这个家的无私付出！感谢姐姐和哥哥对妈妈无微的照顾！感谢家人对我漫漫求学路的一直支持。大爱无言，你们的爱是我一直往前走的动力。

Xianfeng Chen
in Guigang
January 2023

CURRICULUM VITÆ

Xianfeng CHEN

25-08-1992 Born in Guigang, China.

EDUCATION

2008–2011 High School
Guigang Senior High School
Guigang, China

2011–2015 Undergraduate in Mechanical Engineering
China University of Petroleum, Qingdao, China (Sep,2011–Jun,2015)
University of Wollongong, Wollongong, Australia (Jan,2015–Jun,2015)

2015–2018 Master in Mechanical Engineering (Honours)
China University of Petroleum, Qingdao, China

2018–2022 Ph.D. in Precision and Microsystems Engineering
Delft University of Technology, Delft, The Netherlands
Thesis: Dynamics of diamagnetically levitating resonators
Promotors: dr. Farbod Alijani
Prof. dr. Peter G. Steeneken

LIST OF PUBLICATIONS

8. **X. Chen**, Tjebbe de Lint, F. Alijani, P. G. Steeneken. *Nonlinear dynamics of diamagnetically levitating resonators.* 2022. To be submitted.

7. S. K. Ammu, **X. Chen**, F. Alijani, P. G. Steeneken, K. Masania. Direct ink writing piezoelectric composites for application as ultrasound transducers. 2022. In preparation.

6. **X. Chen**, S. K. Ammu, K. Masania, P. G. Steeneken, F. Alijani. *Diamagnetic composites for high-Q resonators.* Advanced Science, 2203619 (2022).

5. **X. Chen**, N. Kothari, A. Keşkeklerr, P. G. Steeneken, and F. Alijani. *Diamagnetically levitating resonant weighing scale.* Sensors and Actuators A: Physical **330**, 112842 (2021).

4. N. M. Zadeh, F. Alijani, **X. Chen**, I. Dayyani, M. Yasaee, M. J. Mirzaali, A. A. Zadpoor. *Dynamic characterization of 3D printed mechanical metamaterials with tunable elastic properties.* Applied Physics Letters **118**,211901 (2021).

3. **X. Chen**, A. Keşkeklerr, F. Alijani, and P. G. Steeneken. *Rigid body dynamics of diamagnetically levitating graphite resonators.* Applied Physics Letters **116** (24), 243505 (2020).

2. L. Zhang, **X. Chen**, H. Wang, S. Zhao, N. Li, D. Zhang. *Research on critical loading force in precision cropping system based on hydraulic compensation.* International Journal of Mechanical Sciences **142**, 44-50 (2018).

1. **X. Chen**, L. Zhang, D. Zhang, X. Wang, H. Wang, Y. X. Liu, Y. H. Liu. *Influence rule of loading parameters on crack initiation at the tip of V-shaped notch of bars based on XFEM.* Journal of Plasticity Engineering **25**(4), 254-261 (2018).